Muons in early ATLAS Data

from first collisions to W^+W^- production

John Philip Ottersbach

Dutch title: *Muonen in eerste ATLAS data*
- van de eerste botsingen tot W^+W^- productie

Cover: Designed by Johannes Heckl and John Philip Ottersbach
Publisher: John Philip Ottersbach
Copies: 250 (August 2012)
ISBN: 978-94-6191-390-6

Netherlands Organisation for Scientific Research

This work is part of the research program of the Foundation for Fundamental Research on Matter (FOM), which is part of the Netherlands Organisation for Scientific Research (NWO). It was carried out at the National Institute for Subatomic Physics (Nikhef) in Amsterdam, the Netherlands, as well as at the European Organization for Nuclear Research (CERN), Geneva, Switzerland.

Muons in early ATLAS Data

from first collisions to W^+W^- production

ACADEMISCH PROEFSCHRIFT

ter verkrijging van de graad van doctor
aan de Universiteit van Amsterdam
op gezag van de Rector Magnificus
prof. dr. D.C. van den Boom
ten overstaan van een door het college van promoties
ingestelde commissie,
in het openbaar te verdedigen in de Agnietenkapel
op dinsdag 25 september 2012, te 12:00 uur

door

John Philip Ottersbach

geboren te Wuppertal, Duitsland.

Promotor:	Prof. dr. S.C.M. Bentvelsen
Copromotor:	Dr. P.M. Kluit
Overige Leden:	Prof. dr. S.J. de Jong
	Prof. dr. ir. E. Koffeman
	Prof. dr. P.M. Kooijman
	Prof. dr. M.H.M. Merk
	Dr. E.J.W. Moyse
	Dr. I. van Vulpen
	Dr. E. de Wolf

Faculteit der Natuurwetenschappen, Wiskunde en Informatica

"But it ain't about how hard you hit. It's about how hard you can get hit and keep movin' forward."

Rocky Balboa [1]

[1] as Sylvester Stallone in [53].

Contents

Preface

Bern, 1905. The new century starts with a revolution. A young examiner in the local patent office and freshly graduated doctor in experimental physics structures, summarizes and interprets the thoughts and findings of some of the leading physicists at the time: Ernst Mach, James Maxwell, Henri Poincaré and Hendrik Antoon Lorentz. The result shall not be less than a revolution in the understanding of our world and one of the biggest successes of science.

Albert Einsteins theory on special relativity was published in the german physics journal *Annalen der Physik* in September 1905. His thoughts about space and time led him to another striking publication just two month later. It deals with the equivalence of matter and energy. The resulting formula became the most known formula of physics

$$E = \gamma mc^2 \ .$$

Its simplistic beauty and momentous consequences inspired and enchanted not only scientists but also the broad public down to the present day.

It is this equivalence of energy and matter that makes the foundation on which modern particle physics is based. It allows particle physicists to study the elementary substructures of our world by colliding highly accelerated subatomic particles. The energy released in these collisions can transform into matter creating different, exotic particles, unveiling the fundamental building blocks of our universe. The energy densities that are reached in modern particle accelerators mirror the ones of the universe at its very early stage, less than trillionths of a trillionths of a trillionths of a second after the Big Bang. Supported by ample detailed studies of particle collisions with increasing energies, physicist were able to develop a comprehensive model of our world throughout the last decades. However, major questions still remain to be answered. For example: *What is the origin of dark matter and dark energy? Why did matter dominate over antimatter? Where do the particle masses come from?*

2011, Geneva. Only 130 km south-west of Einsteins small apartment in Bern, the birthplace of the mentioned revolution, a global collaboration of particle physicists is preparing to pave the way for new discoveries, deeper insights in the nature of our universe and maybe, another revolution.

CHAPTER 1

Introduction to W-Pair Production at the LHC

1.1 Overview

In this thesis, we are going to explore the first data recorded by the ATLAS experiment at the LHC, CERN. We will thereby focus on the reconstruction and identification of muons. Particularly di-muon final states play an important role, both for the performance studies as well as for the physics analysis detailed in this thesis. This chapter discusses the underlying theory to the studies carried out in the subsequent chapters. After a brief introduction to the Standard Model we focus on the relevant physics processes for this thesis. Section 1.3 discusses the J/ψ particle which plays a prominent role in the performance studies throughout chapters 4 and 5, while Section 1.4 details the underlying theory to the measurement of the W^+W^- production cross section discussed in Chapter 6.

1.2 The Standard Model of Particle Physics

It is in the 70's of the past century when numerous contributions of the leading physicists finally form a consistent theory which describes the elementary particles and their interactions, incorporating three of the four forces of nature. For the first time, the observed physics at the smallest distances was comprehensively described by a theoretical model. It structured and explained the zoo of *elementary* particles that had been discovered since J.J. Thomson's discovery of the electron in 1897 and whose growth was dramatically boosted by the exploitation of the first particle collider experiments in the 50's and 60's of the twentieth century [2]. However, to fully size this breakthrough one needs to confront the numerous precise predictions of the model with the corresponding experimental findings. A phenomenal agreement between the measurements and the theoretical predictions verified the theory. It is for these reasons that it was given the name:

The Standard Model of Particle Physics (SM) [4, 6].

1.2.1 The Elementary Particles and Their Interactions

The Standard Model utilizes group theory to describe electromagnetism, as well as the two short-range nuclear forces, the weak and the strong force with the symmetry group $SU(3) \times SU(2) \times U(1)$. Gravity is not incorporated in this model. However, at the energy scales of interest, gravity is $O(10^{25})$ weaker than the weakest of the three incorporated forces, the weak force. Thus, gravitational effects can be neglected.
According to Noether's theorem, a differentiable global symmetry has a corresponding conservation law [3]. The conserved quantities for the three forces are the electric charge e in case of electromagnetism, the third component of the weak isopsin I_3 for the weak force and *color* for the strong force.

Gauge Bosons

The generators of the three local symmetry groups are associated to gauge bosons that mediate the to each symmetry corresponding force. The photon (γ) mediates electromagnetism, the three gauge bosons W^+, W^- and Z are the carriers of the weak force while eight gluons mediate the strong force. The experimentally determined masses and electric charges of the gauge bosons are listed in Table 1.1. They follow the Bose-Einstein statistic and have an integer spin. A second category of particles in the Standard Model has half-integer spin, follows the Fermi-Dirac statistics and is consequently referred to as *fermion*.

	gauge bosons			
	γ	$W^{\pm}$	Z	g
mass [GeV]	0	80.399 ± 0.023	91.188 ± 0.002	0
electric charge	0	± 1	0	0

Table 1.1: The gauge bosons of the Standard Model are shown with their masses and electric charge. All values are taken from [1].

Quarks and Leptons

All matter in our universe is made of fermions. The elementary fermions are grouped into quarks and leptons. One distinguishes leptons that only interact weakly, the neutrinos (ν), from charged leptons which can also interact electromagnetically. The color carrying quarks can interact via all three forces incorporated in the SM, allowing the formation of atoms. All atoms in the universe are composed of electrons (e^-) as well as up- and down-quarks (u, d). However, particle collider experiments revealed the existence of 2 copies with increasing particle masses of these so called *first generation* fermions. The charged lepton of the second generation, the muon, commonly denoted as μ plays an important

role in this thesis. It is the heavier brother of the electron, carrying about 200 times its mass. However, it is yet too light to decay hadronically. It decays weakly into an electron and the corresponding neutrinos, after a long lifetime of $\tau_\mu \approx 2.2\,\mu$s. The long lifetime and the comparatively low energy loss via Bremsstrahlung due to its high mass, allow the muon of a given energy to penetrate matter far more deeply than electrons.
Particles carrying color charge can only be observed in bound-states, due to the color confinement. These bound-states are color neutral and called hadrons. The existing three colors and anticolors leave room for two different types of bound-states. Bound-states of three quarks, such as the proton (uud) or the neutron (udd) are referred to as baryons, while the bound-states of a quark-antiquark are named mesons. An example of the latter is the $c\bar{c}$ bound-state, named J/ψ, which is discussed in Section 1.3. The quarks and leptons of all three generations are listed in Table 1.2 together with their masses and electric charge. All particles have their corresponding antiparticles with the same quantum numbers and mass but opposite charge. They are commonly denoted with a bar.

	generation						
	I		II		III		
		mass [MeV]		mass [GeV]		mass [GeV]	electric charge
quarks	$\boldsymbol{u}$	$[1.7; 3.1]$	$\boldsymbol{c}$	$1.29^{+0.05}_{-0.11}$	$\boldsymbol{t}$	$172.9 \pm 0.6 \pm 0.9$	2/3
	$\boldsymbol{d}$	$[4.1; 5.7]$	$\boldsymbol{s}$	$[0.08; 0.13]$	$\boldsymbol{b}$	$4.19^{+0.18}_{-0.06}$	−1/3
leptons	$\boldsymbol{e}$	0.5110 ± 0.0000	$\boldsymbol{\mu}$	0.1057 ± 0.0000	$\boldsymbol{\tau}$	1.7768 ± 0.0002	−1
	$\boldsymbol{\nu_e}$	$]0; 2\times10^{-6}]$	$\boldsymbol{\nu_\mu}$	$]0; 2\times10^{-9}]$	$\boldsymbol{\nu_\tau}$	$]0; 2\times10^{-9}]$	0

Table 1.2: The fundamental fermions of the Standard Model are shown grouped into the three generations. The masses of the particles, or the corresponding mass ranges are given together with the electric charge. All values are taken from [1]. Some of the given values are rounded.

1.2.2 The Standard Model Higgs

Despite its predictive power, the Standard Model also shows various weaknesses like the introduction of 21 independent parameters, whose values are not predicted in the theory and have to be determined experimentally [5]. It also offers no explanation to why there are three generations of fermions, or how gravity fits in the picture. But the probably most striking incongruity lies in the origin of the elementary particle masses. The Standard Model allowed originally only for massless particles. Divergencies in the loop diagrams of massive particles break the essential renormalizability of the theory. It was extended by Peter Higgs and others to incorporate a mechanism that would give rise to the mass of the massive Standard Model particles, such as the heavy weak gauge bosons [9]. However,

this extension of the theory introduces an additional particle, the Higgs boson. Despite the large efforts of the particle physics community in the last decades no experiment has discovered the Higgs boson, to date. The latest efforts however, will bring an end to the search of the Higgs boson in the near future, with the LHC experiments being designed to either discover or rule out the Standard Model Higgs boson, see Section 2.3. Combining the results of previous experiments and the latest findings sets limits on the SM Higgs boson mass: 114.4 GeV $< m_H <$ 146 GeV or $m_H >$ 476 GeV [10, 11].
The production cross section at the LHC [1] as a function of the SM Higgs boson mass is given in Figure 1.1(a). The four leading production processes are the gluon fusion (pp→H), the vector boson fusion (VBF, pp→qqH) and the two Higgs boson radiation processes (pp→WH, pp→ZH) that are depicted in Figure 1.2. Figure 1.1(b) displays the possible decay channels of the SM Higgs boson with their predicted branching ratios. One important decay channel to look for the Higgs boson is its decay into a pair of W-bosons, i.e. $H \rightarrow W^+W^-$. In the leading production channel, where two gluons fuse to create a Higgs boson, the cross section times the branching ratio for the process $pp \rightarrow H \rightarrow W^+W^-$ has been calculated to $\sigma \times \mathrm{BR}(H \rightarrow W^+W^-) = (14.12^{+19.2\%}_{-15.1\%} \times 0.305)\ \mathrm{pb}^{-1}$ for a Higgs boson with mass $m_H = 130$ GeV [66] [2].

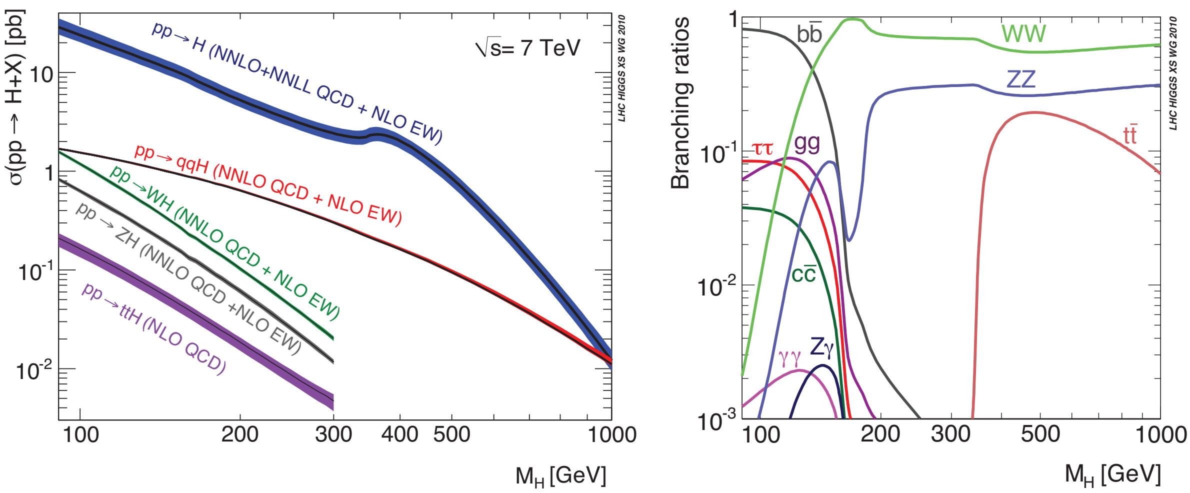

(a) SM Higgs boson production cross section

(b) SM Higgs boson branching ratios

Figure 1.1: The expected SM Higgs boson production cross section as a function of the corresponding Higgs boson mass is shown in (a) for a center of mass energy of 7 TeV. (b) shows the branching ratios of the SM Higgs boson, again as a function of its mass. The layout of the two plots taken from [66] was modified for this thesis.

[1] The Large Hadron Collider is detailed in Section 2.2.

[2] The errors on the cross section are given as the linear combination of the QCD scale, PDF and strong coupling uncertainties.

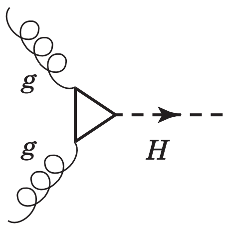

(a) gluon fusion

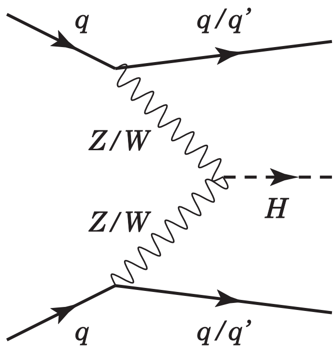

(b) vector boson fusion

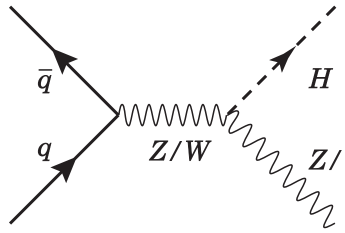

(c) Higgs boson radiation

Figure 1.2: The Standard Model tree-level Feynman diagrams for the leading SM Higgs boson production processes at hadron colliders are shown.

1.3 The J/ψ Meson

The J/ψ was independently discovered in 1974 by the group of Burton Richter at the Stanford Linear Accelerator Center (SLAC) and the group of Samual Ting from MIT at the Brookhaven National Laboratory (BNL) [7]. The discovery confirmed the existence of a predicted fourth quark, the charm quark (c) and was awarded with a Nobel Prize two years later.
The J/ψ is the first excited charmonium state, i.e. it has the second-smallest rest mass of all $c\bar{c}$ bound-states. However, since it is the lowest rest mass charmonium state with the same quantum numbers as the photon, its production rate is much higher than any other $c\bar{c}$ meson. Its rest mass has been measured to be $m_{J/\psi} = 3096.92 \pm 0.01$ MeV [1]. The comparatively long mean lifetime of the J/ψ leads to a narrow average width of its mass distribution of $\Gamma = 92.9 \pm 2.8$ keV. One can distinguish three different J/ψ production mechanisms at hadron colliders:

- the *direct* production: The J/ψ is directly produced in the central collision, e.g. $pp \to J/\psi$ in case of a proton-proton collider such as the LHC discussed in the subsequent chapter.
- the *prompt* production: The J/ψ is produced via a decaying excited charmonium state, i.e. for example $pp \to \chi_c \to J/\psi + \gamma$, or $pp \to \psi'_c + X \to J/\psi + X$, where X denotes any particle(s) created in the associated process. χ_c and ψ'_c stand substitutional for the various $c\bar{c}$ bound-states of the corresponding type, i.e. χ_{c0}, χ_{c1}, …, $\psi(2S)$, $\psi(3770)$, etc..
- the *non-prompt* production: Here, the J/ψ is produced in a weak decay of a B meson.

It is very difficult to distinguish the direct and prompt produced J/ψ's experimentally in existing collider experiments. Figure 1.3(a) shows the inclusive J/ψ production cross

section in the two muon final state measured by the ATLAS collaboration in the central detector [8]. The results are compared to the findings of the CMS collaboration. The theoretical uncertainties from the unknown spin alignment of the J/ψ are represented by the yellow band.
Only 70% of the J/ψ's decay via the strong force leaving a share of 30% for the electromagnetic decay of the J/ψ's [58]. The corresponding Feynman diagrams show the two possible decay processes in Figure 1.4. Naively, one would expect the strong force to dominate more clearly over the electromagnetic force in the decay. The strong decay of the J/ψ is suppressed because of two reasons. D-mesons carry a single charm quark and would be hence a preferred decay product. However, their masses are larger than the J/ψ mass and hence, this strong decay is not possible. The other reasons for a suppressed strong J/ψ decay is the conservation of spin and color, requiring a decay into at least three gluons.
The majority of J/ψ's still decay hadronically ($(87.7 \pm 0.5)\%$). However, a comparatively large fraction decays leptonically into a electron-positron or muon pair. The latter decay mode plays an important role in this thesis. The branching ratio $\mathrm{BR}(J/\psi \to \mu^+\mu^-)$, i.e. the fraction of J/ψ's that decay into a pair of muons is $(5.93 \pm 0.06)\%$. The invariant mass plot of two muons reconstructed in the ATLAS experiment, described in Section 2.3, is shown in Figure 1.3(b). Note that the width of the J/ψ resonance is about 100 MeV and hence clearly dominated by the detector resolution.

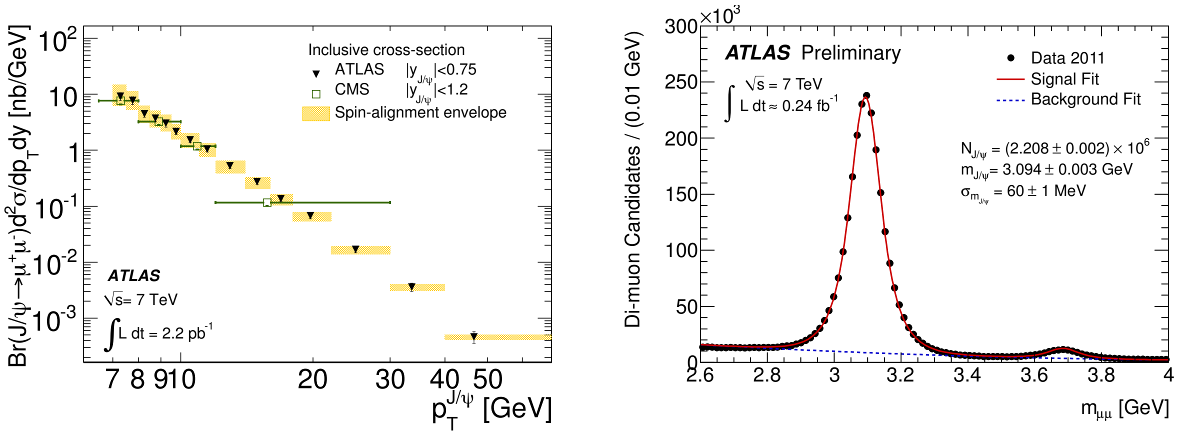

(a) production cross section (b) di-muon invariant mass

Figure 1.3: The inclusive production cross section of $J/\psi \to \mu^+\mu^-$ measured by the ATLAS collaboration is shown in (a), while the J/ψ resonance in the two muon invariant mass spectrum is shown in (b). In addition to the J/ψ, the next excited $c\bar{c}$ state called $\psi(2S)$ is visible around $m_{\mu\mu} = 3.69$ GeV. The plots are taken from [8, 68].

Figure 1.5 shows the kinematic distributions of muons from J/ψ decays [3]. As shown in (a) and (b), the decay products of the J/ψ cover all space up to very large values

[3]The distributions are based on Monte Carlo generated $J/\psi \to \mu^+\mu^-$ events as used in Chapter 5.

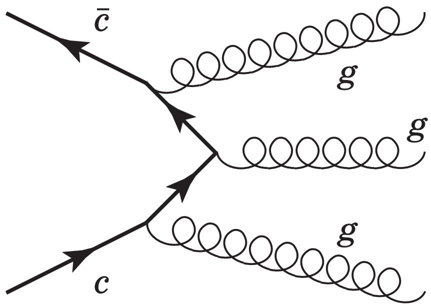

(a) strong decay

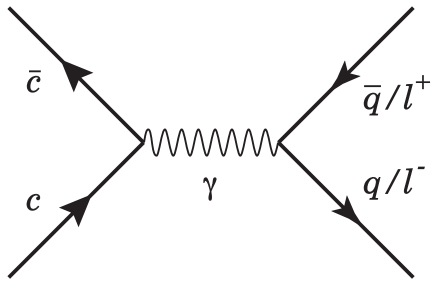

(b) electromagnetic decay

Figure 1.4: The Standard Model tree-level Feynman diagrams for the decay of a J/ψ are shown. (a) shows the strong decay while (b) depicts the decay via the electromagnetic force. l^- indicates either an electron or muon, l^+ the corresponding anti-particle.

in pseudorapidity [4]. Most of the muons have comparatively low transverse momenta. However, the spectrum reaches up to about 20 GeV as shown in (c). The corresponding distribution of the opening angle between the two muons is depicted in (d) and shows that the vast majority of the muon pairs have a sufficiently large opening angle which will be important to separately identified the two muons in the experiment. These features together with the clean, narrow resonance and the overall large production cross section makes the J/ψ a very attractive tool for various physics and performance studies. Chapter 5 will exploit these features of the J/ψ.

1.4 W^+W^- Production and Decay

Measuring the production of W-pairs, i.e. W^+W^- is an important test of the Standard Model. Moving from an originally only global symmetry to a local and hence gauge invariant symmetry requires the introduction of gauge fields. The gauge invariance is of outstanding importance since it makes the theory renormalizable. Renormalization assures that no divergencies occur in the theory.
The weak force is described in the Standard Model by the non-abelian gauge group $SU(2)$ in which the gauge fields quantize and the gauge bosons W^+, W^- and Z emerge. The most important consequence that arises from the non-abelian structure of the local $SU(2)$ symmetry are gauge boson self couplings, i.e. a Z-boson can couple to a pair of W-bosons (triple gauge boson coupling) and four W-bosons can connect in one vertex (quartic gauge boson coupling). The triple gauge boson coupling appears in a process, shown in Figure 1.6(c) for hadron colliders, that contributes to the overall production rate of W-pairs with approximately 10 % at the LHC. This significant contribution from the triple gauge boson coupling allows one to probe the non-abelian structure of the weak force in the SM and hence also provides the sensitivity to possible deviations from the SM. These deviations could either be observed in the measured production cross section or kinematic

[4]Details on the coordinates are given in Section 2.3.1.

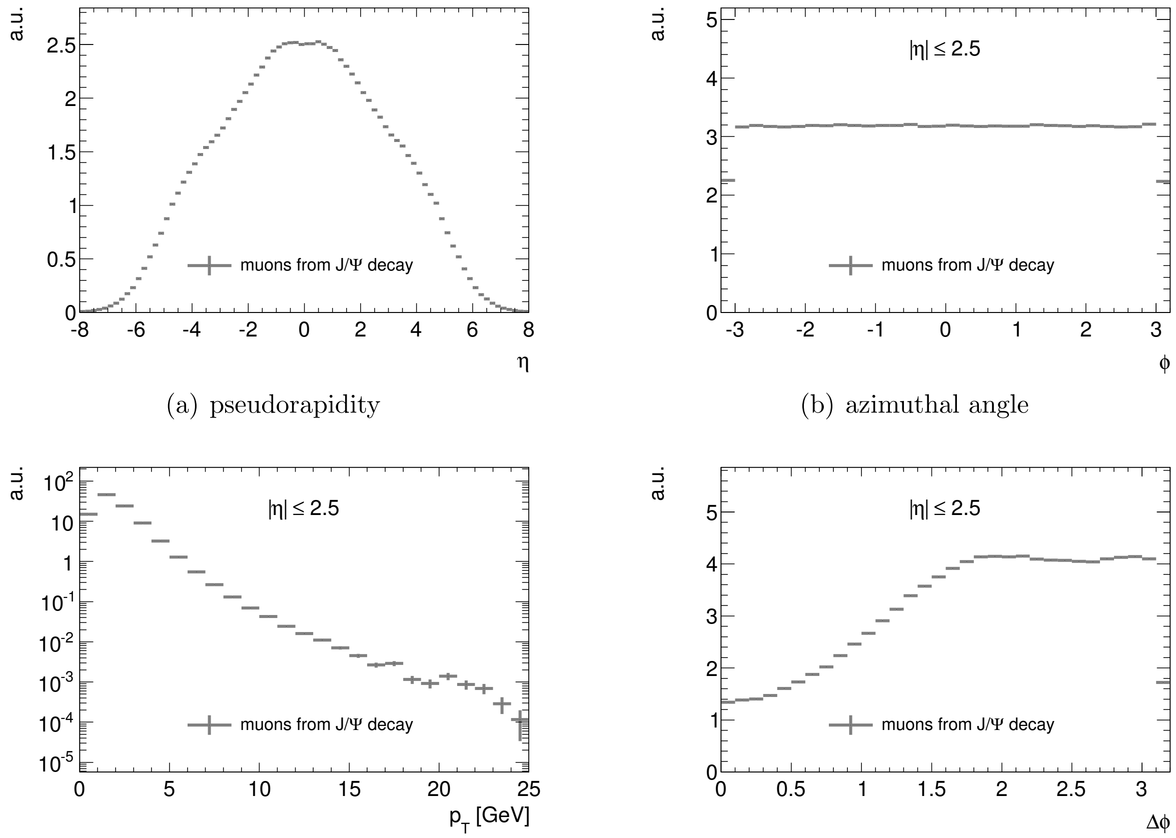

(a) pseudorapidity (b) azimuthal angle

(c) transverse momentum (d) opening angle

Figure 1.5: The kinematic distributions for muons from J/ψ decays are shown.

distributions of the selected events and be possibly caused by yet unobserved particles in loop diagrams. Various measurements of these so called anomalous triple gauge boson couplings (aTGC) have been performed, e.g. [12,14,47]. However, no measurement showed evidence for the existence of anomalous couplings.
A profound knowledge of the W-pair production is however also essential for Higgs boson searches in the W^+W^- channel as it will be an irreducible and non resonant background that needs to be controlled. It is for this reason that we focus on a W^+W^- production cross section measurement in Chapter 6 of this thesis. Taking advantage of our work and findings in Chapters 4 and 5, we analyze the muon decay channel of both W-bosons. The branching fraction for a W-boson to decay into a muon is $(10.57 \pm 0.15)\%$ [1], thus about 1% of all produced W-pairs will decay into a $\mu^+\mu^-$ final state.

We give in the following a summarizing overview over the existing cross section calculations as well as the present experimental determinations of the W^+W^- production cross section.

1.4.1 Cross Section Calculations

A first calculation of the $q + \bar{q} \rightarrow W^+ + W^-$ cross section in the Born approximation was published as early as 1979, four years before the discovery of the W-boson [15]. Real, virtual and radiative corrections were added with the first next-to-leading order (NLO) calculation published in 1993 [16]. Since then, QCD corrections and the gluon-fusion process $g + g \rightarrow W^+ + W^-$ have been calculated in addition [17, 18]. The tree-level Feynman diagrams for W^+W^- production at hadron colliders are shown in Figure 1.6. The t-channel production in (a) is the leading production process with about 87 % of the W-pairs being produced in this channel, while the gluon fusion contribution in (b) amounts to only 2.9 %. The Z-exchange diagrams including a trilinear gauge boson coupling in Figure 1.6(d) cancel when summed over up- and down-type quark contributions in the triangular loop. The only contributing process to the W^+W^- production including a vertex with the gauge boson self couplings is shown in Figure 1.6(c).
The latest NLO calculations give a total W^+W^- production cross section of $\sigma_{W^+W^-} = (47.0 \pm 2.0)$ pb^{-1} at the LHC at a center of mass energy of $\sqrt{s} = 7$ TeV [18]. This is about a factor ten larger than the cross section of a SM Higgs boson with $m_H = 130$ GeV in the corresponding channel. The predicted leading order and next-to-leading order W-pair production cross sections as a function of the center of mass energy is listed in Table 1.3. The NLO corrections are significant.

$\sqrt{s}$ [TeV]	$\sigma^{\mathrm{LO}}(W^+W^-)$ [pb]	$\sigma^{\mathrm{NLO}}(W^+W^-)$ [pb]
7	29.51	$47.04^{+4.3\%}_{-3.2\%}$
8	35.56	$57.25^{+4.1\%}_{-2.8\%}$
14	74.48	$124.31^{+2.8\%}_{-2.0\%}$

Table 1.3: The total W-pair production cross section is given for three center of mass energies relevant for LHC physics. The leading order calculation is compared to the next-to-leading order calculation. Renormalisation and factorization scales are set to the W-boson mass. Upper and lower limits are obtained by varying the scales by a factor of two in each direction. The numbers are taken from [18].

1.4.2 Experimental Results

Since the center of mass energy of the electron positron accelerator LEP was increased to $\sqrt{s} > 160$ GeV in the late 90's to allow for the production of W-boson pairs, the theoretically calculated cross section for a W^+W^- production could first be experimentally verified and marked the first observation of trilinear gauge couplings. A good agreement with the SM predictions was found for various center of mass energies, as shown in Figure 1.7.
The first W-pair production cross section measurements on hadron colliders were performed at the Tevatron collider. At a center of mass energy of $\sqrt{s} = 1.96$ TeV the measured cross section $\sigma(W^+W^-) = 13.6 \pm 2.3(\text{stat.}) \pm 1.6(\text{sys.}) \pm 1.2(\text{lumi.})$ pb (CDF collabo-

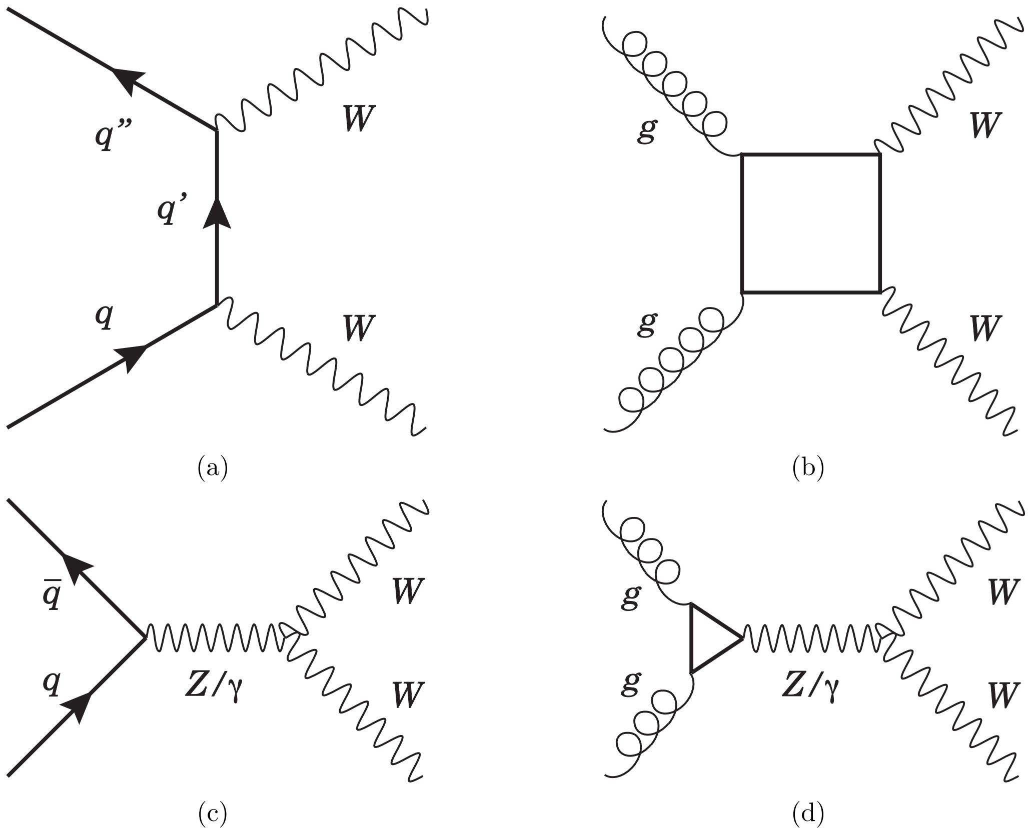

Figure 1.6: The Standard Model tree-level Feynman diagrams for W^+W^- production at hadron colliders are shown. Diagrams (c) and (d) contain trilinear gauge boson coupling vertices.

ration) and $\sigma(W^+W^-) = 13.8^{+4.3}_{-3.8}(\text{stat.})^{+1.2}_{-0.9}(\text{sys.}) \pm 0.9(\text{lumi.})$ pb (DØ collaboration) were found to be in agreement with the NLO predictions $\sigma^{\text{NLO}}(W^+W^-) = 12.4 \pm 0.8$ pb [14]. The most recent measurements are performed at the LHC running at a center of mass energy of $\sqrt{s} = 7$ TeV. The results will be discussed in Chapter 6.

1.4.3 Relevant Background Processes

As already mentioned, the W-pair production cross section will be measured in the di-muon, i.e. $\mu^+\mu^-$ final state with the corresponding neutrinos in Chapter 6. There are various physics processes with the same, or similar final states as well as processes that are a background to this final state, i.e. due to limited detector acceptance or miss reconstruction appear to have a di-muon final state. In the following, we list the relevant processes that contribute to the $W^+W^- \to \mu^+\nu_\mu\mu^-\bar{\nu}_\mu$ background in the order of their production rates.

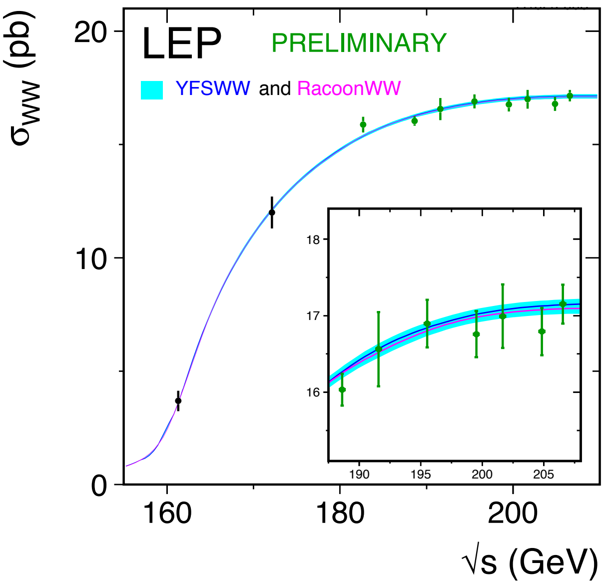

Figure 1.7: The total W^+W^- production cross section in e^+e^- collisions at LEP at center of mass energies of $\sqrt{s}$ = 161 GeV to 207 GeV is shown. The band indicates the SM predictions. The figure is taken from [13].

Drell-Yan and Z-Boson Production

Drell-Yan processes are the largest source of di-muon events at the LHC. The ATLAS collaboration measured the production cross section times the branching fraction for the di-muon final state to be ≈ 1 nb [19]. In the physics process, a quark and an anti-quark annihilate in the central collision. Via the exchange of a virtual photon or Z-boson, a lepton pair is created, such as $\mu^+\mu^-$. The corresponding Feynman diagram is depicted in Figure 1.8(a). The quark and anti-quark pair can also annihilate to create a Z-boson. The final state remains the same, but the invariant mass distribution of the lepton pairs from a Z-boson decay peaks at the Z-boson mass and is hence easily identified. The invariant mass spectrum of Drell-Yan processes in the two muon final state has been measured by the ATLAS collaboration and is shown in Figure 1.8(b) [76]. The J/ψ and Z-boson resonance are the two most prominent peaks in the distribution originating from the comparatively large production cross sections.

Single W Boson Production

The production of a single W-boson can also contribute to the W^+W^- backgrounds, though only a single muon is created in the process, i.e. $W \to \mu\, \nu_\mu$. However, the large production rate of $W + X \to \mu\, \nu_\mu + X$, where X indicates additional physics processes in the event that might also produce a muon, can still create a seizable background

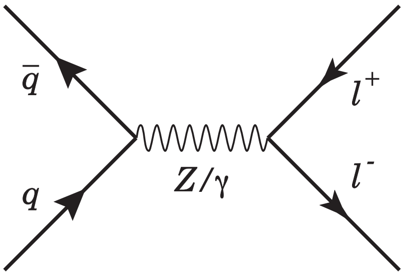

(a) Drell-Yan process

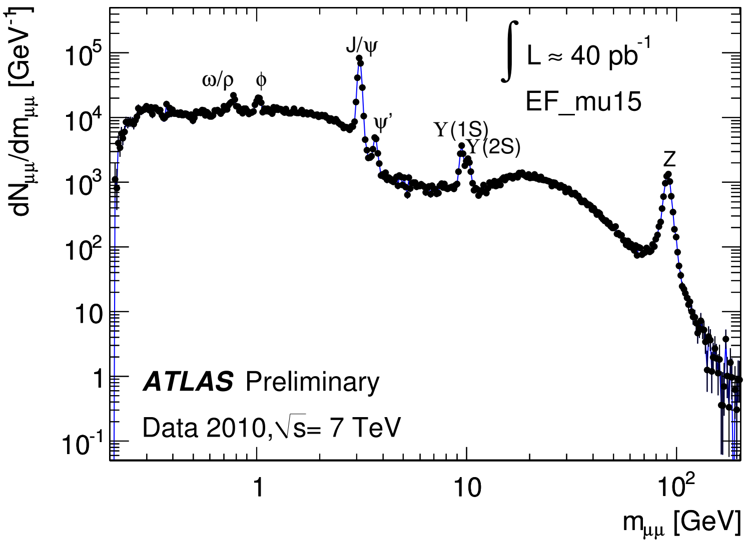

(b) two muon invariant mass

Figure 1.8: The Feynman diagram of the Drell-Yan process is shown in (a). The invariant mass spectrum of two muons in ATLAS is shown in (b). The plot is taken from [76].

contribution. The inclusive W + jets cross section [5] with a muon final state has been measured by the ATLAS collaboration to be approximately 10 nb and is hence almost 5 orders of magnitude larger than the W^+W^- production with the di-muon final state [19].

Top Quark

Top quarks are produced individually and in pairs at the LHC. Both physics processes have to be accounted for in a W^+W^- background estimation. The single top production feynman diagrams are given in Figure 1.9. The s-channel diagram marks the leading contribution in the single top production with $\sigma^{\mathrm{NNLO}}(\mathrm{s-channel}) \approx 65$ pb [67]. Top quarks decay into a W-boson and a bottom quark, i.e. $t \to W^+b$ and $\bar{t} \to W^-\bar{b}$. Hence, a W^+- and a W^--boson are produced in $t\bar{t}$ events and mimic the SM W^+W^- production. The cross section of $t\bar{t}$ production is larger than the production of single top quarks, the ATLAS collaboration measured $\sigma(t\bar{t}) = 176 \pm 5(\mathrm{stat.})^{+14}_{-11}(\mathrm{sys.}) \pm 8(\mathrm{lumi.})$ pb [20] and it thus clearly dominates the W^+W^- background contribution from top quarks. Figure 1.10 shows the leading gluon-fusion $t\bar{t}$ production process.

Di-Boson Production

Another background to the SM W-pair production arises from the production of WZ and ZZ di-boson pairs. These processes occur less often than the W-pair production in the

[5]The concept of jets will be discussed in Section 3.4.

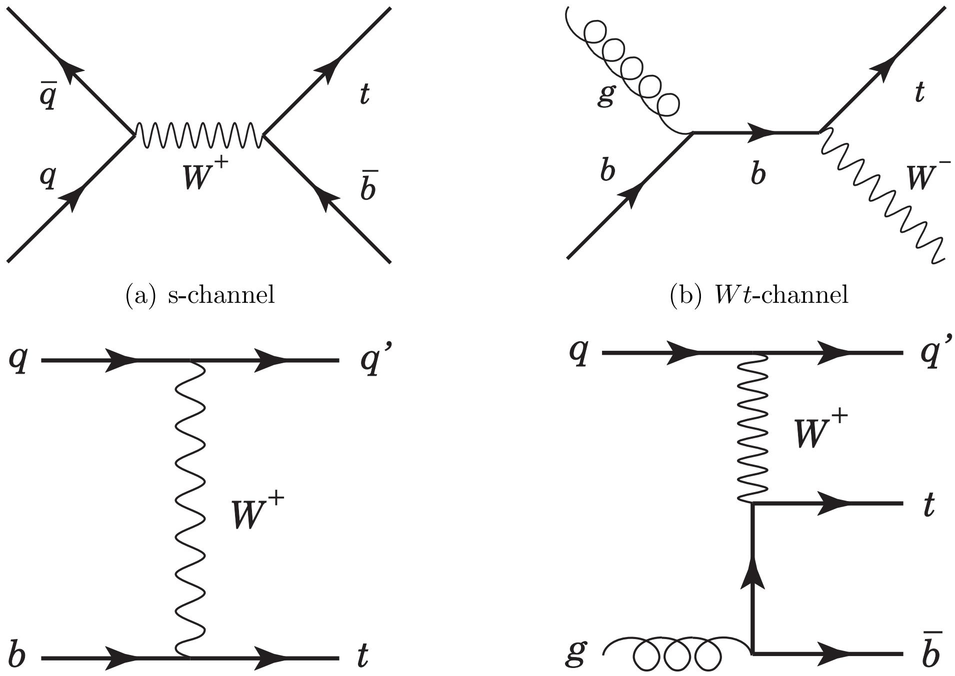

(a) s-channel

(b) Wt-channel

(c) t-channel

(d) t-channel

Figure 1.9: The Feynman diagrams of the single top quark production processes at the LHC are shown.

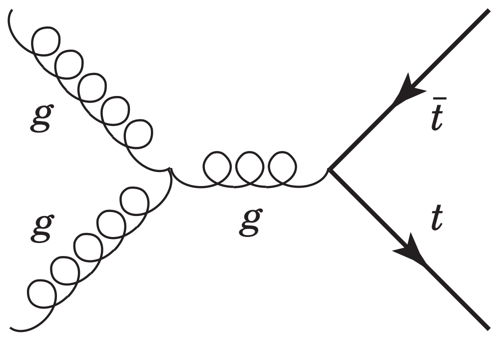

Figure 1.10: The Feynman diagrams of the leading gluon fusion $t\bar{t}$ production at the LHC is shown, with the subsequent decay in the di-muon final state.

Standard Model, however, they can also mimic a W^+W^- signal if part of the final states stay undetected in the experiment. However, since the di-boson production rates are very low compared to the other background sources it remains the smallest of all background contributions.

1.5 Summary

We gave an overview over the structure and the elementary particles of the Standard Model of particle physics. Besides the well established particles, the Higgs boson was briefly discussed as well. With the experimental setup introduced in the subsequent chapter, it is possible to test the SM at center of mass energies of 7 TeV and discover or rule out the SM Higgs boson. The measurement of W^+W^- production at this collision energy is an important contribution to both. Via the triple gauge couplings, it is sensitive to the non-abelian structure of the weak force and hence presents an important test of the Standard Model. In addition, the SM W^+W^- production will be an essential background that needs to be controlled in a search for the SM Higgs boson. At the Tevatron collider in the United States the Standard Model W-pair production has already been measured at the center of mass energy of 1.96 TeV and found to be in agreement with the Standard Model predictions. In this thesis, we will present a W-pair cross section measurement at 7 TeV, the highest center of mass energy reached yet in a collider experiment.
A precise measurement of the W^+W^- production cross section requires however a detailed understanding of the corresponding signatures in the experiment. We choose to measure the cross section of the process $pp \to W^+W^- \to \mu^+ \, \nu_\mu \, \mu^- \, \bar{\nu_\mu}$. The discussed J/ψ particle makes an excellent tool to study the identification of muons in the experiment.

CHAPTER **2**

The ATLAS Detector at the Large Hadron Collider

2.1 CERN

After the end of the second world war the world tried to prevent future devastating wars by creating various international organizations to increase and strengthen international relationships and survey. Particularly the demonstrated massive destruction power of nuclear weapons was a major concern threatening reinvigorating european civilizations. On 29th of September 1954, *Le Centre pour la Recherche Nuclaire*, abbreviated to CERN was founded by the first member states: Belgium, Denmark, France, the Federal Repulic of Germany, Greece, Italy, the Netherlands, Norway, Sweden, Switzerland, the United Kingdom and Yugoslavia. This organization should insure that the european nations work together on nuclear research of a pure scientific and fundamental character [65]. The tasks of CERN were defined to

- **Research**: Seek and find answers to the origin and nature of our universe.
- **Technology**: Advance the frontiers of technology.
- **Collaboration**: Bring nations together through science.
- **Education**: Train the next generation scientists.

In the following decades, CERN proved to be one of the most successful international cooperations of history, counting to date 608 contributing universities and institutes in 113 countries around the world. Developments and research at CERN led to the discovery of many new particles and phenomena of nature, yielding a new and more profound understanding of the building blocks of matter and our universe and was rewarded with 5 Nobel Prizes up to now.

Just two years after the establishment of CERN in Geneva the first accelerator, a synchrocyclotron with a center of mass energy of 600 MeV became operational. In 1959 the Proton Synchrotron, PS started up as the highest energy particle collider in the world, supplying experiments with beam energies of 28 GeV. Also the world's first proton-proton collider ISR (Intersection Storage Ring) was designed and built at CERN with a circumference of about 940 meters. 1976 marks the next mile stone in CERN history, with the SPS (Super Proton Synchroton) becoming operational. This seven kilometer circumference accelerator was originally designed to collide protons. However, at a later stage it ran as a proton-antiproton collider which would provide the data to discover the $W^{\pm}$- and Z-bosons, awarding a Nobel prize to Carlo Rubbia and Simon van der Meer in 1984.
LEP, the Large Electron Positron collider was commissioned in 1989 and heralded yet a new era at CERN. Excavating the 26.7 km long tunnel between 45 and 170 meters under the earth's surface, that accommodated the highest energy lepton collider ever built also marked Europe's largest civil-engineering project at the time. In the end of the year 2000 the very successful LEP collider and its dedicated experiments were closed to make way for the next generation accelerator.

2.2 The LHC

The Large Hadron Collider (LHC) is located in the former LEP tunnel. Being a proton-proton collider, two rings are needed to accelerate the particles, as opposed to particle-antiparticle colliders, such as LEP, where a single ring design is sufficient. To fit the LHC in the former LEP tunnel, twin bore magnets were used that consist of two sets of coils and beam pipes within the same mechanical structure and cryostat [21]. The first design studies of this new proton-proton collider at CERN reach back to the early 80's of the last century. The LHC consists of 1232 superconducting dipole magnets designed to create a magnetic field of upto 8.33 Tesla. The magnets are cooled down to 1.9 Kelvin using superfluid helium. The technology for this ultra cold superconductors was originally developed for the french Tokamak Tore Supra fusion reactor and for the first time adopted to particle colliders. With this magnetic field strength a center of mass energy of 14 TeV is reached, a factor seven larger than the energy of the Tevatron proton-antiproton collider at FermiLab in the United States [26]. To accelerate proton beams up to 7 TeV the particles need to be injected in the LHC with an energy of 450 GeV. Protons with this injection energy are highly cost-efficiently provided by the previous generation CERN hadron accelerators. A linear accelerator, or linac takes ionized hydrogen atoms and pre-accelerates them to 50 MeV before they are boosted to 1.4 GeV by the PS booster. In the PS itself, the bunches of protons are then accelerated to 25 GeV before they enter the SPS where the bunches are collected and accelerated up to the LHC injection energy. With a bunch spacing of 25 ns the LHC can hold 2808 bunches of 10^{11} protons each, for each beam. The resulting design luminosity $\mathcal{L} = 10^{34}\,\mathrm{cm}^{-2}\,\mathrm{s}^{-1}$ is an important key figure of the machine. The high center of mass energy together with the high luminosity will provide the dedicated experiments with the means to spot and measure rare processes of nature being the key to understand the fundamentals of our world.

In addition to protons, the LHC and its accelerator chain were conceptualized such, that they can accelerate and collide heavy ions as well. The current LHC schedule foresees 6 to 8 weeks of heavy ion runs each year. During these periods, atomic lead nuclei are collided in the bunch crossing points of the LHC. The focus of LHC operation lies however on colliding proton bunches. The beams are collided in four bunch crossing points along the LHC. Four experiments are situated at these bunch-crossing points, see Figure 2.1. A brief summary of the four experiments is given here in alphabetic order:

- **ALICE** is an experiment designed for heavy ions collisions to study the characteristics of an extremely early state of matter in our universe [23].
- **ATLAS** and **CMS** are multi purpose detectors designed to explore the full spectrum of proton-proton physics. However, they have been shown to also substantially contribute to heavy ion studies. A detailed description of ATLAS follows in the subsequent section while for further information on CMS, the reader is referred to [24].
- **LHCb** is a single arm spectrometer dedicated to the study of rare B meson decays [25].

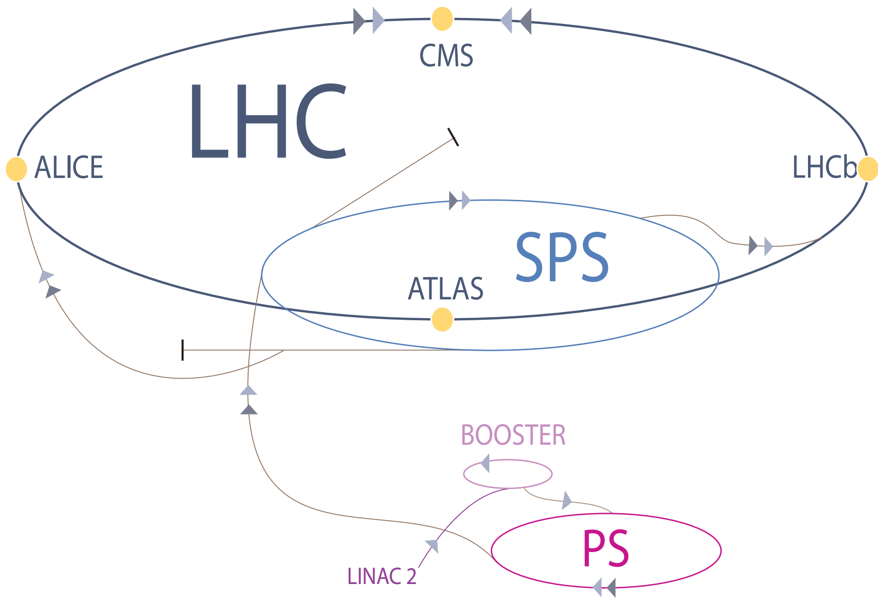

Figure 2.1: A schematic view on the LHC accelerator chain with the location of the four major experiments is shown.

Only 9 days after the first circulating beams in September 2008, a faulty electrical connection between 2 dipole magnets sparked which led to a sudden vaporization of the cooling helium causing severe damage to the machine. It took over a year to replace and repair 53 damaged dipole magnets and install additional safety systems to prevent

similar incidents in the future. After all connections between the magnets were thoroughly checked it was decided to run the machine in 2010 and 2011 only up to beam energies of 3.5 TeV. In the scheduled longer technical shutdown of the LHC that will follow a first data taking period, all dubious connection will be replaced which will allow the machine to reach its design beam energy of 7 TeV after the shutdown.
However, the performance of the LHC since its restart in March 2010 is remarkable and exceeded the most optimistic predictions. The aim of providing the large LHC experiments with an integrated luminosity of 1 fb^{-1} of collision data by the end of 2011 was already reached in spring 2011 as shown in Figure 2.2(b). Since then, the luminosity of the machine could be increased even more and over 5 fb^{-1} were recorded before October 2011.

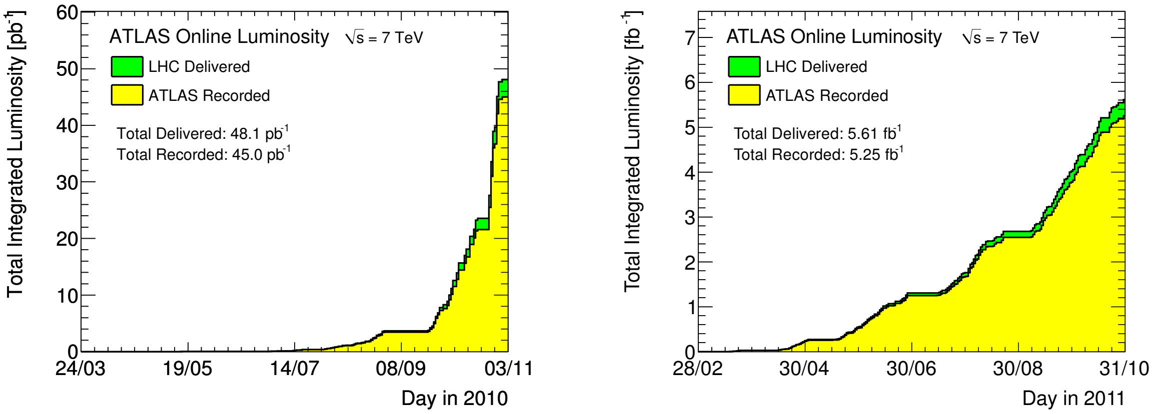

(a) integrated luminosity in 2010

(b) integrated luminosity in 2011

Figure 2.2: The delivered integrated luminosity of the LHC as well as the fraction recorded by ATLAS is shown by days since the restart of the machine in March 2010 up to October 2011.

2.3 The ATLAS Detector

ATLAS (A Toroidal LHC ApparatuS) is a detector designed to fully exploit the potential of the LHC. Its goals are diverse and reach from improved measurements of the Standard Model and the properties of its known particles to new physics that might unveil at these energies. As a central benchmark to establish the performance of ATLAS the search for the Standard Model Higgs particle was chosen. Together with the very high interaction rates of the LHC resulting in high particle multiplicities and radiation doses, this led to the following requirements for the ATLAS detector [22]:

- the detector elements and electronics need to be fast and radiation-hard.
- a highly efficient trigger, providing sufficient background rejection is indispensable to cope with the high luminosities delivered by the LHC.
- high detector granularity is required to handle the particle fluxes and overlapping events.
- a large acceptance with full azimuthal angle coverage is needed for all major subsystems.
- a good charged-particle momentum resolution is required next to a high reconstruction efficiency.
- good electromagnetic calorimetry for electron and photon identification is needed in addition to hadronic calorimetry for precise jet and transverse energy measurements.
- a highly efficient muon identification is essential.

The last point is one of the key aspects of this thesis and will be discussed in detail in Chapter 4 and 5.

To meet these requirements, ATLAS consists of multiple sub-detector systems illustrated in Figure 2.3. The individual subsystems are arranged in cylindrical layers around the beam pipe which form the detector barrel. On each side of the barrel the subsystems are completed by wheels perpendicular to the beam pipe, the end-caps. The individual subsystems can be grouped into three sub-detectors. Closest to the beam pipe, track measurements are performed by the Inner Detector (ID). The calorimeters surround the ID and measure the particle energies. The Muon Spectrometer is the outermost system, a tracking device to measure the tracks of traversing muons. It also defines the dimensions of ATLAS, which is with its 44 times 25 meters the largest of the LHC experiments. The design resolution and coverage of the individual systems are summarized in Table 2.1. After the coordinate system of ATLAS is introduced, all detector systems will be discussed in the given order.

As shown in Figure 2.2, ATLAS had a remarkable start of collision data taking, with over 93 % of the provided luminosity being recorded in the first year. The individual detector systems proofed to work reliably. Table 2.2 shows the time fraction the sub-detectors were operational [69]. All systems show an uptime of $> 96\,\%$.

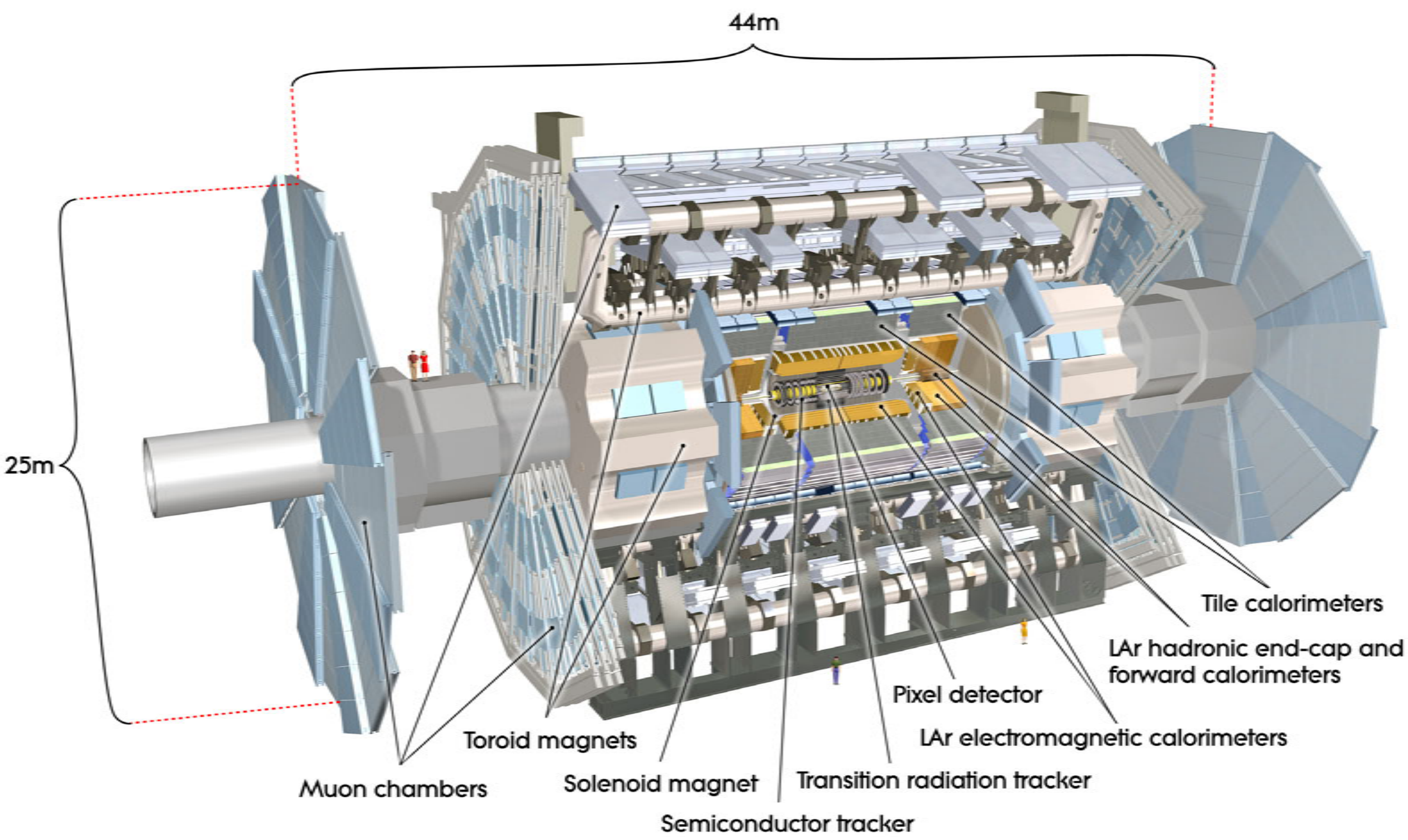

Figure 2.3: A cut-away view of the ATLAS detector. Sub-detector systems are labeled.

detector component	η coverage	design resolution
Inner Detector	± 2.5	$\sigma_{p_T}/p_T = 0.05\,\% \times p_T \oplus 1\,\%$
Pixel	± 2.5	
SCT	± 2.5	
TRT	± 2.0	
EM calorimeter	± 3.2	$\sigma_E/E = 10\,\%/\sqrt{E} \oplus 0.7\,\%$
Hadronic calorimeter		
barrel + end-cap	± 3.2	$\sigma_E/E = 50\,\%/\sqrt{E} \oplus 3\,\%$
forward	$3.1 < \lvert\eta\rvert < 4.9$	$\sigma_E/E = 100\,\%/\sqrt{E} \oplus 10\,\%$
Muon Spectrometer	± 2.7	$\sigma_{p_T}/p_T = 10\,\%$ at $p_T = 1$ TeV
MDT	± 2.7	
RPC	± 1.05	
TGC	$1.05 < \lvert\eta\rvert < 2.7$	
CSC	$2.0 < \lvert\eta\rvert < 2.7$	

Table 2.1: The requirements on coverage and resolution are listed for the individual subsystems of ATLAS.

detector component	readout channels	operational
Inner Detector		
Pixel	$\approx$ 80.4 million	$\approx 96.8\,\%$
SCT	$\approx$ 6.3 million	$\approx 99.1\,\%$
TRT	$\approx$ 351000	$\approx 97.5\,\%$
EM calorimeter	173312 [1]	$\approx 99.8\,\%$
Hadronic calorimeter		
barrel + end-cap	15484	$\approx 97.5\,\% + 99.8\,\%$
forward	3524	$\approx 99.8\,\%$
Muon Spectrometer		
MDT	354000 [2]	$\approx 99.7\,\%$
RPC	373000	$\approx 97.0\,\%$
TGC	318000	$\approx 98.1\,\%$
CSC	30700	$\approx 97.7\,\%$

Table 2.2: The number of readout channels is listed together with the approximate fraction of time the individual detector system was operational during data-taking.

[1] This number includes the 9344 channels of the presampler.

[2] The quoted numbers are the design values for the fully operational MS. There are about 50 chambers that have not been installed yet and are foreseen to be integrated in the MS in the coming technical shutdown the end of 2011 and 2012 [83]. These chambers are situated in the transition region between barrel and endcap stations.

2.3.1 Coordinate System

The nominal interaction point (IP) defines the origin of the right-handed ATLAS coordinate system. The positive x-axis is pointing towards the center of the LHC ring, while the positive y-axis is pointing upwards towards the ground surface. The x-y plane is hence perpendicular to the beam pipe and is referred to as the transverse plane. The positive z-axis is defined to point along the beam pipe towards the west, thus in the counter-clockwise direction.
In view of the ATLAS geometry, a cylindrical coordinate system is often used with azimuthal (ϕ) and a polar angle (θ) in addition to a radius R. These coordinates are defined as:

$$\begin{aligned} R &= \sqrt{x^2 + y^2} \\ \phi &= \arctan\left(\frac{y}{x}\right) \\ \theta &= \arccos\left(\frac{z}{R}\right) \end{aligned} \tag{2.1}$$

where $\phi \in [-\pi, \pi[$ and $\theta \in [0, \pi]$. Instead of θ the pseudorapidity η is commonly used, that is defined as

$$\eta = -\ln\left(\tan\frac{\theta}{2}\right) \tag{2.2}$$

i.e. $\eta \in]-\infty, \infty[$. A convenient property of the pseudorapidity is that the production of charged particles is approximately flat in η. Also the difference in η of two massless particles is Lorentz invariant.

2.3.2 Inner Detector

The ATLAS Inner Detector is a tracking device designed to precisely measure traversing charged particles with a high spatial and momentum resolution. It is further capable in reconstructing primary and secondary vertices. Its first cylindrical detector layer is as close as 5 cm to the beam pipe to insure a high vertex resolution. The inner most subsystem is a silicon pixel detector, which is surrounded by a silicon strip detector (SemiConductor Tracker, SCT). The third, outermost subsystem is a transition radiation detector (Transition Radiation Tracker, TRT). The three detector systems are embedded in a solenoidal magnetic field with a field strength of 2 T parallel to the beam axis. A cut-away view of the ID is shown in Figure 2.4.

Pixel Detector

The ATLAS Pixel Detector is the inner most system with the first of its three layers, the so-called B-Layer reaching about 5 cm to the interaction point, as illustrated in Figure 2.4. The three barrel layers are completed with corresponding end-caps on each side, which leads to an expected number of three hits for charged collision products. Being so close to the interaction point implicates a high granularity to match the requirements on vertex and track momentum resolution. A total of over 80 million readout channels

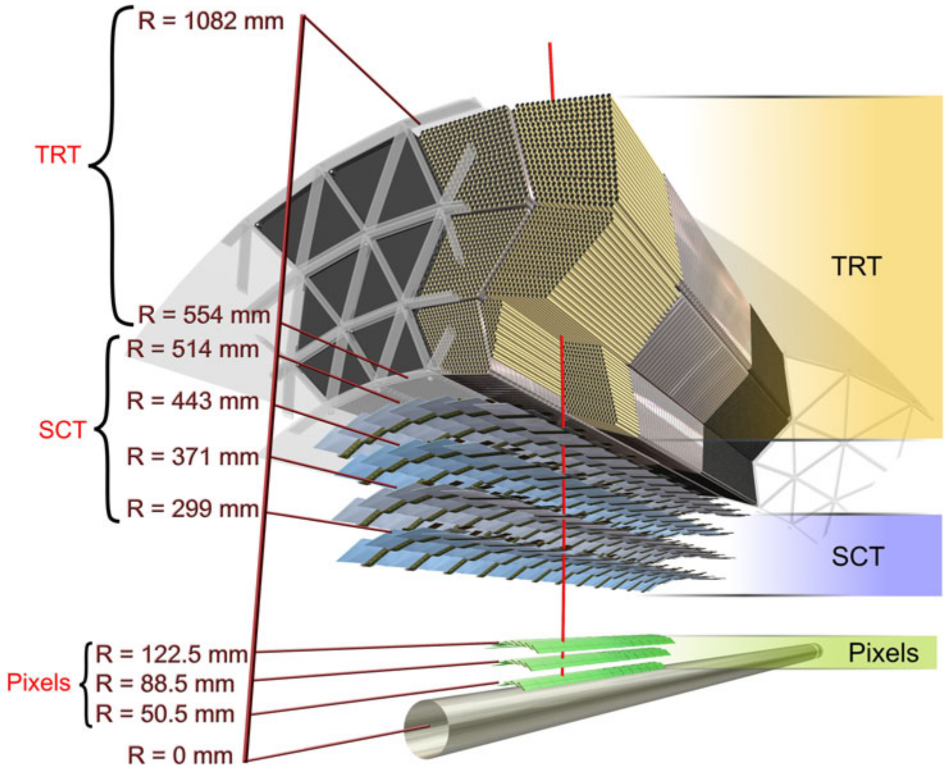

Figure 2.4: A sketched cutaway of the ATLAS Inner Detector showing the setup of the three subsystems in the barrel. The tube at $R = 0$ is the beam pipe.

is deployed. The barrel layers and disks are equipped with 50×400 μm^2, respectively 50×600 μm^2 semiconducting silicon pixels providing a design hit resolution of 10 μm in $R - \phi$ and 115 μm in z. Traversing charged particles ionize the charge depleted zone of the sensors, creating electron-hole-pairs in the silicon, which are separated by the applied potential. The induced signal is measured as time-over-threshold by a discriminator in the readout electronics after the signal was amplified.
The efficiencies of the individual barrel layers and end-cap disks measured on early data in 2010 are shown in Figure 2.5(a). “Dead modules are excluded from the association efficiency computation, but otherwise dead regions contribute to the inefficiency. The full efficiency of B-Layer is due to the track selection, the lower efficiency for the most external disks is mainly due to inefficient regions on some modules. Error bars are smaller then marker sizes.” [3] [70] The noise occupancy is shown in Figure 2.5(b) as a function of time, using randomly triggered events with empty bunches between April and May 2010. The noise rate is dominated by few pixels [4] which are detected on a run-by-run basis by offline prompt calibration and masked during the bulk processing. For the bulk processing, the

[3] The quoted text is literal text from the ATLAS web side.
[4] typically 300 - 1500 out of 80 million,

remaining noise occupancy is less than 10 hits per pixel per bunch crossing, corresponding to less than 0.2 noise hits per event when reading out 5 bunch crossings [70].

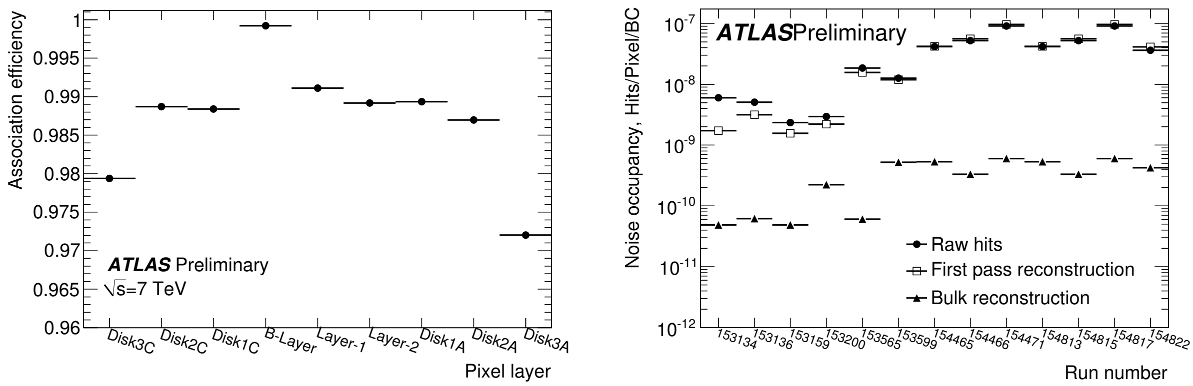

(a) Pixel detector efficiency

(b) Pixel detector noise rate

Figure 2.5: The efficiency for a track to have a hit associated when crossing a Pixel Detector layer is shown in (a). The noise rate for the Pixel detector measured on empty bunches is shown in (b). The plots are taken from [70].

Semiconductor Tracker

The SCT, surrounding the Pixel Detector provides typically four space point measurements (8 hits) of traversing charged particles. To insure a good momentum resolution, extending the Pixel Detector measurements is particularly important for high momentum particles, where the curvature of the track in the magnetic field is small. The SCT barrel consists of 4 cylindrical detection layers while each end-cap is made of nine detection disks. As for the Pixel Detector, silicon is used as detection material, however the SCT is segmented in strips. This design limits the number of readout channels and is hence cost efficient. The SCT detector modules consist of two silicon sensors glued back-to-back with an angle of 40 mrad providing a 2 dimensional measurement. In the barrel the strips on one side of the modules are aligned parallel to the beam axis, while the strips on one side of the disk modules run radially. Each sensor is made of 768 strips with a strip pitch of 80 μm. The design resolution is 17 μm in $R - \phi$ and 580 μm in z.
The intrinsic SCT module efficiency has been measured on data to be on average larger than 99.7 %. The performance is detailed at [71] and shown in Figure 2.6. The "hit efficiency is the number of hits per possible hit, where dead modules and chips are taken into account. [...] The efficiency is shown for two different types of tracks: SCT stand-alone and Inner Detector combined tracks, both with the requirement of a transverse momentum of above 1 GeV. For stand-alone tracks we demand at least 7 SCT hits (not including the hit under test for efficiency) while for combined tracks at least 6 SCT Hits are required. The efficiencies in layer 0 inner and 3 outer are biased for the SCT stand-alone tracks as holes beyond the last measurement are not counted." [71]

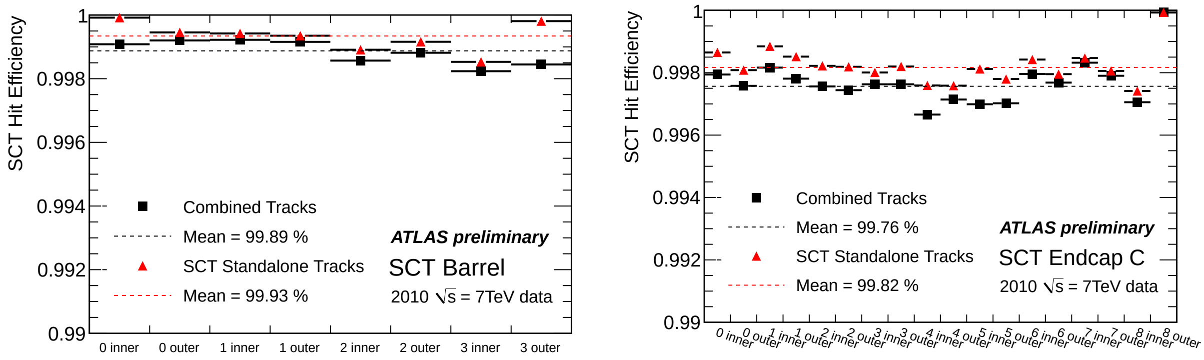

(a) SCT barrel

(b) SCT end-cap

Figure 2.6: The hit efficiencies of the SCT barrel (a) and end-cap C modules (b) are shown. Since the performance differences of the two end-caps are negligible, the efficiencies of only one end-cap is shown. The plots are taken from [71].

Transition Radiation Tracker

The outermost ID subsystem uses two independent detection principles. It contributes to the ID track measurement up to $|\eta| = 2$ using wire chambers while also allowing for the identification of particles by the emitted transition radiation.
The TRT barrel consists of 73 layers of 144 cm long straws parallel to the beam axis, while each end-cap contains 18 disks of 37 cm long straws which are radially aligned. The straws are gas filled tubes with a 4 mm diameter which are kept as cathodes on -1530 V. The gold plated, 31 μm tungsten wire in the center of each tube, supported at the straw ends, is kept on ground potential. In the barrel, the wires are divided into two halves at $\eta = 0$ to deal with the high occupancies. Traversing charged particles ionize the Xe:CO_2:O_2 (70:27:3 %) gas mixture and the free charges drift towards the wire under the applied potential. The resulting induced current is measured. The TRT provides only a $R - \phi$ measurement. The design resolution is 130 μm.
The TRT straws are coated by materials with different dielectrical constants, causing a charged particle to emit X-ray photons when traversing the boundaries between these material layers. These photons are referred to as transition radiation. The amount of emitted transition radiation depends on the particles Lorentz factor $\gamma = E/m$. A charged pion, carrying 273 times the mass of an electron produces hence a significantly smaller amount of transition radiation, which is absorbed by the Xenon in the gas mixture of the tubes and yield much larger signal amplitudes than traversing ionizing particles. Thus, tracking signal and transition radiation are distinguished by two separate thresholds in readout electronics of the TRT.

2.3.3 Calorimeter

As shown in Table 2.1, the ATLAS calorimeters cover the wide range up to $|\eta| = 4.9$. They are designed to measure the energy of all incoming particles by absorbing them. Muons and neutrinos are the only known particles that are not absorbed and can traverse the calorimeter [5]. In addition, their total minimal thickness of 11 nuclear interaction lengths (λ) [6] limits punch-through into the muon system. Combining the ID and calorimeter measurements provides an identification of electrons, photons and gives probabilities for a jet to result from a b or τ decay.
Different techniques depending on the radiation environment are used to meet the physics requirements, leading to 6 calorimeters that can be grouped into electromagnetic (EM) and hadronic calorimeters and are displayed in Figure 2.7. ATLAS uses sampling calorimeters, which consist of alternating layers of absorbers, dense materials used to degrade the energy of the incident particle and active materials that are used to measure the deposited energy.

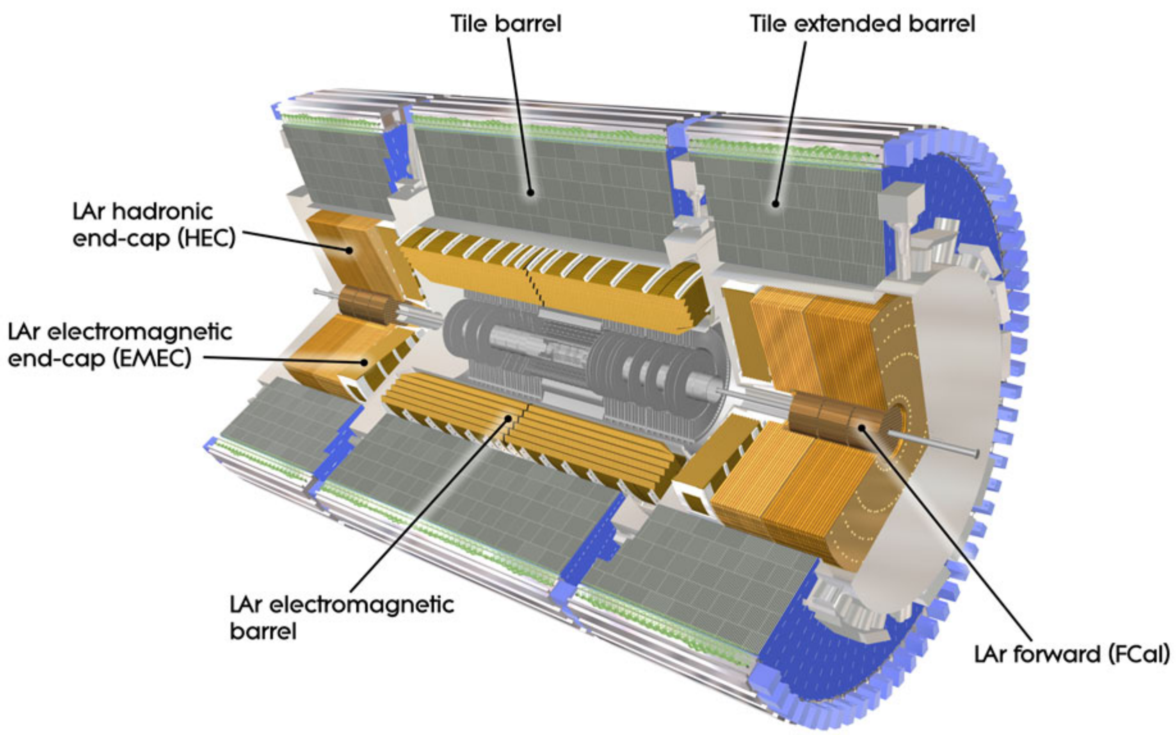

Figure 2.7: A cut-away view of the ATLAS calorimeters, with the Inner Detector in the center.

[5] Traversing the calorimeter requires the muons to have an energy of at least 3 GeV.
[6] The thickness is a function of η and increases to more than 18 λ for the forward regions. The nuclear interaction length λ is defined as the mean path length in which the number of relativistic charged particles is reduced by a factor $1/e$.

Electromagnetic Calorimeter

The ATLAS EM calorimeter is attached to the solenoid enclosing the ID. Direction and energy of electromagnetic showers caused by Bremsstrahlung and pair production of incident electrons and photons are precisely measured using lead as absorber and liquid argon (LAr) as the active material. An accordion shape geometry was chosen for the alternating layers providing complete ϕ symmetry without azimuthal cracks. The first of its three layers in barrel and end-caps has a finer granularity to allow for electron, photon and pion identification. The thickness corresponds to more than 22 radiation lengths (X_0) [7] in the barrel and more than 24 X_0 in the end-caps. The covered pseudorapidity range and expected energy resolution is listed in Table 2.1. For $|\eta| < 1.8$ a presampler detector in front of the first EM calorimeter layer corrects for the energy electrons and photons lost upstream of the calorimeters.
A cell occupancy map of the EM calorimeter, measured on collision data in April 2010 is shown in Figure 2.8 and published at [72].

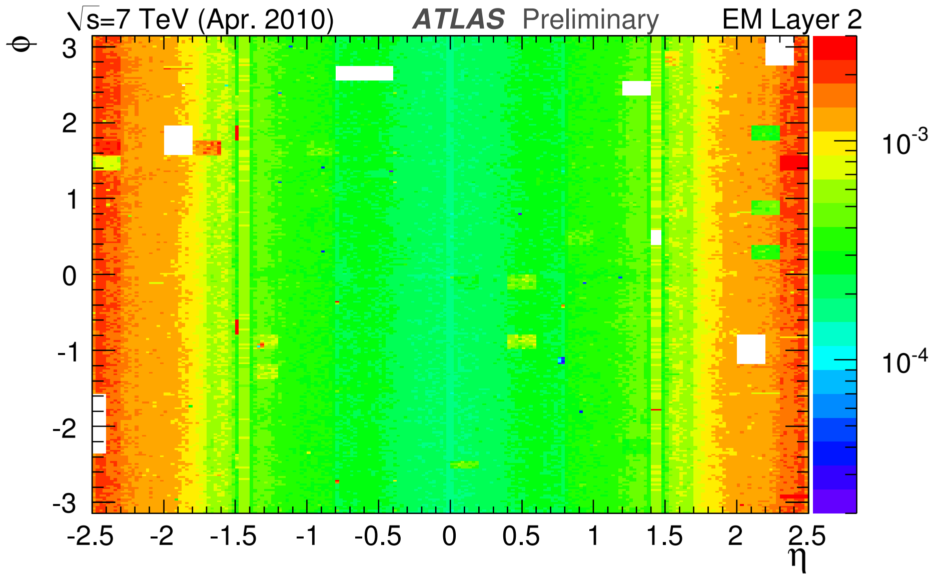

Figure 2.8: The cell occupancy in the EM calorimeter is shown. The plot is taken from [72].

Hadronic Calorimeter

Strong interacting particles deposit only a small fraction of their energy in the EM calorimeter. The hadronic calorimeter is used to measure energy and direction of hadrons through their strong and electromagnetic interactions. Since hadronic showers are wider and longer than their electromagnetic counterparts, the hadronic calorimeters allow for a coarser granularity but are significantly more massive. The barrel, which is called Tile

[7] The radiation length X_0 is defined as the mean path length in which the energy of a high energetic electron is reduced by a factor $1/e$.

Calorimeter extends from an inner radius of 2.28 m to an outer radius of 4.25 m, covering the pseudorapidity range of $|\eta| < 1.0$. It is extended by two additional barrels in the range $0.8 < |\eta| < 1.7$ as shown in Figure 2.7. Steel is used as the absorber while scintillating tiles measure the signal, which is read out by wavelength shifting fibres into photomuliplier tubes. The corresponding end-caps, one on each side, use copper as absorber and LAr as the active medium, sharing some infrastructure with the EM calorimeter end-caps. They are hence referred to as the LAr hadronic end-cap calorimeters (HEC). Figure 2.9 shows the "mean value of the E/p variable as a function of η, integrated over all p ranges for 2010 Data and Monte Carlo simulation. E refers to the energy deposited in the Tile Calorimeter ($|\eta| < 1.7$) by the isolated charged particles with momentum p and pseudorapidity η (excluding the energy deposited in the scintillators). Charged particles have been selected applying a MIP-like signal requirement for the energy deposition in the LAr calorimeter." [73] The E/p distribution in ϕ is to a good approximation flat and not shown here.
The pseudorapidity coverage of the ATLAS hadronic calorimeter is extended by the Forward Calorimeter (FCal) up to $|\eta| = 4.9$ to improve the measurement of the missing transverse energy which is caused by collision products that stay undetected, like neutrinos. The FCal consists of two end-caps using LAr as the active medium while copper is the absorber in the first layer, being optimized for EM measurements, while the other two layers use tungsten, measuring the energy lost in hadronic interactions.

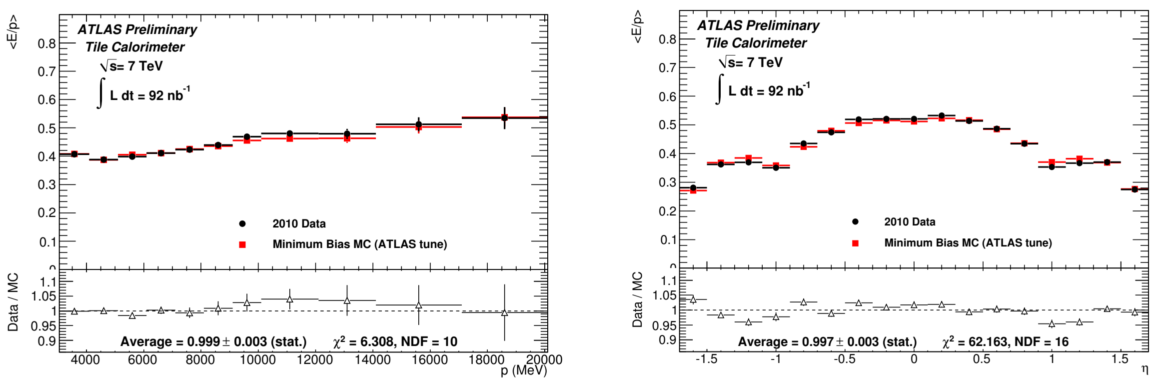

(a) (b)

Figure 2.9: The mean value of E/p is shown as a function of momentum (a) and pseudorapidity (b) for the ATLAS Tile Calorimeter. The bottom plots show the data-Monte Carlo ratio of the mean value of the E/p variable, fitted with a constant function. The errors are statistical. The plots are taken from [73].

2.3.4 Muon Spectrometer

The Muon Spectrometer (MS) is another tracking device. This outermost subsystem of ATLAS was designed to provide a muon trigger as well as a precise muon track re-

		Chamber resolution (RMS) in			Measurements/track	
Type	Function	z/R [mm]	ϕ [mm]	time [ns]	barrel	end-cap
MDT	tracking	35×10^{-3} (z)	–	–	20	20
CSC	tracking	40×10^{-3} (R)	5	7	–	4
RPC	trigger	10 (z)	10	1.5	6	–
TGC	trigger	2 - 6 (R)	3 - 7	4	–	9

Table 2.3: The parameters of the four sub-systems of the ATLAS Muon Spectrometer are shown. The intrinsic time resolution of the individual chambers is quoted. No contributions from signal-propagation or electronics are included.

construction based on measurements in typically 3 stations. Its three cylindrical layers, forming the barrel of the MS are positioned at radii of 5, 7.5 and 10 meters from the beam-axis. They are referred to as the inner, middle and outer station. The corresponding MS end-caps are positioned at z equals ± 7.4, ± 14 and ± 21.5 meters. The spatial MS coverage as shown in Table 2.3 has a few acceptance holes due to support structures. At $|\eta| \lesssim 0.1$ a shaft to provide ID, solenoid and calorimeter services makes the installation of muon chambers impossible. Also in the feet regions of ATLAS at $\phi \approx -1.0$ rad and $\phi \approx -2.0$ rad the support structures of the large toroid and the detector barrel limit the acceptance.
To allow for a precise momentum measurement, a magnetic field is provided by the superconducting air-core ATLAS toroid. Up to $|\eta| < 1.4$ the large barrel toroid provides a field mostly orthogonal to the traversing muon directions. For $1.6 < |\eta| < 2.7$ muon tracks are bent by two smaller end-cap magnets. The pseudorapidity range $1.4 < |\eta| < 1.6$ is commonly referred to as the transition region, where the two magnetic fields of barrel and end-cap toroids are overlapping.
The MS is equipped with high precision tracking chambers and separate trigger chambers. Their η coverage and number of readout channels is summarized in Table 2.1, while the individual chamber resolutions and corresponding measurements per track are listed in Table 2.3. The trigger chambers are required to provide fast and coarse tracking information including a transverse muon momentum estimate as well as bunch-crossing identification. The transverse x-y-view of the barrel detector in Figure 2.10 and the side view of the upper ATLAS quadrant in Figure 2.11 illustrate the location of all individual MS chamber types which are described in detail in the following.

Monitored Drift Tube Chambers

The Monitor Drift Tubes (MDT's) provide precision measurements in the ATLAS MS. Figure 2.12 shows a cut-away view of a typical middle or outer station MDT barrel chamber consisting of two multilayers with three layers of MDTs each. The layer dimensions and sizes of the MDT chambers increase in proportion to their distance from the interaction point. However, a considerable number of specially shaped chambers have been built to minimize acceptance losses in the regions around magnets and support structures. The general layout alternates small and large chambers in ϕ. The naming of the chambers is

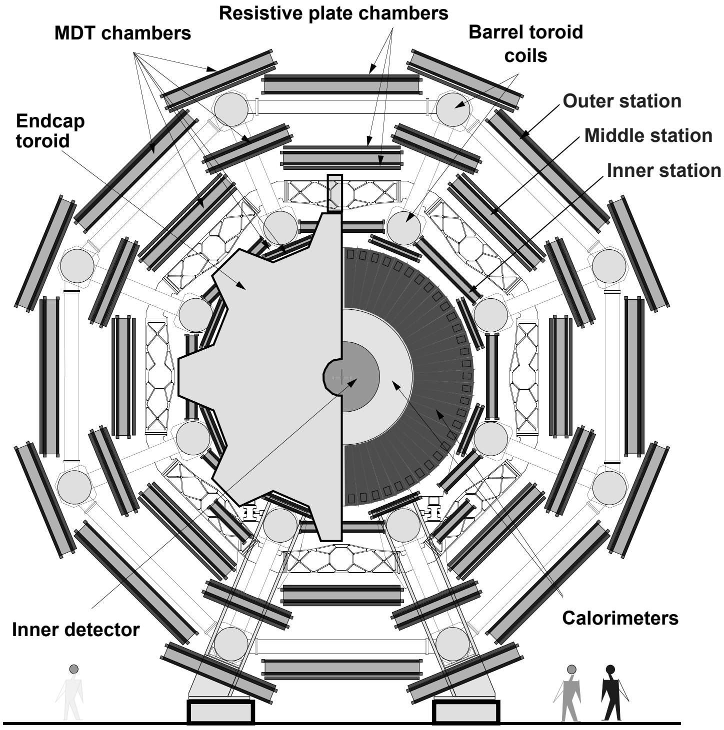

Figure 2.10: The cross section of the ATLAS detector barrel is shown perpendicular to the beam-axis, illustrating the muon system.

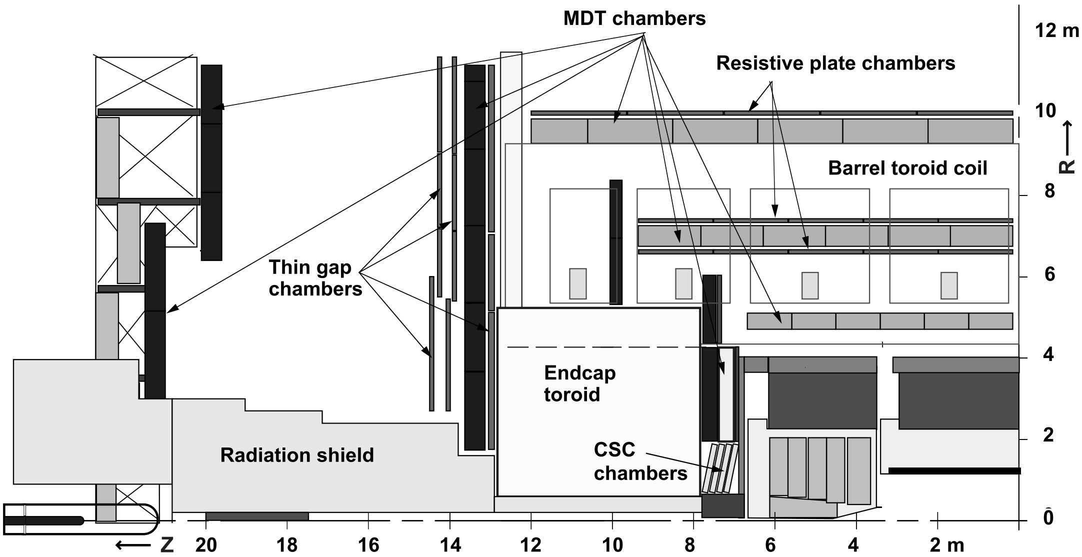

Figure 2.11: The cross section of an upper quadrant of the ATLAS detector is shown parallel to the beam-axis, illustrating the muon system.

based on their location ('B'arrel, 'E'ndcap), their assignment to inner, middle, or outer stations ('I', 'M', 'O') and their size ('S'mall, 'L'arge). A BOL chamber refers thus to a large chamber in the outer station of the barrel. To improve the pattern recognition, the inner station MDT chambers are equipped with four multilayers.
The basic elements of the MDT chambers are the individual aluminum tubes with a 30 mm diameter, pressurized by an Ar:CO_2 (93:7 %) gas mixture at 3 bar. Their individual lengths varies between 1685 and 2820 mm in the barrel inner stations up to 4202 to 6503 mm in the outer end-cap stations. The tungsten-rhenium wire is gold plated and kept at a potential of 3080 V in the center of each tube, while the tubes are on ground potential. Free charges, created by the traversing ionizing muons in the gas, drift through the applied potential and induce a measured current in the central wire. When a predefined threshold in the readout electronics is reached the signal and corresponding time is recorded. The measured time is the drift time of the free charges which is converted into a drift radius, the minimal distance of the traversing muon to the wire. Figure 2.13(a) shows the relation of drift time and drift radius measured in 2010, while the measured drift time spectrum is shown in Figure 2.13(b) [41]. The measurement of the drift circle gives a precise position in one plane with an average tube resolution of 80 μm. The resolution quoted in Table 2.3 shows the average resolution per chamber. The position along the tube is not measured by the MDT's [8].

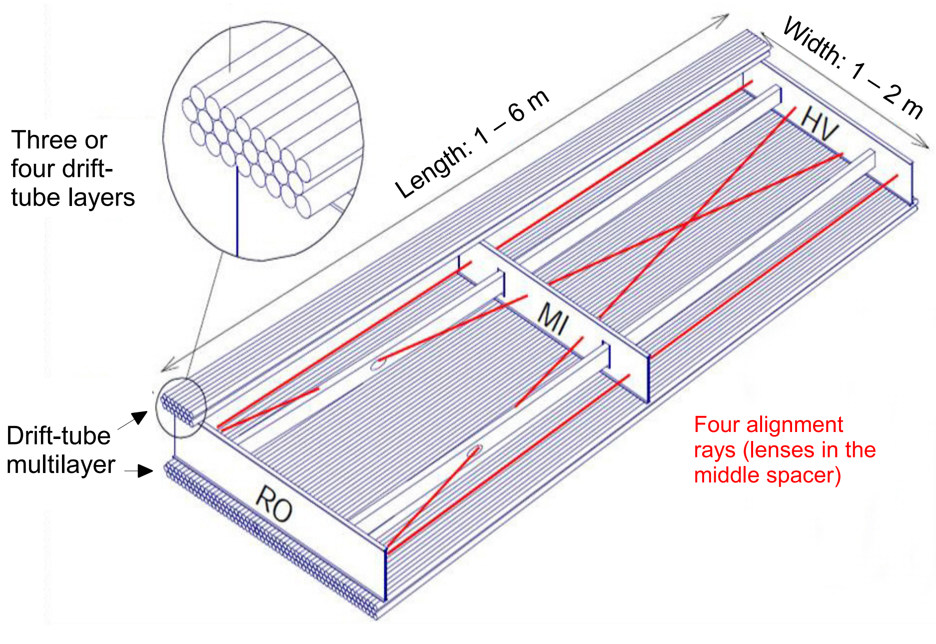

Figure 2.12: A cut-away view of the typical MDT layout. The shown configuration with 2 multilayers of 3 tube layers is used in the barrel middle and outer stations.

[8]Exceptions are the two MDT twin-tube chambers installed for testing in the outer barrel stations. MDT's are paired in these chambers to reconstruct the second coordinate from the two correlated measured times of the individual MDT's, see [64] for details on the MDT twin-tubes.

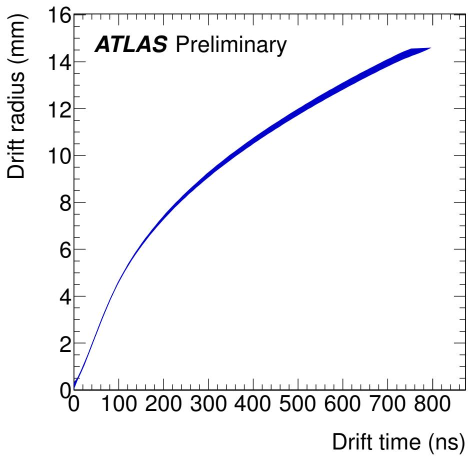

(a) drift radius vs. drift time

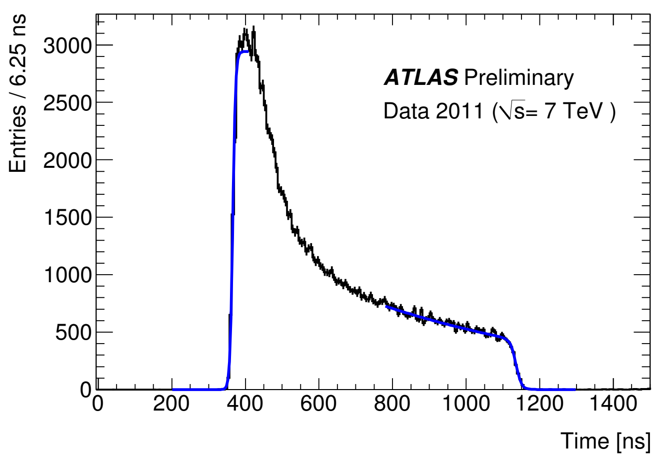

(b) drift time spectrum

Figure 2.13: The drift time - drift radius relation is shown in (a) while (b) shows the drift time spectrum. Note that (b) shows an arbitrary time scale where the drift time starts at around 350 ns. The plots are taken from [41].

Cathode Strip Chambers

The particle fluxes and track density are highest in the forward regions of the detector ($|\eta| > 2.0$). At LHC design luminosity, the counting rates will be too high for the MDT's to provide an efficient measurement in the inner stations in this region. The fast Cathode Strip Chambers (CSC's) replace the MDT inner stations in the region $2.0 < |\eta| < 2.7$. They combine high spatial, time and track resolution (see Table 2.3) with high counting rate capability and low neutron sensitivity. The CSC system consists of 2 disks mounted about 7 m from the interaction point, one on each side of the detector. Each disk consists of 8 small and 8 large chambers alternating in ϕ, resembling the MDT layout.
The CSC's are multi-wire proportional chambers with 30 μm diameter anode wires oriented in the radial direction. Both cathodes are segmented, one in strips parallel and one perpendicular to the wires, providing a two dimensional position measurement. The chambers are filled with an Ar:CO_2 (80:20 %) gas mixture that is ionized by traversing charged particles. The operating voltage is 1900 V. Unlike the MDT's, the wires are not read out. Instead, the induced current in neighboring cathodes provides the signal. Each CSC chamber consists of 4 identical CSC planes providing 4 independent position measurements in η and ϕ for every charged particle traversing a CSC.

Resistive Plate Chambers

The Resistive Plate Chambers (RPC's) are an important complement to the MDT's in the detector barrel, providing a ϕ measurement and a trigger for muons. Two RPC's are mounted on the middle station MDT chambers and one on the outer station MDT chambers, see Figure 2.11. Thus, the three muon trigger stations are formed. The RPC's are gaseous parallel electrode-plate detectors. Two plastic plates are installed with a distance of 2 mm. The chambers are filled with a low cost and nonflammable gas mixture of $C_2H_2F_4$:Iso-C_4H_{10}:SF_6 (94.7:5:0.3 %). The strong electric field of 4.9 kV/mm between the plates allows electron avalanches to form along the path of a traversing charged particle. The signal at the anode is read out via capacitive coupling to metallic strips mounted on the outer faces of the plastic plates.

Thin Gap Chambers

In the end-caps, the muon trigger is provided by the Thin Gap Chambers (TGC's). Four disks in each end-cap provide on average nine measurements per traversing particle. The MDT end-cap inner station has two layers, while the EM stations have 7 layers of TGC's. TGC's are like CSC's multi-wire proportional chambers. The anode wires operated at 2900 V are thin gold wires while the cathodes are made of graphite which are read out using copper strips. Both, cathodes and wires are read out, providing an η and a ϕ measurement. The chambers are operated with a gas mixture of CO_2:n-C_5H_{12} (55:45 %).

2.3.5 Magnets

The ATLAS magnet system provides the magnetic fields in the Inner Detector and the Muon Spectrometer to allow for a momentum measurement of charged particles. It consists of 4 large superconducting magnets, shown in Figure 2.14, with an energy of 1.6 GJ stored. The entire system is 22 m in diameter and 26 m in length, providing a magnetic field over the volume of 12000 m^3. Figure 2.3 indicates where the magnets are located in the detector with respect to the individual sub-detector systems.

Solenoid

The ID is embedded in a 2 T strong axial magnetic field of the ATLAS solenoid, which is operated at 7730 A. The windings of the solenoid lie inside the tile calorimeter volume. It has a total length of 5.8 m with an inner diameter of 2.46 m and an outer diameter of 2.56 m.

Torroids

For the MS a system of three large air-core toroids was designed to provide a magnetic field of approximately 0.5 T in the barrel and 1 T in the end-cap region. A nominal current of 20500 A is needed to reach this field strength. A total mass of 650 tonnes need to be cooled down to 4.6 K, the operational temperature of the superconducting magnets. The barrel toroid is 25.3 m in length and its inner and outer diameters are 9.4 m and 20.1 m, respectively.

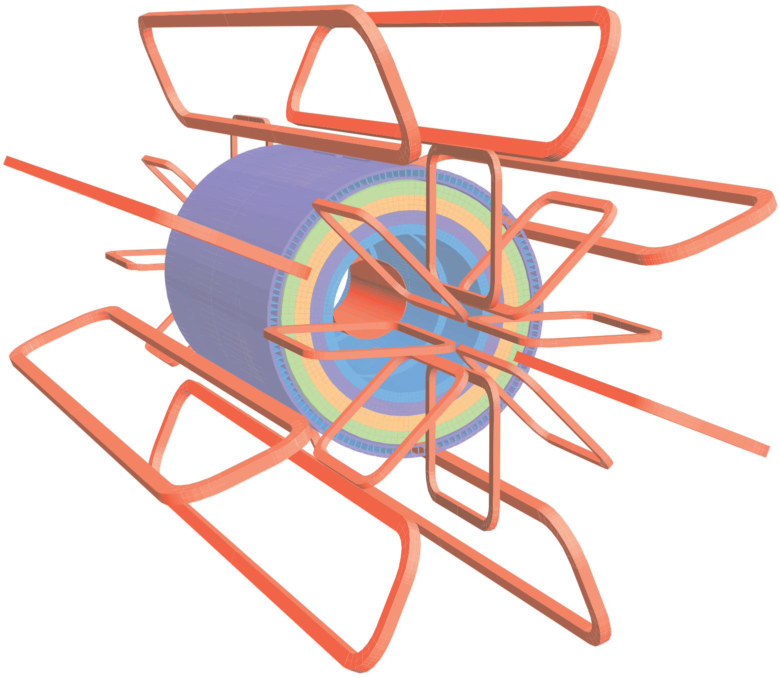

Figure 2.14: A cut-away view on the ATLAS magnet system. The eight toroid coils are shown for barrel and both end-cap toroids. The tile calorimeter is shown in the center, hosting the solenoid.

B-field monitoring

In order to achieve the design momentum resolution of 10 % for a muon with transverse momentum of 1 TeV, stated in Table 2.1, the magnetic field needs to be known to a relative precision of approximately 4×10^{-4} [27]. The magnetic field is modeled with the contribution of all magnet windings and material effects, particularly from the calorimeters. However, the high self-weight of the toroids as well as the inwards directed net Lorentz force of approximately 1400 tonnes per coil lead to a deflection of the toroids. In addition, perturbations of the magnetic field induced by metallic materials e.g. used in the calorimeters, and the transition region $1.4 < |\eta| < 1.6$ where barrel and end-cap toroid fields overlap introduce further uncertainties on the magnetic field map. To counter all these effects, about 1800 Hall probes have been distributed over the entire MS volume, measuring continuously the toroidal field. Figure 2.15 shows the distribution of the sensors in space. The toroid coils and general structure of the ATLAS MS are visible. All sensors have been calibrated to provide exact values of the measured magnetic field strength. Their measurements are compared to the computed magnetic field map and corrections can be applied to the model, that is used to reconstruct muon tracks in the MS.
Measurements of the magnet currents supplement the measurements of the B-field sensors which are analyzed on a daily bases. Figure 2.16 shows the solenoid and toroid currents as a function of time, starting at the day where the first data used in this thesis was

recorded, the 23rd of April 2010 [9]. Each entry corresponds to one day and shows the average current. The values in between 0 and the nominal current correspond to days, where the magnet currents were either ramped up or ramped down. During the technical stop at the end of the year 2010 until the mid February 2011 the magnets were off. Missing entries correspond to failures in the daily B-field sensor monitoring, as for example at the end of June 2010 where the software was updated [10].
A worry were possible aging effects that could change the calibration of the Hall probes over time. The measured values would thus not be reliable any longer. Figure 2.15(b) shows the average $|B|/I$ values of each day between April 2010 and July 2011 on which the toroid current was all day nominal and B-field monitoring data is available. Each entry is the average of all B-field sensor measurements on the corresponding day. Ideally, the value should not change over time since the toroid current is constant. The displayed distribution is indeed extremely narrow with a RMS of 1.5×10^{-4} and we hence conclude, that the B-field sensors work as expected and perform reliably without any visible aging effects.

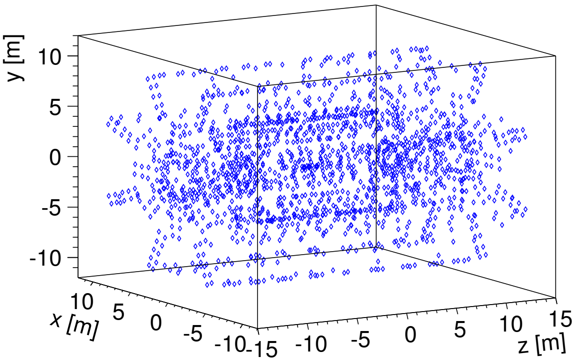

(a)

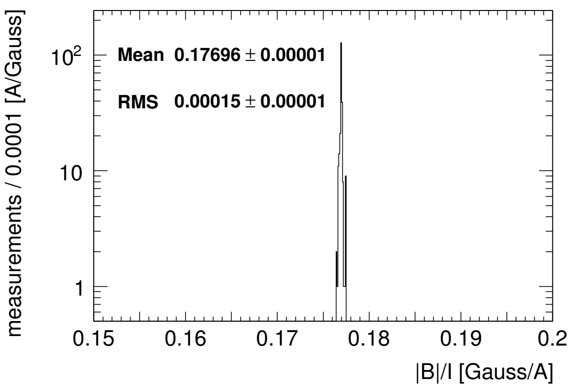

(b)

Figure 2.15: The position of the B-field monitoring sensors in the MS are shown in (a). The projection of the average measured $|B|/I$ as function of time is shown for measurements between April 2010 and July 2011.

2.3.6 Summary

ATLAS had an extraordinary start in the collision data taking phase in 2010. In the past two years, 2010 and 2011 the most optimistic expectations were far exceeded in both, the amount and the quality of the recorded data. After almost 30 years of research, development, construction and commissioning, the ATLAS detector is fully operational

[9] This day marks the start of the first run in 2010's data period B.
[10] The B-field monitoring system was updated to a new operating system leading to major compatibility issues that took multiple weeks to be sorted out.

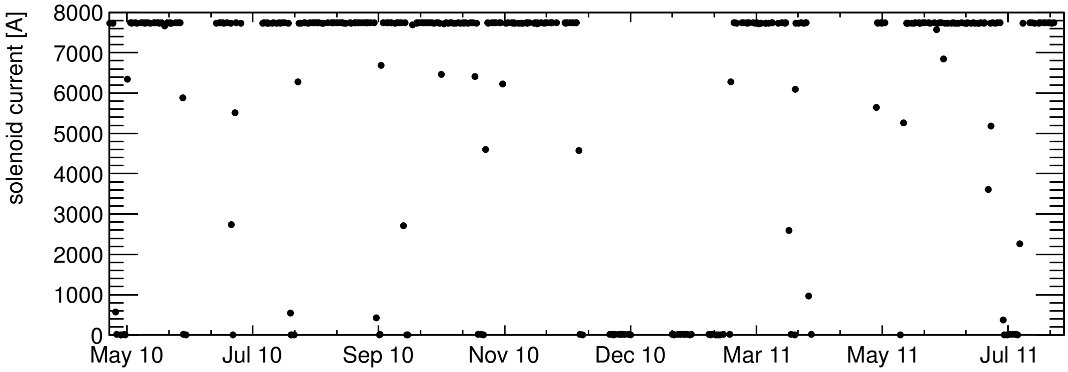

(a)

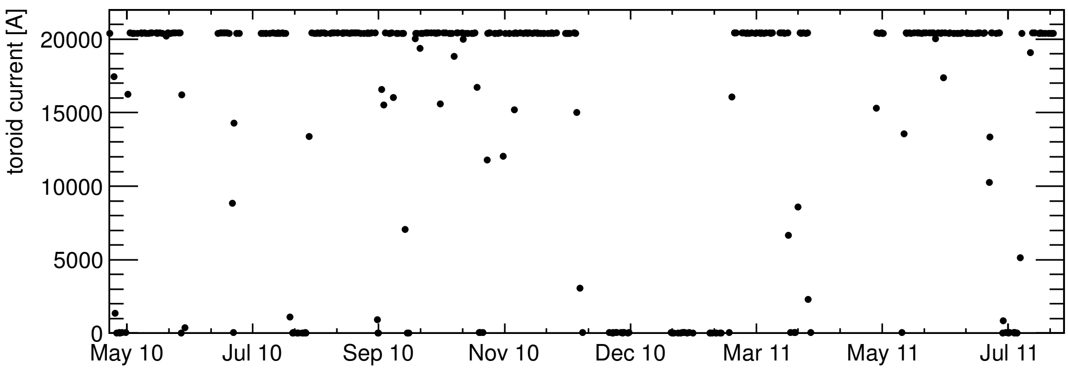

(b)

Figure 2.16: Solenoid and toroid current are shown for the first data taking periods, i.e. end of April 2010 until end of July 2011.

and up for the tasks it was designed for. The ATLAS performance measurements are widely based on collision data and do not rely on Monte Carlo simulations anymore. We discussed in this section the technical aspects and design of the individual subsystems of ATLAS enriched with a selection of performance plots on collision data to illustrate the excellent shape of the detector.

CHAPTER 3

ATLAS Software and Reconstruction

After having laid out the hardware and performance of the ATLAS detector in the previous chapter, the software used to reconstruct physics objects in the recorded data and simulated events will be discussed in this chapter. The main focus here lies on the reconstruction and identification of muons in ATLAS, which will be discussed in 3.6. Before that, the software framework, the trigger, the reconstruction of jets and missing transverse energy as well as Monte Carlo simulations will be described. For tracks reconstructed in the Inner Detector, we refer to [63].

3.1 Athena Software Suite

Athena is the modular software framework of ATLAS [28]. All processing levels of ATLAS data, from high-level trigger (see 3.2) to reconstruction and analysis take place in this framework. Also the simulation and processing of generated events is performed within Athena. After a digitization step, the generated and simulated events follow the same reconstruction chain as is used for data events. Athena provides the common functionality and communication between the embedded individual algorithms and components and thus insures the necessary coherence of the software infrastructure. Its development and maintenance are a continuous effort leading to one major software release and various amounts of sub-releases of the software per year. A release is a snapshot of Athena and all its algorithms at a given time, creating a baseline for performance and physics studies. Throughout this thesis, Athena is used in releases 15 which was used to initially process the data recorded in 2010 and release 16 which was used to reprocess the 2010 data and initially process data recorded in 2011 in the months up to August. The algorithm discussed in Chapter 4 deals with both releases and its developments in the transition from Athena release 15 to release 16. Since release 16 has substantial improvements, particularly in terms of performance, as in improved alignments, calibrations and general performance boosts, we choose to use this release for the performance and analysis Chapters 5 and 6.

3.2 Trigger

An average ATLAS raw data event is of size 1.5 Mbyte. Scaling up to the LHC design collision rate of 40 MHz leads to a total data stream of about 60 Tbyte per second which can not be stored and analyzed by computing systems available at present nor in the near future. A selection of interesting events has to be made in real time that can be stored and made available for analysis. The rate of events that can be written to the ATLAS disks was on average 305 Hz in 2011 [84]. Reducing the event rate by five orders of magnitude without loosing interesting events is a huge challenge which is taken up by the ATLAS trigger system. It is a 3 level trigger system, with each trigger level refining the decisions made by the previous level. The three trigger levels are in the order of their implementation:

1. `L1`: The **Level 1** trigger is a hardware trigger using custom-made electronics. It uses a limited amount of the available detector information to make a decision within 2.5 μs. The rate is reduced from 40 MHz down to 75 kHz. It searches for high p_{T} leptons, hadronicaly decaying τ's, photons as well as jets. Event variables like total transverse energy and large missing energy are constructed. The L1 trigger rates in June 2010 are shown in Figure 3.1 for the unprescaled EM triggers with E_T threshold 2, 3 and 5 GeV, the unprescaled muon triggers with (6 GeV) and without p_T threshold, as well as for the unprescaled jet and τ triggers with an E_T threshold of 5 GeV. The minimum bias trigger had to be downscaled by a factor 20 [74].
   The muon trigger chambers, RPC's and TGC's (see 2.3.4) provide the information for the L1 decision on muons, while calorimeter selections are based on reduced granularity information from all calorimeters. Regions-of-Interest (RoI's), i.e. detector regions where the L1 has identified a trigger object are created and passed on to the L2.

2. `L2`: The **Level 2** trigger is seeded by the RoI's of the L1. All available detector data is used within the RoI's to refine the L1 selection. The L2 reduces the 75 kHz L1 event rate to 3.5 kHz with an average event processing time of 40 ms.

3. `EF`: The **Event Filter** trigger is the last element of the ATLAS trigger chain. The EF selections are based on offline analysis procedures reducing the total event rate to a maximum of 200 Hz, which is then stored on disk. It takes of the order of four seconds to process an event by the EF.

L2 and EF are also commonly referred to as the high level trigger (HLT). Unlike the L1 trigger, the HLT is implemented using commercially available computers and networking hardware. It uses the full granularity of all ATLAS calorimeters as well as the full precision of MS and ID measurements. The event rates of the individual triggers are a function of the instantaneous luminosity the LHC provides and the respective threshold of the triggers. Hence, the trigger transverse momentum and energy thresholds have to be increased for higher instantaneous luminosities.

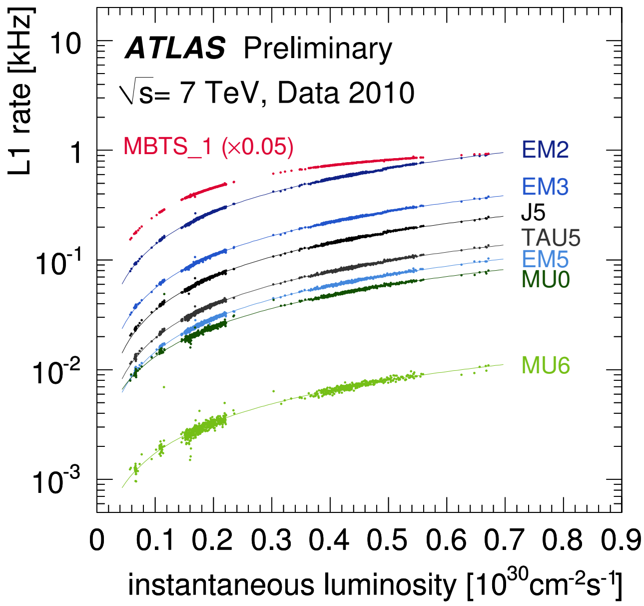

Figure 3.1: This ATLAS plot shows the unprescaled L1 trigger rates in June 2010 as a function of instantaneous luminosity. The plot is taken from [74].

3.3 Monte Carlo Simulations

Simulating events are a necessity of any particle physics experiment throughout all its stages. During development and construction of the experiments simulated samples are needed to evaluate the requirements on the hardware and are essential to validate the reconstruction software. At a later stage, during data taking, simulated events are crucial to compare the recorded data to expectations. This section briefly summarizes the individual steps in the generation of simulated samples for ATLAS, i.e. event generation, simulation, digitization and reconstruction. Figure 3.2 visualizes this production chain.

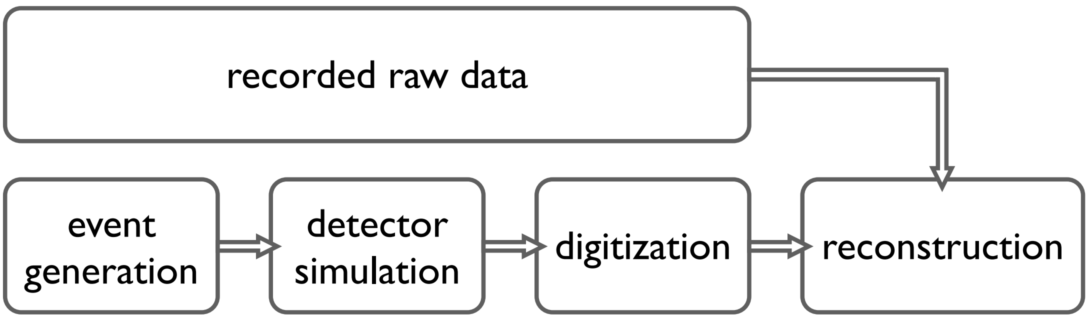

Figure 3.2: A schematic view on the production chain of simulated samples for ATLAS. Monte Carlo generated samples and data are processed by the same reconstruction.

3.3.1 Event Generation

The effective scattering in high energy proton-proton collisions takes place between the constituents of the protons. These quarks and gluons are referred to as *partons* and carry fractions of the corresponding proton momenta. The probability of finding a parton with a certain momentum fraction is described by the Parton Distribution Functions (PDF's). In the hard scattering process the initial partons interact and perform the physics processes under study, as for example the production of W-bosons, Higgs particles or the production of W^+W^--boson pairs.
Besides these hard scattering processes (HS) the so called underlying event (UE), describing interactions of remaining partons, contributes to the observed event. The parton-parton scattering cross-sections can be calculated using pertubative techniques. Monte Carlo (MC) event generators like Herwig [30, 31], Pythia [32] or Sherpa [33] use random numbers to generate these processes as well as the subsequent decay of the created particles. All particles carrying color charge can radiate off gluons. This process is called final state radiation (FSR). Likewise, partons may also radiate off gluons before the hard scattering, which is referred to as initial state radiation (ISR). The radiated off gluons will in turn radiate off more gluons or decay into quark-antiquark pairs. This process, referred to as *parton showering*, continues up to a certain energy scale, where the color connected partons are grouped into mesons and baryons. This stage in the event generation is hence called hadronization. As an example, Figure 3.3 visualizes a Higgs event associated with a $t\bar{t}$ quark pair generated by Sherpa.
Finally, the generated events with all its particles are stored as *Monte Carlo truth* and stay accessible also after the event passed the simulation, digitization and reconstruction steps. Monte Carlo truth information is essential to study and understand various physics processes and detector effects.

3.3.2 Detector Simulation

A complex and detailed description of the ATLAS detector is needed to accurately model the propagation of the generated final state particles through the detector. Interactions with the different detector materials are computed by the ATLAS simulation software G4ATLAS [34], which is based on a detailed model of the entire detector with all its subsystems. The algorithm is a customization for ATLAS of the widely-used Geant4 simulation software suite [35]. G4ATLAS propagates all generated final state particles in small steps to the modeled detector surfaces, evaluating and simulating the possible interactions with the local materials step by step. Also the decays of long-living particles such as e.g. K or ϕ mesons are included in the simulation.
Consequently, all energy deposits of the traversing particles are stored for each of the approximately 25 million volumes in G4ATLAS.

3.3.3 Digitization

The input of the digitization is the list of energy deposits as obtained from the detector simulation. To allow for detailed comparisons of recorded data and Monte Carlo samples,

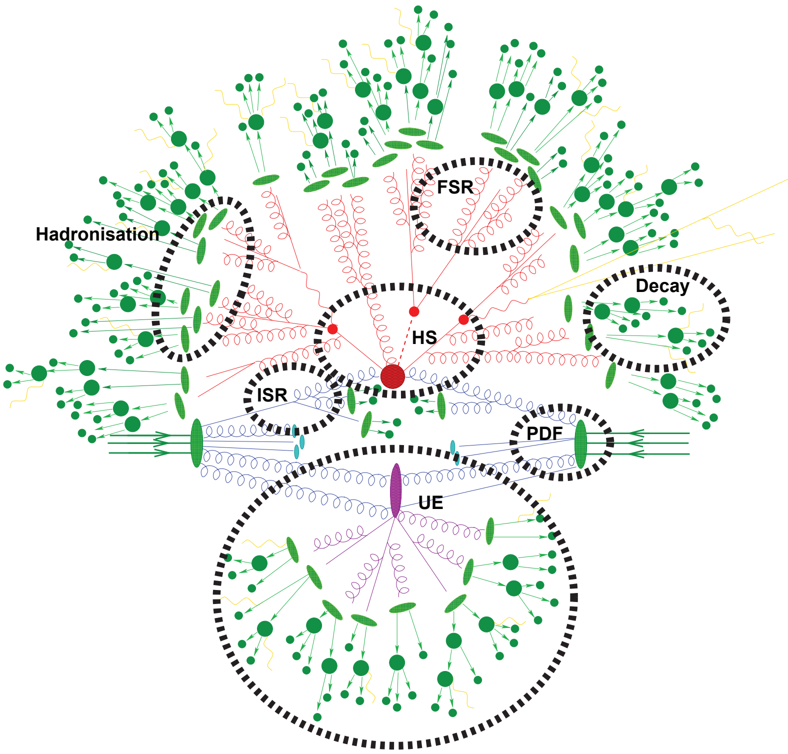

Figure 3.3: A visualization of a generated $t\bar{t}H$ event including initial and final state radiation, hadronization and decays. The HS blob contains the top and anti-top quarks shown as straight lines, as well as the subsequently hadronically decaying Higgs boson shown as a dashed line.

these energy deposits need to be converted into detector measurements, i.e. electronic signals of deposited charges and electrical currents. This is done by the digitization step, so the output can be treated like raw data, see Figure 3.2.

3.3.4 Reconstruction

After the digitization step, the Monte Carlo events are processed by the same reconstruction algorithms that are used for data. This coherent processing of data and simulated events is essential to study detector effects as well as physics processes. All physics objects are obtained during this stage, such as tracks, jets but also event variables like the missing transverse energy. Detector calibration and alignment are additional important ingredients for the reconstruction algorithms improving the resulting physics observables. At high luminosity there is a non-negligible probability for multiple protons to interact in a single bunch crossing and hence additional particles are created. These events are referred to as *pile-up* events. This effect is taken into account for increasing luminosity by adding additional minimum bias events to the Monte Carlo samples during the reconstruction.
A more detailed description of the reconstructed physics objects used in this thesis is

given subsequently. We hereby focus on the muon reconstruction and identification as the title of this thesis suggests.

3.4 Jets

Jets are features of the hadronic final-states of an event. They are the remnants of a high energetic parton that showered off partons and produced thus a collimated stream of particles. Since jets carry an integer electric charge and zero net color charge, no fully unambiguous mapping to partons in the event is possible. However, they can be a powerful measure of the QCD processes in the hard scattering of the event. After the hadronization, described in 3.3.1, hadrons and long living mesons created in QCD interactions traverse the Inner Detector before they get absorbed in the ATLAS calorimeters, creating energy deposits in cone shaped collections of clusters. Jets are designed to cluster and add up these energy deposits such that their properties like energy, momentum, etc. reflect as closely as possible the properties of the partons in the hard scattering in the center of the collisions. This way, properties of quarks, gluons but also hadronically decaying particles like W- and Z-bosons can be determined, although they are generally not physical observables.
Unlike electron or muon reconstruction, that aim to find the track and/or energy deposits of the corresponding particle traversing the detector, jet algorithms do not find pre-existing jets, but define them. Therefore, there are various different concepts of how to define a jet. An overview of the discussed jet algorithms for ATLAS is given in [54]. The default jet algorithm chosen for the collaboration is also used to define jets in Chapter 6. It is referred to as the Anti-k_{T} jet algorithm [29]. The characteristic feature of this algorithm is that in the vicinity $\Delta R < R$ of a hard, thus high transverse momentum calorimeter object all objects with low transverse momentum are merged with the hard object in the order of their closeness in ΔR. R is a parameter of the algorithm which sets the resolution of the algorithm. Figure 3.4 displays an impressive two jet event in ATLAS, recorded in the last days of the 2010 proton-proton run [75]. The transverse momentum of the highest energetic jet amounts to $p_{\mathrm{T}} = 1.3$ TeV. The total energy deposited in the transverse plane is $E_{\mathrm{T}} = 2.2$ TeV.

3.5 Missing Transverse Energy

The missing transverse energy, $E_{\mathrm{T}}^{\mathrm{miss}}$ is the vectorial sum of the energies measured by ATLAS in the transverse plane. Since the exact momentum along the beam-pipe of the constituents of the colliding hadrons in hadron colliders is not known but follows the parton distribution functions, the experiments can only use momentum and energy conservation in the transverse plane. An unbalance of energy in the transverse plane signals particles that escape the detector undetected, such as the weak interacting neutrinos. Due to large underlying event effects and possible pile-up events the uncertainty on $E_{\mathrm{T}}^{\mathrm{miss}}$ is large. Besides the energy deposits in the ATLAS calorimeters, also the muon momentum

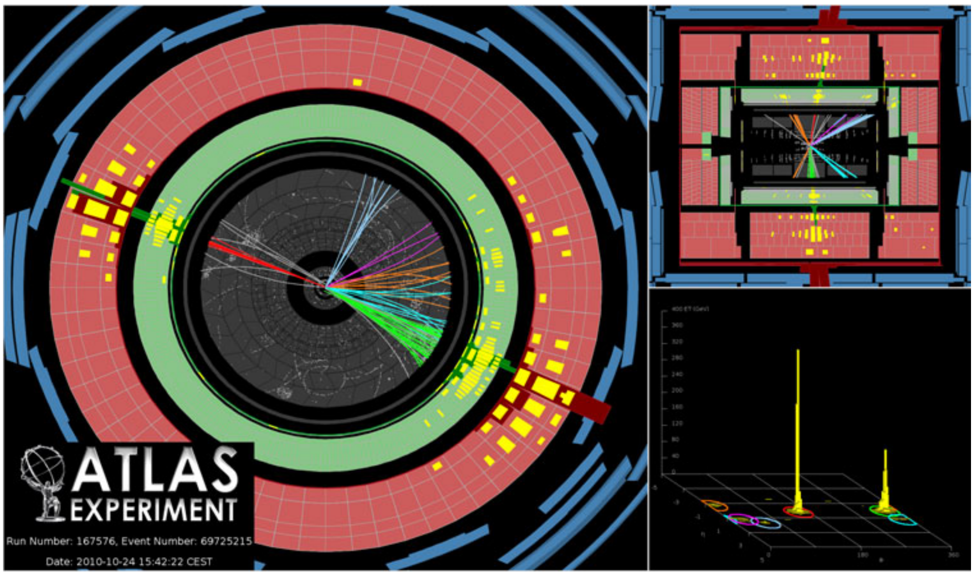

Figure 3.4: An event display of a two-jet event recorded by ATLAS in 2010.

measurement in the transverse plane is accounted for in the calculation of the $E_{\mathrm{T}}^{\mathrm{miss}}$.

3.5.1 Implementation

The missing transverse energy is composed of several contributions [1]. The energy deposits in electromagnetic and hadronic calorimeters are accounted for by summing over the calibrated topological clusters referred to as `MET_LocHadTopo` in the ATLAS community. The topological clustering covers the pseudorapidity range $|\eta| < 4.5$, leaving out the region $4.5 < |\eta| < 5$ as in this regions there are problems with the energy calibration in the FCAL. The clusters are seeded by calorimeter cell deposits above four standard deviations of the cell noise level. Neighboring cells with energy deposits exceeding two standard deviations are added to the cluster. Afterwards, all the neighboring cell deposits are added as well. The clusters are calibrated to correct for dead material in the detector as well as for out-of-cluster deposits, which correspond to energy deposits in calorimeter cells outside of the reconstructed clusters, i.e. in the tails of hadronic or electromagnetic showers which are rejected by noise cuts.
Muons usually traverse the detector without being absorbed in the calorimeters. The momentum they carry needs to be added to the $E_{\mathrm{T}}^{\mathrm{miss}}$ calculation. A muon term based on ID and MS track measurements of the reconstructed muons in each event is hence added to correct for the muon contributions. The individual x and y contributions are added to the total missing transverse energy, i.e.

$$E_{\mathrm{T}}^{\mathrm{miss}} = \sqrt{(E_{\mathrm{x}}^{\mathrm{miss}})^2 + (E_{\mathrm{y}}^{\mathrm{miss}})^2} \quad . \tag{3.1}$$

[1]We follow the recommendations of the ATLAS Jet-$E_{\mathrm{T}}^{\mathrm{miss}}$ group [82].

To reduce the sensitivity to mis-measured muons, we define a quantity called relative missing transverse energy which is defined as:

$$E^{\text{miss}}_{\text{T,rel.}} = \begin{cases} E^{\text{miss}}_{\text{T}} \sin(\Delta\phi) & \text{if } \Delta\phi \leq \pi/2 \\ E^{\text{miss}}_{\text{T}} & \text{if } \Delta\phi > \pi/2 \end{cases} \tag{3.2}$$

where $\Delta\phi$ denotes the angle between $E^{\text{miss}}_{\text{T}}$ and the closest muon in the transverse plane.

3.6 Muon Reconstruction and Identification

As discussed in the previous chapter an efficient muon reconstruction with a precise momentum measurement is essential to explore the physics potential at the LHC with ATLAS. The two tracking devices ID and MS as well as the thick calorimeter, shielding the MS provide the necessary means on the hardware side. Muons are particles that leave measurable signals in several detector subsystems of ATLAS. This is utilized by various algorithms reconstructing and identifying muons. Two comprehensive, independent software packages to reconstruct muon trajectories have been developed, which are also commonly referred to as the two muon algorithm families. They are called Muid [55] and Staco [38, 39] and comprise each a full muon reconstruction and identification chain of algorithms. While Staco is based on muon reconstruction code written in Fortran, called MuonBoy [37], Muid was specifically designed for Athena. Its core reconstruction algorithm, Moore [36] is written in C++ and takes full advantage of the modular Athena framework.
Both algorithm chains follow the same approach to reconstruct and identify muons:

1. A global search for patterns in the MDT hit distribution is performed.

2. The found patterns in the MS are fitted by straight lines to obtain segments.

3. Segments are combined to track candidates that are extrapolated to the interaction point. These MS tracks are called **standalone muons**.

4. ID tracks and MS tracks are combined to **combined muons**.

5. ID tracks are also combined with single, or multiple MS segments, without requiring a full MS track. These muons are called **segment tagged muons**.

An illustration of these steps is presented in Figure 3.5. We follow the given order in this chapter and discuss the individual implementations for the Muid family, for each step. Finally, in 3.6.5 we introduce an independent method to reconstruct muons, using calorimeter energy depositions, the **calorimeter tagged muons**.
The summary in 3.6.6 gives a compact overview of all available muon identification algorithms, including an attempt to visualize the different muon types.

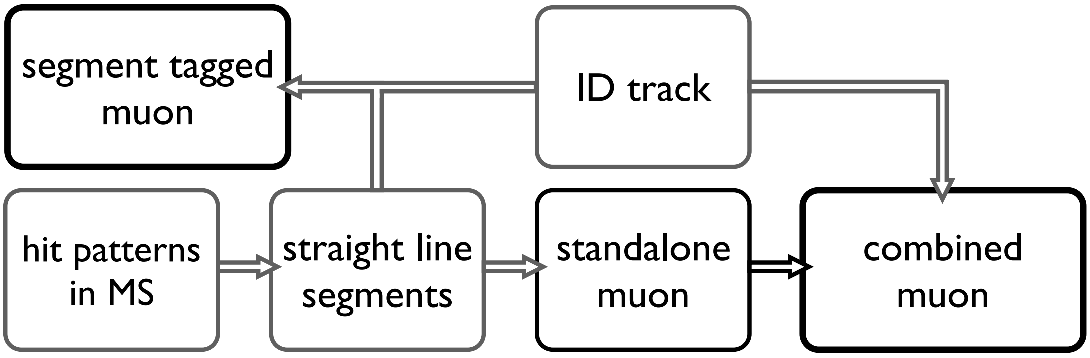

Figure 3.5: A schematic view on the standard muon reconstruction and identification in ATLAS, as performed by Muid and Staco.

3.6.1 Standalone Muons

Standalone muons are tracks reconstructed and identified by Moore for the Muid family and by Muonboy for the Staco family. They are purely based on the MS measurements. In the following, we discuss the making of standalone muons by the Moore algorithm. A more detailed description of Moore can be found in [59]. References [39] and [37] explain the corresponding standalone muon reconstruction with the Muonboy package for the Staco family.

Pattern Recognition

The search for patterns in the full MS volume is done using Hough transforms. This method to identify patterns and trajectories in a sample of point measurements was developed by Paul Hough in 1962 to analyze bubble chamber pictures at CERN. Mathematically, it is a transformation f_H transforming elements of $\mathbb{R}^n$ into the Hough space H.

$$f_H : \mathbb{R}^n \to H \tag{3.3}$$

To illustrate the general concept we choose $n = 2$. Any line can be parametrized in this 2-dimensional x-y-space as

$$x \sin\phi - y \cos\phi = \mathrm{R}_0 \tag{3.4}$$

with R_0 being the distance between the origin of the cartesian x-y-coordinate system and the closest point of the line. The angle ϕ is defined by R_0 and the positive x-axis.
However, for each point (x, y) Equation 3.4 describes also a curve in the polar R_0-ϕ-space. This space denotes the Hough space in our example. Drawing the Hough curves of different points on the line in the cartesian system unveils an intersection of all curves in one point of the Hough space. Figure 3.6 illustrates the concept for two independent lines and three random points in the x-y-space. All points in Figure 3.6(a) are transformed into their curves in the Hough space in (b). The two points in Figure 3.6(b) where all black and all grey curves meet indicate that they originate from the same lines in the x-y-space.

The three random points in Figure 3.6(a) that do not belong to a common line appear as dashed lines without a common intersection in the Hough space after their transformations. In summary, transforming points (x_i, y_i) in the Hough space and searching for curve intersections will identify points that belong to the same lines in the x-y-space.

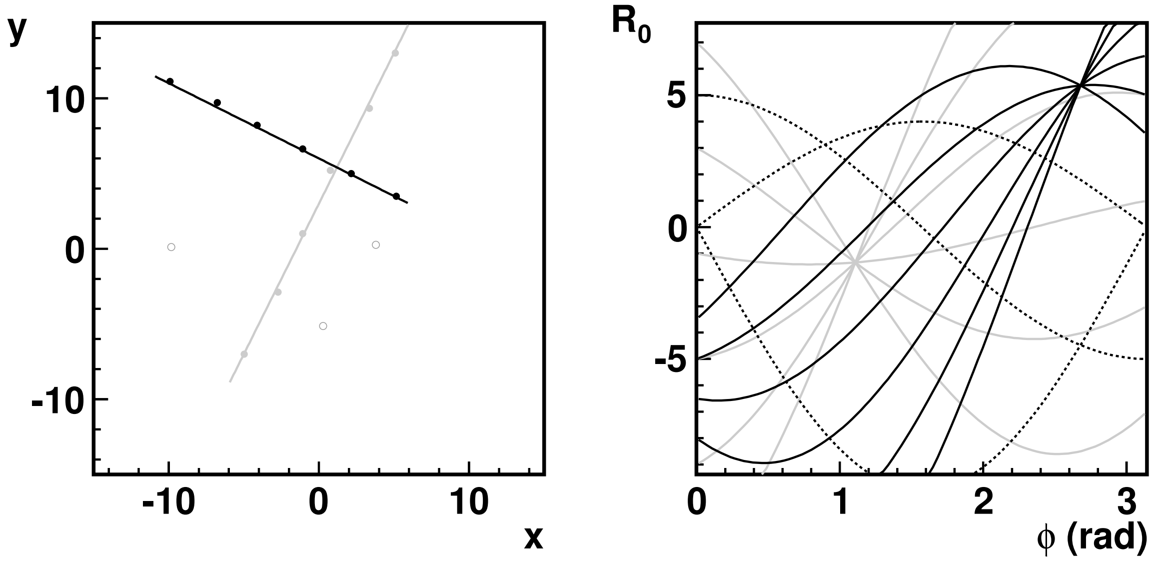

(a) cartesian coordiante system

(b) Hough space

Figure 3.6: Two sets of points belonging to two lines are shown in grey and black in the cartesian coordinate system in (a). Their transformation in the Hough space are shown in (b). The open circles represent random points that are transformed into dashed lines in the Hough space.

In practice, more complex, non linear Hough transformations are used to identify not only lines but all sorts of trajectories. The Hough space is binned into a Hough histogram, so the intersection points do not have to be computed individually but only the maxima in the Hough histogram need to be found. This method is considerably faster particularly for a large number of point measurements like in most ATLAS events. The Hough histogram for our example is shown in Figure 3.7. The chosen binning of the histogram is crucial since it is directly related to the patterns. A too small bin size will smear out clear peaks while a too large bin size will degrade the resolution, thus close patterns might not be distinguishable.
Hough transforms are in addition very convenient to use because the processing time of these transformations scales linearly with the number of point measurements k as opposed to most combinatorial approaches that scale with k^3.

The Hough transforms use measurements of all ATLAS MS subsystems (MDT, CSC, RPC, TGC) to identify patterns in the MS hit collection. The search is performed in two orthogonal planes, the x-y-plane (ϕ patterns) and the R-z-plane (η patterns) in which

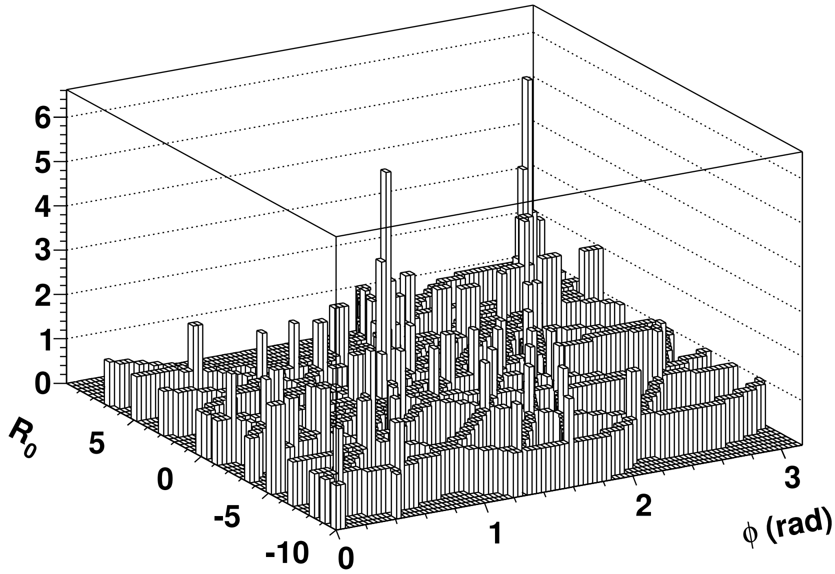

Figure 3.7: The binned Hough space is shown. The maxima in the histogram correspond to the searched patterns.

the toroidal field bends the muon trajectories. A straight line R-ϕ transformation is used to find ϕ patterns, while a more complex track model is needed for the curved tracks in the R-z-plane, see Figure 3.8. From the interaction point to the MS entrance, a straight line parametrizes the trajectories in the R-z-plane while in the toroidal field, a parabolic parametrization is used. Since the outer endcaps of the MS do not lie within the nominal toroidal field, a straight line transformation is used for this region and completes the transformation used to identify η patterns. More details on Hough transforms and the pattern recognition used to reconstruct muons in ATLAS can be found in [60].

Segment Making

Two segment making algorithms were developed, one for the MDT's one for the CSC's.

- **MDT segments**: The MDT hits from patterns found by the Hough transformations seed the MDT segment making. In each muon station with hits from a pattern the 4 possible tangents to the drift-radii of the two outer hits are constructed, see Figure 3.9 for an illustration. If at least one of these tangent lines is within 0.2 rad of the estimated pattern direction and at least three hits are found within 1.5 mm of that tangent, a straight line is fitted to all drift radii matching the latter requirement. If the χ^2 value divided by the number of degrees of freedom (χ^2/ndof) of the fit is larger than 10, the MDT hit with the largest contribution to the χ^2 is dropped and the fit is performed again. This step is repeated until the χ^2/ndof is smaller than 10. If the number of fitted hits drops below three, no segment is made. Finally the

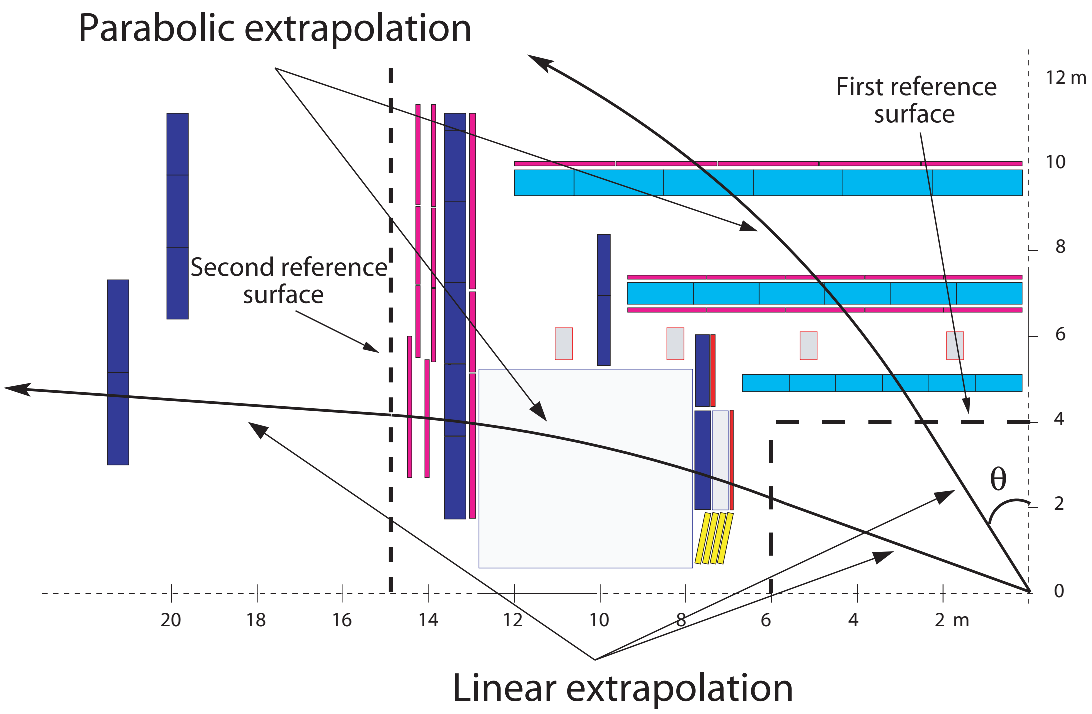

Figure 3.8: The model to parametrize muon trajectories in the R-z-plane is illustrated in a quadrant of the ATLAS MS.

fit parameters and their covariance are stored as a MDT segment. RPC or TGC trigger hits associated to the pattern are now associated to the segment.

The resulting MDT segment collection still contains possible ambiguities, that are segments sharing hits. These are solved by the following priority list:

1. largest number of hits on tracks
2. smallest sum of $N_\delta + N_{\text{out-of-time}} + N_{\text{holes}}$
3. largest number of trigger hits
4. smallest χ^2/ndof

To understand the second item decision, one needs to distinguish between different types of MDT hits. The four distinctive hit types are illustrated in Figure 3.10. For a hit-on-track, the track is a tangent on the drift circle, while for an out-of-time hit, it is a secant. A too small drift circle is often caused by free electrons, created in an ionizing interaction of the muon with the MDT tube walls, that move towards the central wire. These so called δ-electrons create an own drift radius, closer to the center of the tubes. N_δ stands hence for the number of hits that are associated to δ-electrons. Consequently, $N_{\text{out-of-time}}$ is the number of out-of-time hits and N_{holes} the number of holes, see Figure 3.10.

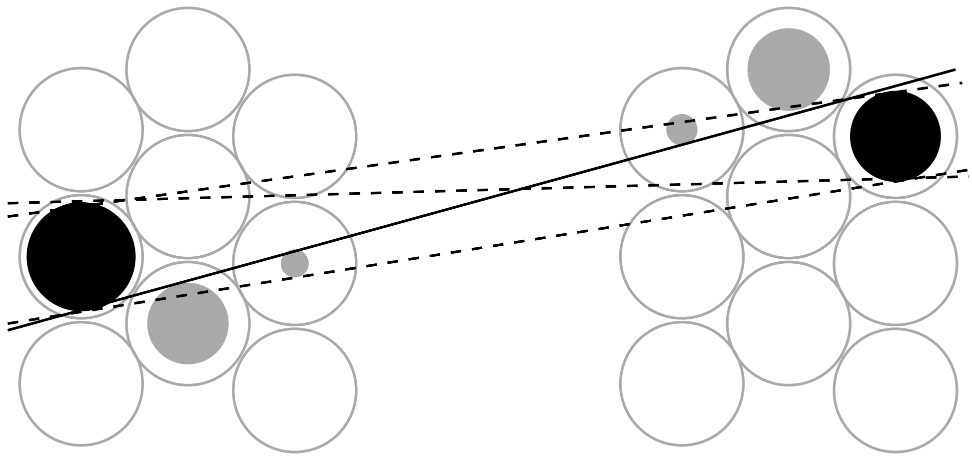

Figure 3.9: A schematic view on two MDT multilayers is shown. The tangent lines to the seeding drift circles (black) are drawn as dashed lines, while the one with the most associated hits in drawn as a solid line.

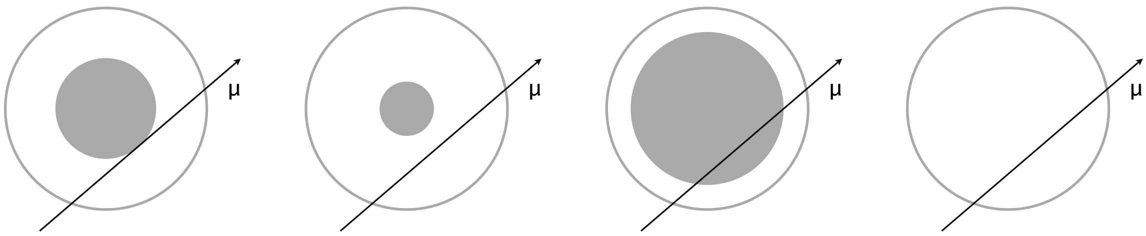

(a) hit-on-track (b) δ-electron (c) out-of-time (d) missing hit

Figure 3.10: The four distinctive MDT hit types are shown. A missing hit is also referred to as a *hole*.

- **CSC segments**: Fitting the charge depositions on the ϕ and η strips of the CSC's create clusters which are fitted to straight lines to make segments. These ϕ- and η-segments are then combined to the final CSC segments with a 3-dimensional position and direction.

Track Finding

In order to find the combination of segments that originates from the same muon, the MDT and CSC segment collections are combined and a segment matching is performed. A segment is labeled *compatible* with another if both were found in the same pattern and the two segments are successfully matched in position and direction. Sets of compatible segments are created, the track candidates. Tracks are built segment by segment outside-in from a track candidate. Thus, track fits are seeded by the track candidate segment(s) in the outermost station, normally the outer station. These segment(s) are fitted to the

segment(s) in the next station layer closer to the interaction point, normally the middle station. The resulting 2-segment tracks of successful fits are then fitted to the innermost station layer segment(s). This method allows for the creation of multiple tracks from a single segment seed. If tracks share more than half of their segments, they are merged. The resulting collection of tracks per pattern is first ranked according to their total number of associated hits and the smallest χ^2/ndof before their ambiguities are solved. If tracks share the same hits, these hits are assigned only to the higher ranked track. After the ambiguities are solved, the remaining tracks are refitted utilizing a detailed material and geometry description of the associated detector volume. All tracks that can not be successfully refitted are dropped. The resulting collection of tracks are the Moore tracks.
Subsequently, these tracks are extrapolated inwards to the beam pipe, taking material interactions and energy loss, particularly in the calorimeters into account. At the closest point to the IP, the so called perigee, the track parameters are determined and stored as standalone muons of the Muid collection.

3.6.2 Combined Muons

Prompt muons traverse the Inner Detector before they are measured in the muon system. It is hence reasonable to attempt to identify the ID track, that originates from the muon whose standalone track has already been reconstructed. Muid and Staco both calculate the χ^2_{match} of pairs of standalone and ID tracks to find possible matches.

$$\chi^2_{\mathrm{match}} = \left(\mathrm{t_{MS}} - \mathrm{t_{ID}}\right)^{\mathrm{T}} \left(\mathrm{cov_{MS}} + \mathrm{cov_{ID}}\right)^{-1} \left(\mathrm{t_{MS}} - \mathrm{t_{ID}}\right) \tag{3.5}$$

where t symbolizes the track parameters and cov the corresponding covariance matrix [40]. If an ID track passes the χ^2_{match} requirement, it is extrapolated to the MS and position and direction of the extrapolated track are compared to the corresponding MS track, the Moore or Muonboy track. If these matching requirements are also fulfilled, the combined track parameters of the Staco Combined muon are obtained from a statistical combination of ID and MS track, which is defined as:

$$\mathrm{t_{Staco}} = \left(\mathrm{cov_{ID}^{-1}} + \mathrm{cov_{MS}^{-1}}\right)^{-1} \left(\mathrm{cov_{ID}^{-1}}\,\mathrm{t_{ID}} + \mathrm{cov_{MS}^{-1}}\,\mathrm{t_{MS}}\right) \tag{3.6}$$

Muid Combined follows a different approach and obtains its combined track parameters by fitting the ID and MS measurements of the two tracks.

3.6.3 Segment Tagged Muons

As discussed in 2.3.4, the Muon Spectrometer has some acceptance holes at $\eta = 0$ and in the ATLAS feet region. But the standalone muon reconstruction is also more challenging in the overlap region between barrel and endcaps at $|\eta| \approx 1.2$, where less measurements are available due to missing third MDT stations. In addition, low momentum muons can produce hits and segments in the MS that are not found by the standalone algorithm, due to the large curvature of these muons.
In order to recuperate these efficiency losses, ID tracks are extrapolated to the muon

system and matched to segments. The track parameters of the segment tagged muons are taken from the ID track that was successfully matched to one or multiple MS segments. MuTagIMO is the segment tagger of the Muid family and extrapolates ID tracks to all three muon stations, hence, the 'I'nner, 'M'iddle and 'O'uter stations. At every station, a matching to segments in the vicinity of the extrapolated track is made. A detailed description of the algorithm and its performance is given in Chapter 4.
MuTag is the corresponding segment tagger of the Staco family and uses hence Muonboy segments for the matching. Unlike MuTagIMO, it is not an independent identification algorithm, but it only uses ID tracks and MS segments, that are not already part of a Staco Combined muon. Another important difference to MuTagIMO is that it extrapolates in general only to the inner station. For $|\eta| < 1.4$ also the middle stations are included and at $\eta \approx 0$ the outer station are added to reduce the inefficiencies resulting from the $\eta = 0$ acceptance hole. The current configuration of MuTag is specified at [78].

3.6.4 MuGirl Muons

The MuGirl algorithm follows the approach of the segment taggers by extrapolating ID tracks to the MS inner, middle and outer stations [79]. However, instead of matching the extrapolated tracks to either Moore or Muonboy segments in the MS, a local pattern recognition in the vicinity of the extrapolated tracks is performed to create the MuGirl segments. This is done station by station from the inner to the outer. The created segments in each station are used to refine the extrapolated track parameters for the next station. An artificial neural network decides if an extrapolated ID track with its set of MuGirl segments is rejected, or tagged, therewith identified as a MuGirl muon. After an ID track is successfully tagged, a refit of associated ID and MS measurements is performed by MuGirl and a muon with the combined track parameters is created, if the fit is successful. These muons are commonly labeled *refitted MuGirl muons*. The MuGirl and MuGirl refitted muons are added to the Muid family.

3.6.5 Calorimeter Tagged Muons

The calorimeter taggers are the only muon identification algorithms that are completely independent of the Muon Spectrometer. This interesting feature will be exploited in Chapter 5. Being independent of the MS also allows one to reconstruct muons in the regions where the MS coverage is limited, like at $\eta = 0$. Another use case of calorimeter tagged muons is to enhance the purity of combined or segment tagged muons to be confirmed by the calorimeter taggers. However, the comparatively low efficient calorimeter taggers will decrease the efficiency of such a selection significantly as will be shown in Chapter 5.
Calorimeter tagged muons, also abbreviated to *calo muons* are stored in an independent collection called CaloTrkMuId [80]. Two algorithms are used to identify calo muons, *CaloMuonTag* [61] and *CaloLikelihood ratio*. Both algorithm are seeded with Inner Detector tracks, that are extrapolated to and through the calorimeters. The energy deposits in the electromagnetic and hadronic calorimeters are collected along the extrapolated track. Muons with sufficient momentum to traverse the calorimeter are expected to leave

small, continuous energy deposits with a total of approximately 3 GeV. This makes it distinguishable from an electron whose energy will be deposited mostly entirely in the EM calorimeter layers. Low energetic hadrons will deposit most of their energy in the first layer of the hadronic calorimeters, while high energetic hadrons will deposit large amounts of energy in the central hadronic calorimeter layer. These characteristics are used by CaloMuonTag to veto energy deposits from electrons and hadrons.
The large number of ID tracks in collision events requires a preselection. The extrapolated ID tracks are preselected by requiring a transverse momentum of at least 2 GeV, at least 2 Pixel and 6 SCT hits on the track and an isolation of $\log_{10}(p_{\mathrm{T}}^{iso}/p_{\mathrm{T}}) < 0.7$, where p_{T} denotes the transverse momentum of the selected track and p_{T}^{iso} is the sum of the transverse momenta of all ID tracks in a cone with an angle of 0.45 rad around the selected track. The same cone is used to tighten the isolation by requiring the sum of the energy deposits in the cone along the extrapolated track to be smaller than 15 GeV for $|\eta| < 1.5$, 8 GeV for $1.5 < |\eta| < 1.8$ and 12 GeV for $|\eta| > 1.8$. These isolation requirement on energy deposits and ID tracks are needed to reject hadrons mimicking muon signals in the calorimeter by showing a very broad showering profile with small energy deposits in the individual calorimeter cells.
Instead of relying on a cut-based selection, the CaloLikelihood ratio algorithm calculates the probability of a muon to induce the measured energy deposits along the extrapolated ID track. The likelihood ratio L is computed with

$$L(m_1, m_2, \ldots, m_N) = \frac{\prod_{i=1}^{N} P_i^{\mu}(m_i)}{\prod_{i=1}^{N}\left[P_i^{\mu}(m_i)\right] + \prod_{i=1}^{N}\left[P_i^{\mathrm{bkg}}(m_i)\right]} \tag{3.7}$$

where N denotes the number of calorimeter cell measurements associated to the extrapolated ID track and m_i indicates the measurement in calorimeter cell i. $P_i^{\mu}(m_i)$ is hence the probability of a muon to create the measured energy deposit and $P_i^{\mathrm{bkg}}(m_i)$ corresponds to the probability of non-muons to create the same energy deposit. The probabilities are a function of η and p_{T} and cached by the algorithm. With $L \in [0, 1]$, where 0 indicates that the found energy deposits along the extrapolated ID track are very unlikely to originated from a muon, while 1 indicates the opposite. The CaloLikelihood ratio algorithm requires $L > 0.5$ to identify a calo muon and store the ID track parameters.

3.6.6 Summary

Various techniques are used in ATLAS to reconstruct and identify muons. Calorimeter tagged muons cover the entire range up to $|\eta| = 2.5$ while combined muon algorithm provide a highly efficient muon identification with the best momentum resolution, taking full advantage of both ATLAS tracking detectors. Their inefficiencies, particularly at low muon momenta can be recuperated using segment tagged muons. A conceptual overview of the available muon types and the sub-detector systems used for their reconstruction and identification is shown in Figure 3.11. In addition to these different reconstruction and identification techniques, facilitated by the ATLAS design, two different algorithm families have been developed. Table 3.1 lists the available muon algorithms sorted by their belonging families and types.

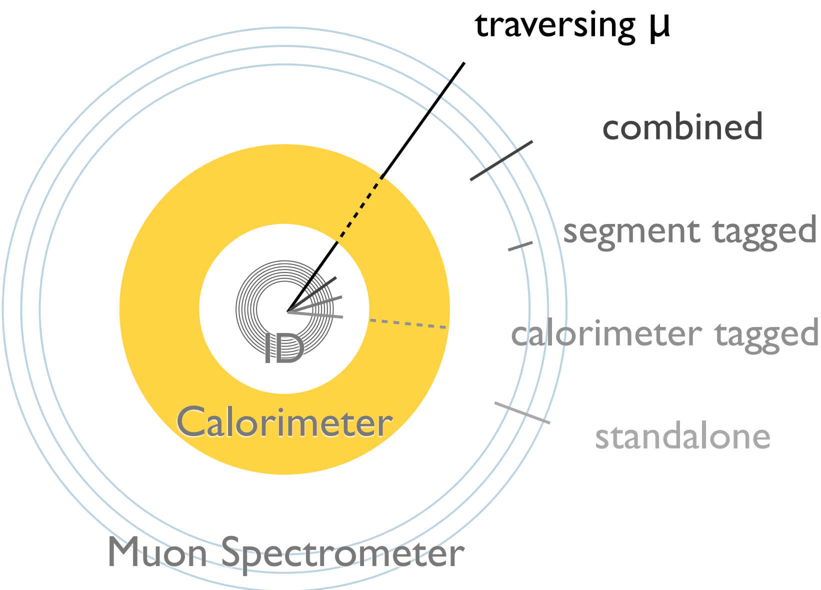

Figure 3.11: In a simplified cross section of the ATLAS barrel the characteristics of the different types of muons and their signals in the detector are depicted.

Muon Type	Muid	Staco	Calo
Standalone	Moore	Muonboy	–
Combined	Muid Combined MuGirl refitted	Staco Combined	–
Tagged	MuTagIMO MuGirl	MuTag	CaloMuonTag CaloLikelihood ratio

Table 3.1: A schematic overview of the different types of muons and their implementations is given. The taggers of the Muid and Staco families use MS segments, while the calorimeter taggers use the calorimeter cell energy depositions.

CHAPTER 4

Commissioning of a Muon Segment Tagger

This chapter explains in detail how the muon segment tagger algorithm MuTagIMO works on an event-by-event basis and what developments have been made to enhance its performance after commissioning the algorithm with first data. A detailed description of MuTagIMO can be found in [62].
In the following, two version of the MuTagIMO algorithm are compared: the one which was used to initially reconstruct the very first ATLAS data (Athena release 15) and the revised version, which has been commissioned on data (Athena release 16) [1].

4.1 Preface

When the LHC started running in March 2010 the performance of the ATLAS Detector had only been studied using cosmic muons. Though these studies were very useful and lead to improved detector alignment and calibration, the general performance on proton-proton collisions was unclear. As a consequence, MuTagIMO was run with very loose requirements in Athena release 15, which will be detailed in the following section, to allow for thorough studies and commissioning of the algorithm on first data. After it was clear that the mis-tag rate, the rate of MuTagIMO muons where ID track and associated muon segment(s) result from different particles, could be reduced significantly without decreasing the high efficiency, the requirements in MuTagIMO for Athena release 16 were tightened to get the best performance for physics analyses. Hereby, we granted high priority to the efficiency in order to not loose muons that would be valuable either for physics studies or further detector commissioning.

[1] This corresponds more precisely to the comparison of the software packages MuonSegmentTaggerTools-00-01-13 and MuonSegmentTaggerTools-00-01-33.

4.2 The Algorithm

This section describes the MuTagIMO algorithm in multiple steps from ID track and segment preselections over the extrapolation of the selected ID tracks to the segment matching and ambiguity solving. The developments made after commissioning the algorithm with first data are explained in each step. For a general introduction to muon segment taggers and MuTagIMO, the reader is referred back to 3.6.3.

4.2.1 ID Track Selection

The vast majority of Inner Detector tracks do not originate from muons. Additionally, muons with a momentum less than about 3 GeV will not be able to reach the Muon Spectrometer. It is hence sensible to apply quality and momentum cuts on the ID tracks. This reduces the mis-tag rate and limits the processing time of the algorithm. Table 4.1 shows the requirements on ID tracks for MuTagIMO in Athena release 15 and 16. The requirements on individual sub-detector hits of the ID track are found to be essential and were consequence implemented in release 15 very soon after the first muon events were analyzed. All Figures in this chapter include this basic requirement. Tighter cuts on the muon momentum and transverse momentum reduce the mis-tag rate significantly however at the cost of an efficiency loss in the low momentum region. Since these cuts can be applied at the analysis level, it is left to the physics user to reject these low momentum muons.

MuTagIMO in	p [GeV]	p_{T} [GeV]	Pixel hits	SCT hits
release 15	2	-	-	-
release 16	3	2	≥ 1	≥ 3

Table 4.1: The ID track selection requirements for the two compared versions of MuTagIMO are given.

4.2.2 Segment Selection

No additional requirements [2] on the selected segments were made in release 15. However, adding some basic requirements on the segment quality reduce the mis-tag rate as well as the CPU time consumption of the algorithm without compromising the efficiency. These basic requirements on the segments introduced in release 16 are the following:

- reject MDT segments with less than 3 hits.
- reject MDT segments that do not pass the following quality requirement on the hits: At least half of all MDT tube hits need to pass a certain value of integrated charge. The integrated charge is calculated by the MDT front-end electronics over

[2] See 3.6.1 for general requirements on segments.

a predefined time after passing the threshold and is referred to as ADC count. This requirement provides a good noise reduction [59].

- reject MDT segments with more than one enclosed hole and no trigger hits. A hole is an expected hit that was not found.
- reject MDT segments that are not close to chamber edges which have more holes than hits and no trigger hits. A segment is defined to be close to a chamber edge if its distance in the shortest tube to the edge of the corresponding chamber is less than 10 cm.
- reject MDT segments in the middle end-caps that have no trigger hits, although they are expected to have trigger hits.
- reject CSC segments that do not have η and ϕ hits.
- reject CSC segments where the sum of η and ϕ hits is less than 4.

4.2.3 Extrapolation

The selected ID tracks are extrapolated to the MS, using common tracking tools [42]. Since the extrapolation is a CPU time consuming procedure, the number of extrapolations per track are limited by first extrapolating each ID track to the MS entrance and then further to abstract surfaces that follow the ATLAS MS design, 3 cylinders and 2 times 4 disks, see 2.3.4. A loose match is performed between the extrapolated track at the surfaces it crosses and the segments that are associated to that surface. Large safety factors are added to the errors of the extrapolated track to insure no muon candidates are lost at this stage. The loose matching requirements depend on the individual surfaces and are given in more detail in [62]. The track is then only extrapolated to segments passing the loose matching criteria.

4.2.4 Matching

The matching is performed using position, direction, distance, as well as additional pull distributions of extrapolated track and segment. The segment surface is described in a local coordinate system, depicted in Figure 4.1. The individual matching quantities are listed here, while their mathematical definitions are given in Appendix A. $\mathcal{R}$ stands for a residual, $\mathcal{P}$ indicates a pull distribution. A single letter index refers to one of the local coordinates while two letters refer to the angle defined by the two corresponding local coordinates. The only exception is $\mathcal{P}_{\mathrm{CY}}$ where the C stands for a combination of position and direction. We can distinguish between different types of matching variables:

- established matching quantities:
  - in the **precision plane** $\mathcal{R}_{\mathrm{Y}}$, $\mathcal{P}_{\mathrm{Y}}$, $\mathcal{R}_{\mathrm{YZ}}$, $\mathcal{P}_{\mathrm{YZ}}$ are used.

  - in the **non-precision plane**, i.e. only for segments with ϕ coordinate measurement the matching is extended by cutting on $\mathcal{R}_{\mathrm{X}}$, $\mathcal{P}_{\mathrm{X}}$, $\mathcal{R}_{\mathrm{XZ}}$ in addition.

- additional quantities being the result of commissioning the algorithm with first data:
  - $\mathcal{R}_{\mathrm{chamber}}$: This quantity indicates wether or not the extrapolated ID track traversed the MDT chamber(s) with the associated segment. The values correspond to the distance between extrapolated track and the corresponding chamber edges. Negative values are returned for extrapolated tracks that cross the chamber, while positive values are returned for tracks that miss the chamber.
  - $\mathcal{P}_{\mathrm{chamber}}$: This is the pull distribution of $\mathcal{R}_{\mathrm{chamber}}$.
  - $\mathcal{P}_{\mathrm{CY}}$: This pull relates position and direction and was introduced as an additional powerful discriminant to reduce the mis-tag rate.

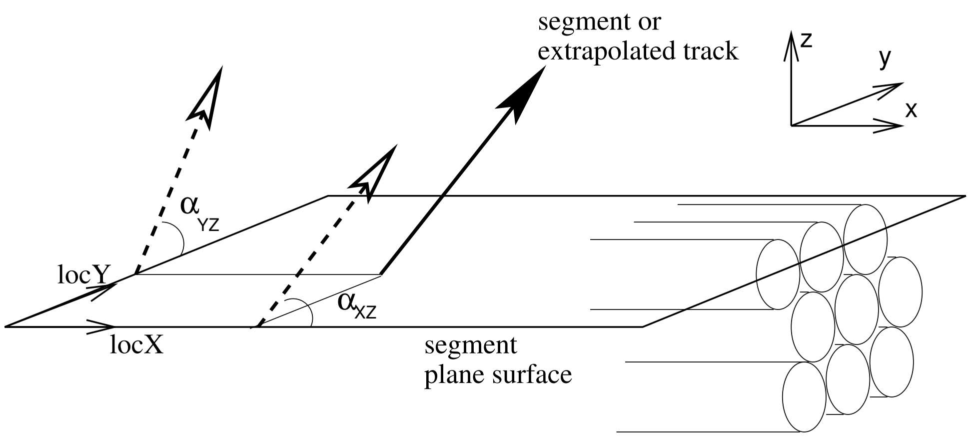

Figure 4.1: The local coordinate system for MS segment surfaces is shown.

The requirement on these matching quantities in Athena release 15 and 16 are shown in Table 4.2. The values of pull distributions, i.e. $\mathcal{P}_{\mathrm{Y}}$, $\mathcal{P}_{\mathrm{YZ}}$, $\mathcal{P}_{\mathrm{CY}}$ and $\mathcal{P}_{\mathrm{chamber}}$ correspond to standard deviations. The requirements on $\mathcal{P}_{\mathrm{Y}}$ and $\mathcal{P}_{\mathrm{YZ}}$ demand the sum of Pixel Detector and SCT hits of the corresponding ID track to be at least 5. The individual pull distributions in the precision plane are shown in Figure 4.3, while the variables $\mathcal{R}_{\mathrm{chamber}}$ and $\mathcal{P}_{\mathrm{chamber}}$ are shown in Figure 4.4. Like for the Pixel Detector and SCT hits requirement on the ID track, the cut on $\mathcal{R}_{\mathrm{chamber}}$ was implemented soon after studying the first muon events and hence all available data and simulated events include this requirement. The underlying distributions of the local residuals did not have to be modified and are shown in Figure 4.2. The requirement on the residuals in the non-precision plane, i.e. $\mathcal{R}_{\mathrm{X}}$ and $\mathcal{R}_{\mathrm{XZ}}$ hold only for segments with ϕ measurement, i.e. segments in the middle or outer stations of the detector barrel or the inner and middle stations of the end-caps, see 2.3.4. All these figures compare early data triggered on muons, corresponding to the first 16.9 nb^{-1} of integrated luminosity and Monte Carlo generated inclusive minimum bias, minimum bias muons and $Z \to \mu^+\mu^-$ events reconstructed in Athena release 15

[3]. The minimum bias muon sample is derived from the inclusive minimum bias sample by neglecting all MuTagIMO muons that do not originate from a generated muon at the vertex. The distributions of the Monte Carlo sets are normalized to data. As expected, the distributions from selected datasets are closer to the ones from minimum bias events but always lie in between the distributions of minimum bias and Z Monte Carlo.

	matching quantities	release 15	release 16
precision plane	$\|\mathcal{P}_{\mathrm{Y}}\| <$	30	5
	$\|\mathcal{P}_{\mathrm{YZ}}\| <$	30	5
	$\|\mathcal{P}_{\mathrm{CY}}\| <$	-	5
	$\|\mathcal{R}_{\mathrm{Y}}\| <$	2 m	2 m
	$\|\mathcal{R}_{\mathrm{YZ}}\| <$	0.7 rad	0.7 rad
non-precision plane	$\|\mathcal{R}_{\mathrm{X}}\| <$	2 m	2 m
	$\|\mathcal{R}_{\mathrm{XZ}}\| <$	0.7 rad	0.7 rad
additional requirements	$\mathcal{P}_{\mathrm{chamber}} <$	-	5
	$\mathcal{R}_{\mathrm{chamber}} <$	-	2 m

Table 4.2: The individual requirements on all matching quantities are shown before and after the algorithm commissioning. The values of pull distributions are in standard deviations.

4.2.5 Solving Ambiguities

Particularly in busy collision events, extrapolated ID tracks can often be matched to multiple segments in a single MS station. A muon however crosses an MDT station only once and therefore it can only be correctly associated to a single segment in one MS station. On the other hand, segments can also be matched successfully to multiple ID tracks in certain cases. These ambiguities are solved by a number of checks and selections:
In cases where one ID track has multiple associated segments in the same MS station, the one with the smallest $\mathcal{R}_{\mathrm{Y}}$ is taken. For multiple ID tracks sharing the same segments, selecting the right association is more complicated. In addition to comparing station and chamber names, a hit comparison of the segments is added in Athena release 16. Only if there is at least one chamber hit shared in two segments, the segments are taken to originate from the same muon. To select the ID track that most likely corresponds to that muon, a quality factor based on $\mathcal{R}_{\mathrm{Y}}$, $\mathcal{R}_{\mathrm{YZ}}$ and the number of segments that were associated to the ID track is calculated.
In order to reduce the mis-tag rate, a few additional modifications are implemented subsequently. All ID tracks tagged with a single segment coming from a CSC chamber are rejected. Since there are no acceptance holes in the CSC region, a good muon is expected to create more segments when traversing this detector region. ID tracks with only one associated MDT segment that has more than three holes are rejected as well. The requirement is tightened for events with high segment multiplicities. Less than 3 / 2 holes

[3]The corresponding ATLAS Monte Carlo samples names are given in Appendix E.1.

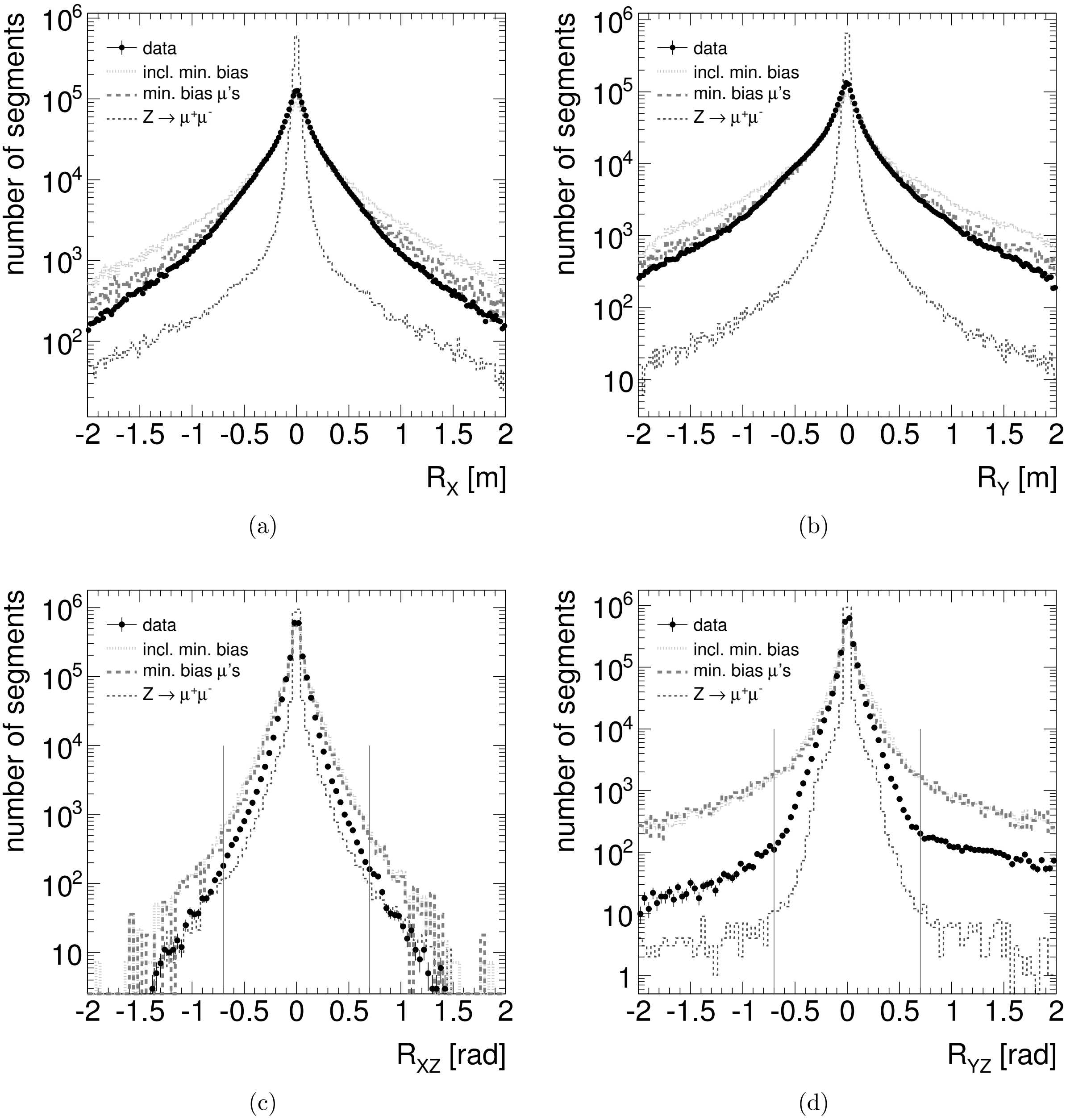

Figure 4.2: The residuals of position and direction in the local coordinate system are shown for data and Monte Carlo simulated minimum bias, as well as Z events.

are required in case of more than 30 / 50 segments per event. MDT segments made from a single multilayer (see 2.3.4) are rejected a) if they have one or more holes, or b) as a function of the segment multiplicity and the ID track p_{T}. For further details, the reader is referred to [62].

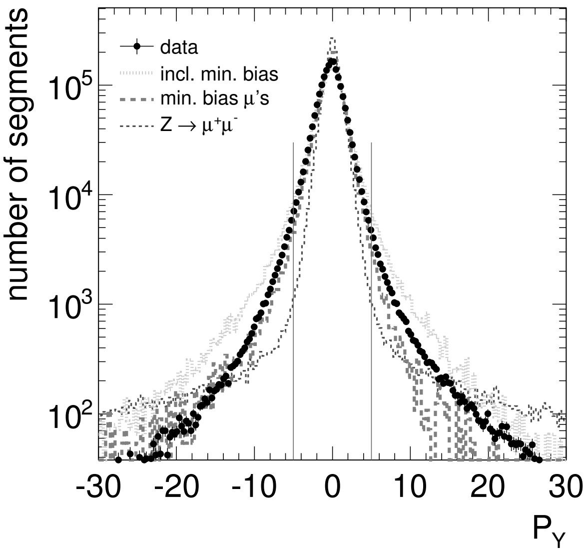

(a)

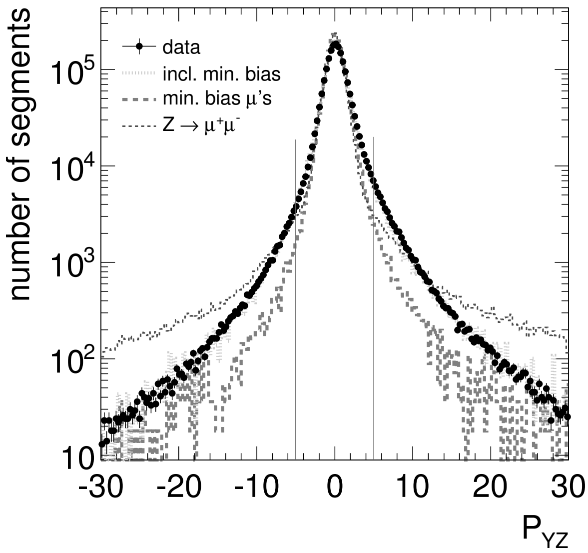

(b)

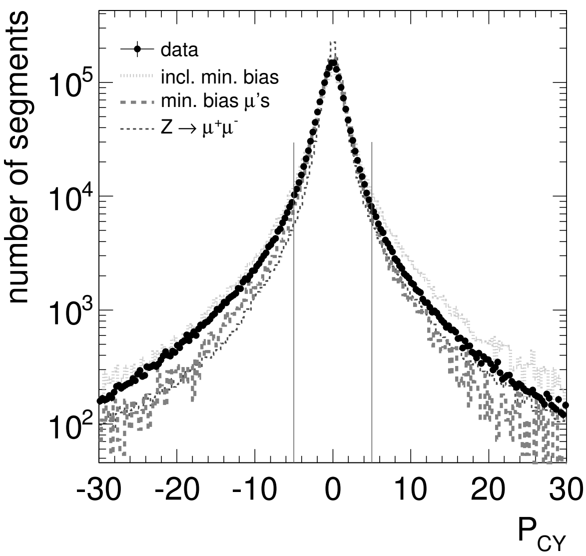

(c)

Figure 4.3: The pull distributions of position, direction and their correlation in the local coordinate system are shown for data and Monte Carlo simulated minimum bias, as well as Z events.

4.3 Performance

This section discusses the performance of the latest version of MuTagIMO. The improvements over the algorithm performance in Athena release 15 are shown on Monte Carlo simulated events in 4.3.1 and using data in 4.3.2.

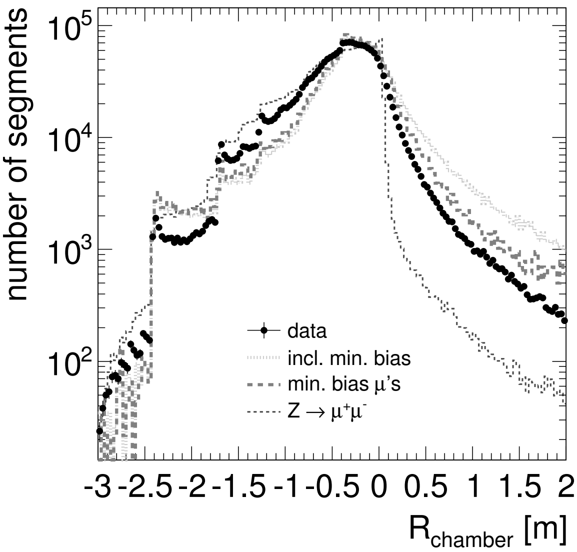

(a)

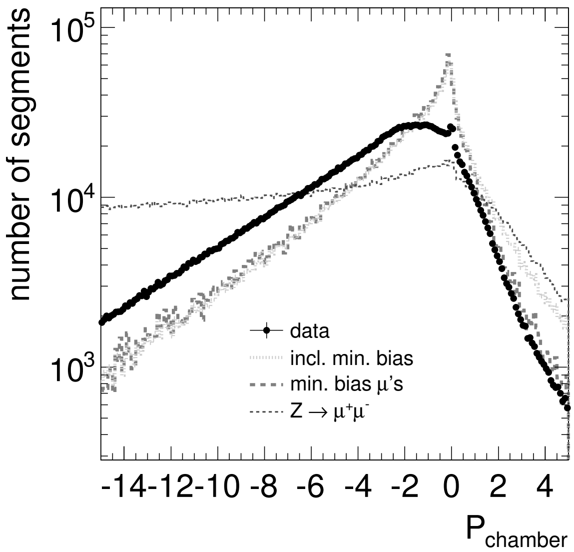

(b)

Figure 4.4: $\mathcal{R}_{\text{chamber}}$ and $\mathcal{P}_{\text{chamber}}$ are shown for data and Monte Carlo simulated minimum bias, as well as Z events.

4.3.1 On Simulation

Monte Carlo samples allow us to unambiguously evaluate the mis-tag or fake rate, using the available information from the event generator, see 3.3.1. We use a set of simulated $J/\psi \to \mu^+\mu^-$, $Z \to \mu^+\mu^-$ and leptonic $t\bar{t}$ samples to measure the performance in different physics environments. We define a fake in the following as a tagged muon whose ID track does not originate from a generated muon at the production vertex.
The Monte Carlo datasets processed with Athena release 16 have additional pile-up events included, see 3.3.4, while this is not the case for the release 15 samples. Pile-up events consist mainly of hadronic processes leading to an increased number of pions and kaons in the events which make the major part of the fakes. To obtain comparable samples the pile-up events are removed using Monte Carlo truth information. Figure 4.5 shows the obtained fake rates, the fraction of fake MuTagIMO muons in release 15 and 16 over the total number of ID tracks in release 16, for J/ψ, Z and the $t\bar{t}$ sample [4]. At low momenta, the errors on the extrapolated track get very large, leading to small values of the matching pull distributions. In addition, the number of ID tracks increases exponentially to lower momenta. Consequently, the fake rate rises towards low momenta. This is an unavoidable characteristic of all segment taggers. However, the tightened matching requirements in release 16 appear in a clear reduction of the overall fake rate. Particularly in busy events like in the $t\bar{t}$ sample the fake rate is reduced significantly, see Figures 4.5(e) and 4.5(f). But also cleaner events, like in the Z sample benefit from a reduced fake rate in release

[4]The corresponding ATLAS Monte Carlo sample names are given in Appendix E.1.

16 over the entire η range as shown in Figure 4.5(d).
Another meaningful quantity to study the MuTagIMO performance is the purity. It is defined as

$$p := 1 - \frac{N^{\text{fake}}_{\text{MuTagIMO}}}{N^{\text{all}}_{\text{MuTagIMO}}} \tag{4.1}$$

thus the fraction of MuTagIMO fakes to all MuTagIMO muons. Figure 4.6 shows the MuTagIMO purity for the selected three Monte Carlo samples, comparing again release 15 with release 16. Figure 4.6(a) shows that the increasing purity loss for muon momenta larger than 5 GeV observed in the J/ψ Monte Carlo sample in release 15 is recuperated in release 16. Also the Z and $t\bar{t}$ samples profit from a higher purity, particularly for low and intermediate muon momenta up to 30 GeV, as shown in Figures 4.6(c) and 4.6(e). While there are improvements in the barrel region the largest gain in purity is achieved in the end-caps as the right column of Figure 4.6 confirms.
Figure 4.7 shows the muon identification efficiencies of MuTagIMO in the corresponding samples. The efficiency is defined as:

$$\epsilon_{\text{true}} := \frac{N_{\text{MuTagIMO}}}{N_{\text{true muons}}} \tag{4.2}$$

where $N_{\text{true muons}}$ is the number of generated muons that fall within the acceptance of MuTagIMO, hence fulfilling $|\eta| < 2.5$ as well as the individual ID track requirements discussed in 4.2.1. In addition, the generated muons are required to originate from a J/ψ or Z decay depending on the sample. No requirements on the origin of the generated muon in the $t\bar{t}$ sample is made. N_{MuTagIMO} is the number of the selected generated muons that are found by MuTagIMO. A small efficiency drop of less than 2 % is observed for the plateau region of the algorithm, comparing release 15 to release 16. The losses are mainly in the forward region $|\eta| > 2$, as shown in Figures 4.7(b), 4.7(d), 4.7(f).

4.3.2 On Data

A dataset with an integrated luminosity of 1.9 pb^{-1}, recorded by ATLAS between April and August 2010 is used to show some key figures of the algorithm performance. The dataset has been independently reconstructed in Athena release 15 and 16, allowing us to compare the two versions of MuTagIMO in these releases. We only select events in which a muon trigger fired. Figure 4.8 shows the transverse momentum spectrum of MuTagIMO muons. The two peaks in the p_{T} distribution at 4 and 6 GeV originate from the trigger thresholds of the individual data periods. The requirement on the transverse momentum of the Inner Detector track $p_T > 2$ GeV, stated in 4.2.1 becomes visible. From $p_{\text{T}} > 10$ GeV onwards, we see a deviation in the shape of the tails, with the steeper fall-off being observed in release 16. The subsequently discussed data plots on the mis-tag rates will elaborate this discrepancy. The η and ϕ distributions are shown in Figure 4.9. The two dips in the ϕ distribution at $\phi \approx -1$ rad and $\phi \approx -2$ rad result from trigger inefficiencies in the ATLAS feet region. The plots show that the fraction of muons that is rejected due to the tightened matching criteria is approximately constant over the entire detector volume. The number of segments associated with a tagged ID track is shown in

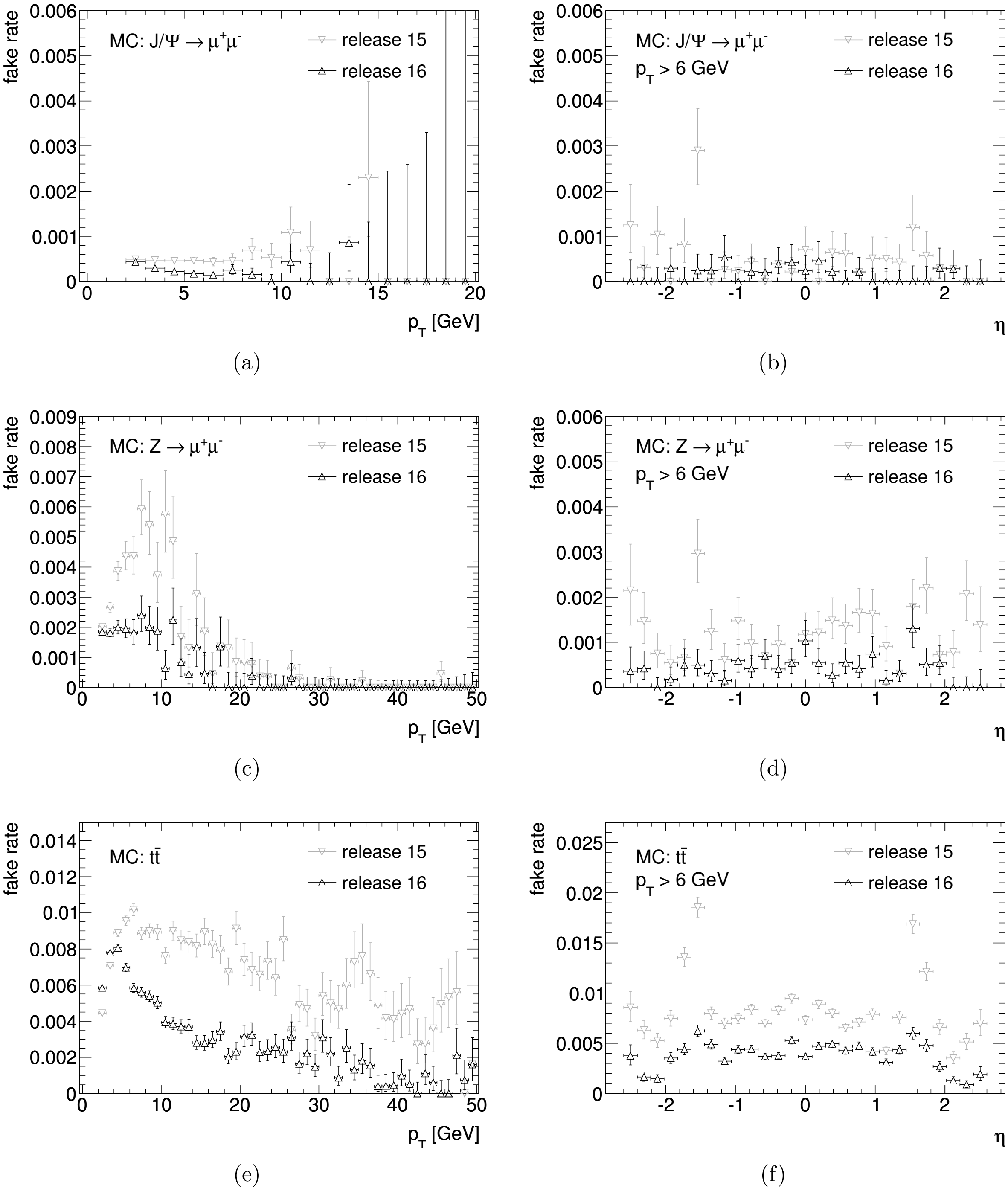

Figure 4.5: The MuTagIMO fake rate is shown as a function of transverse momentum and pseudorapidity for J/ψ, Z and $t\bar{t}$ samples reconstructed in Athena release 15 and 16. Note the different scales.

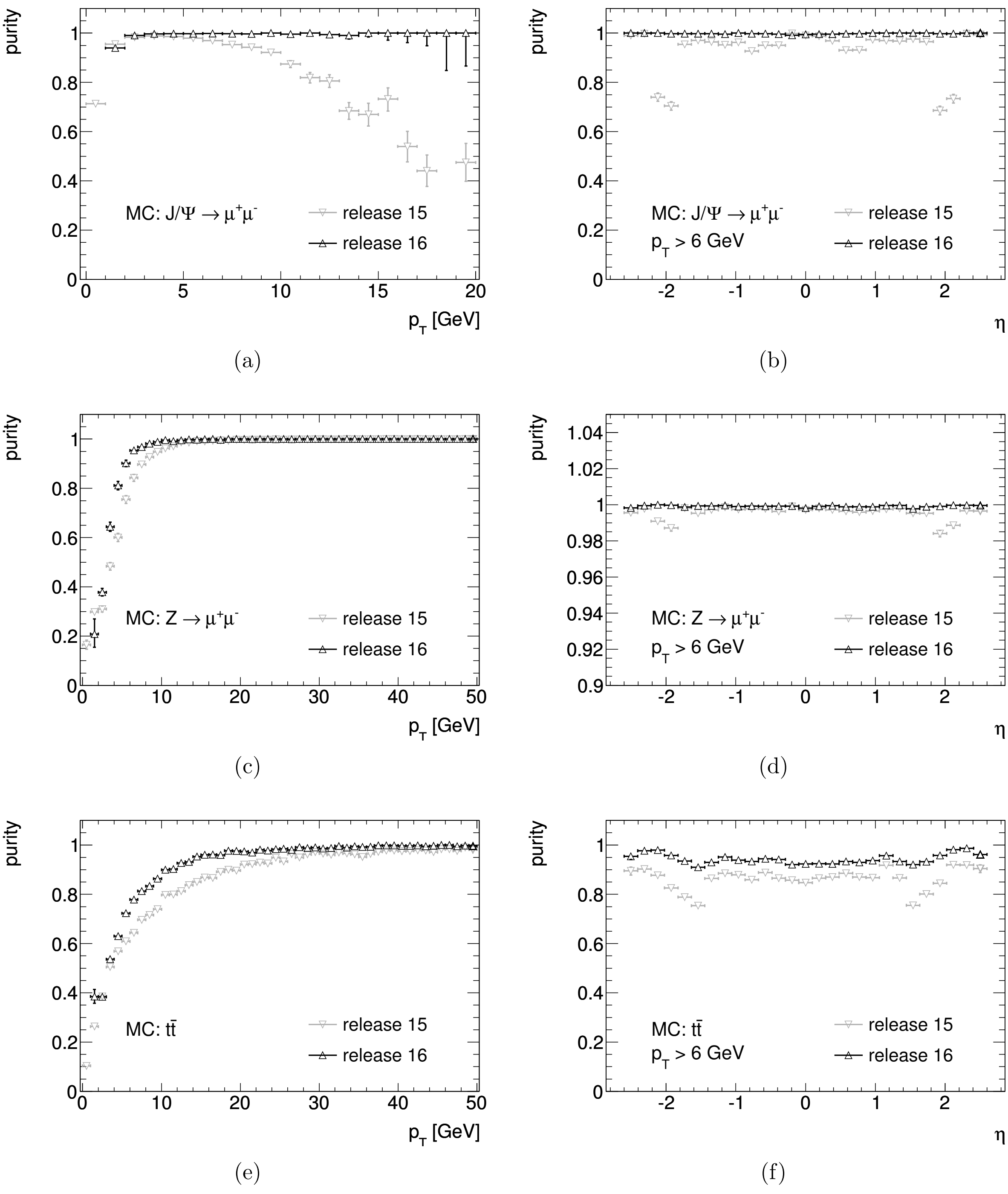

(a) (b) (c) (d) (e) (f)

Figure 4.6: The purity of MuTagIMO as a function of transverse momentum and pseudorapidity is shown for J/ψ, Z and $t\bar{t}$ samples reconstructed in Athena release 15 and 16.

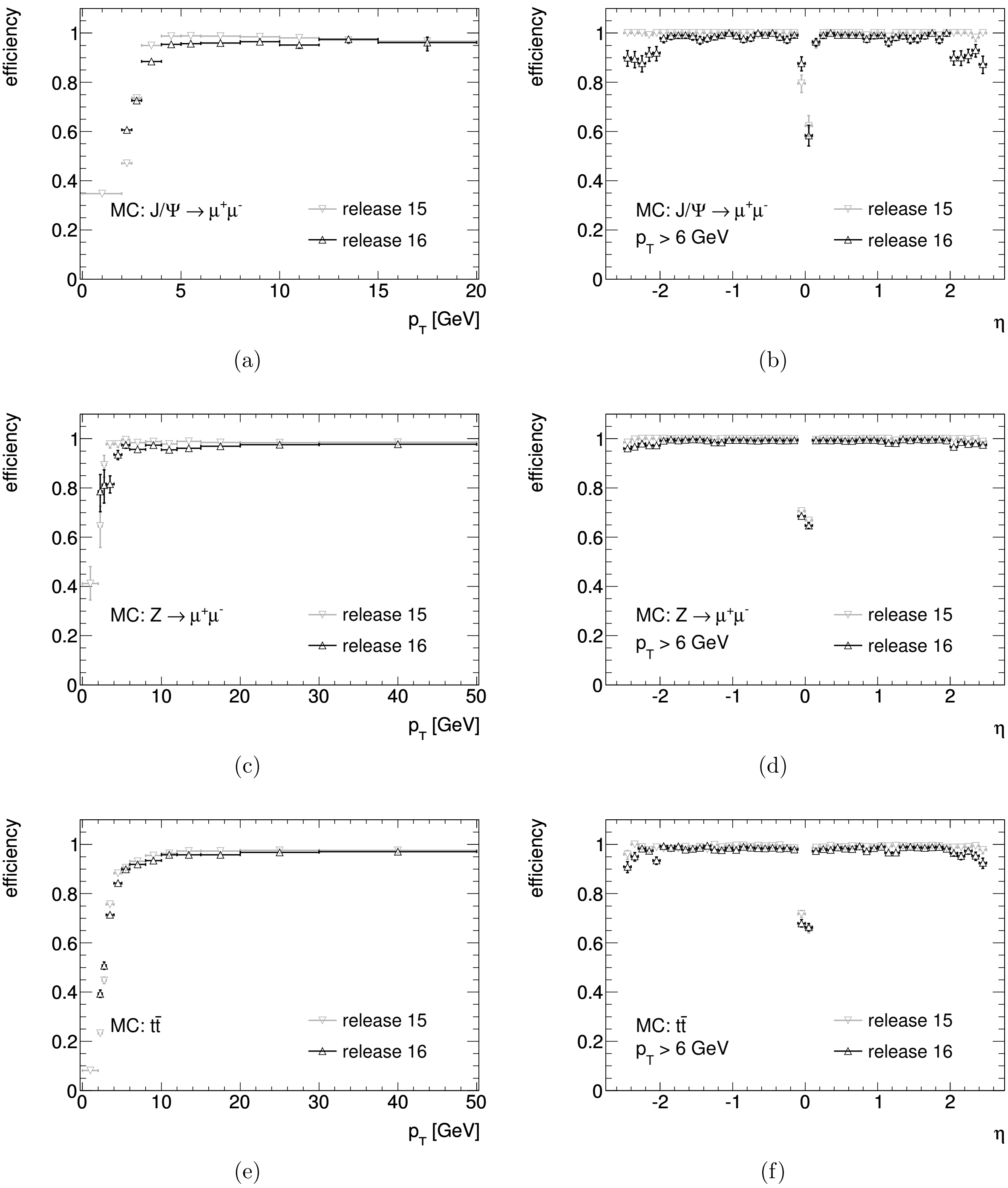

Figure 4.7: The true MuTagIMO efficiencies are shown as a function of transverse momentum and pseudorapidity for J/ψ, Z and $t\bar{t}$ samples reconstructed in Athena release 15 and 16.

Figure 4.10(a) while the number of silicon hits, i.e. Pixel Detector plus SCT hits of these tracks are shown in Figure 4.10(b). The silicon hit distribution peaks at 11 as typically 3 hits are provided by the Pixel Detector, while the SCT adds on average another 8, see 2.4. Since the MuTagIMO algorithm searches for compatible segments in all three stations of the Muon System and due to the very loose matching criteria in release 15, there are significantly more tracks with three associated segments in release 16 than in release 16.

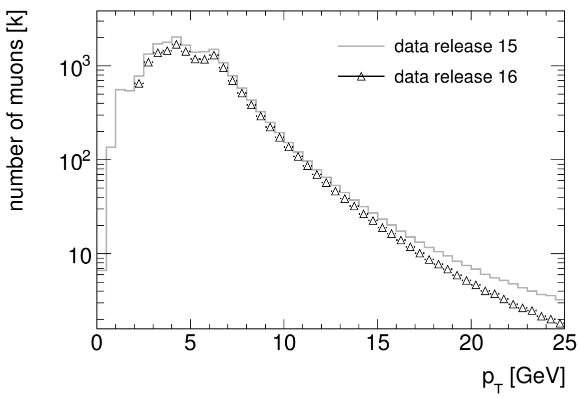

Figure 4.8: The transverse momenta of MuTagIMO muons in Athena release 15 and 16 are compared using first data. Note the logarithmic scale.

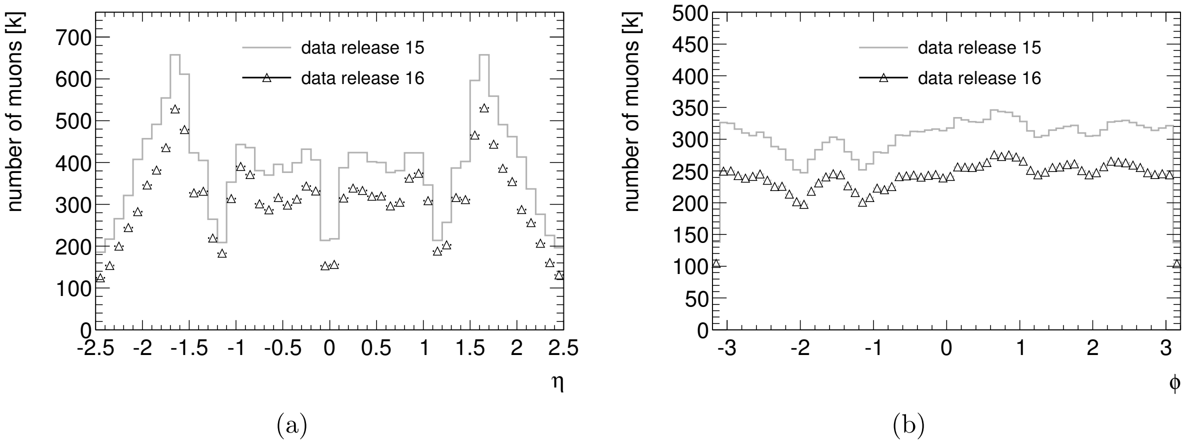

Figure 4.9: The distributions in ϕ and η for MuTagIMO muons in Athena release 15 and 16 are shown for first data.

Measuring the mis-tag rate on data is more difficult than on simulated events. One way of estimating the mis-tag rate is to check the amount of tagged muons that are not found by the corresponding combined algorithm. These muons are certainly not all mis-tagged, however, at transverse momenta of > 8 GeV the combined algorithms reach their efficiency plateaus, as will be shown in Chapter 5 and the segment taggers are expected

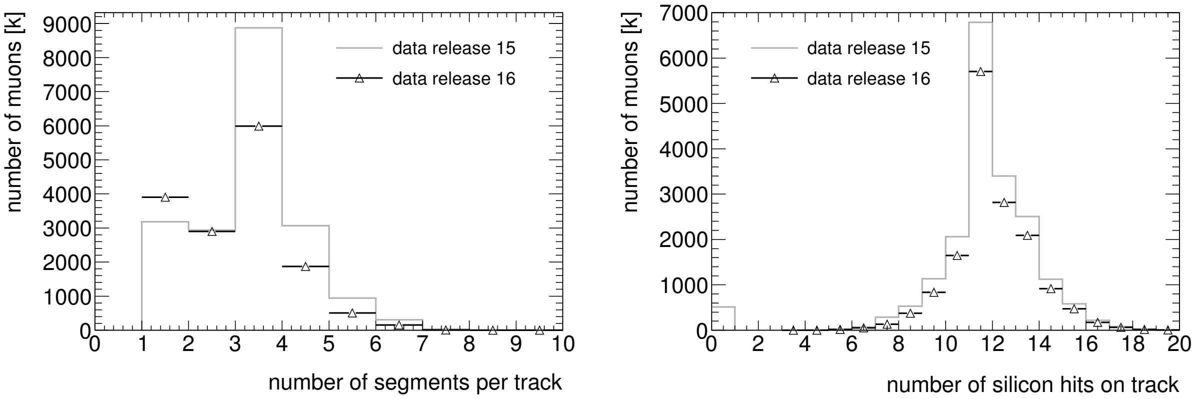

Figure 4.10: The number of associated segments and the number of silicon hits of the MuTagIMO tagged ID tracks are shown for first data reconstructed in Athena release 15 and 16.

to add only very few muons that were missed by the combined algorithms. Thus, the number of real muons added by the tagger is expected to be small and constant once the combined algorithm reaches its plateau. Figure 4.11 shows the exclusive MuTagIMO muon fraction which is defined as the ratio of MuTagIMO muons that are not identified by Muid Combined and all MuTagIMO muons, as a function of p_{T} and η. The latter shows muons with a transverse momentum larger than 12 GeV to insure that the combined algorithm reached well its plateau efficiency. In release 16 the fraction is lower over the entire p_{T} and η range. At higher muon momenta, the tightened requirements in MuTagIMO release 16 lead to a flat distribution with about 8 % of MuTagIMO muons that are missed by Muid Combined, while in release 15, this fraction keeps rising with transverse momentum, indicating that the majority of the added segment tagged muons are mistags. This finding also explains the different tails observed in the transverse momentum spectrum of all MuTagIMO muons depicted in Figure 4.8.

4.4 Conclusion

The muon segment tagger MuTagIMO was commissioned with first ATLAS data. Selections of ID tracks and MS segments were refined and the matching quantities evaluated. The requirements on existing matching quantities were tightened where needed and additional quantities were introduced. The improved performance of MuTagIMO was subsequently demonstrated on simulated Monte Carlo samples as well as on data. The fake rate was significantly reduced by about a factor 2. The purity was enhanced while the efficiency losses were kept low, amounting to less than 2 % at high muon momentum.

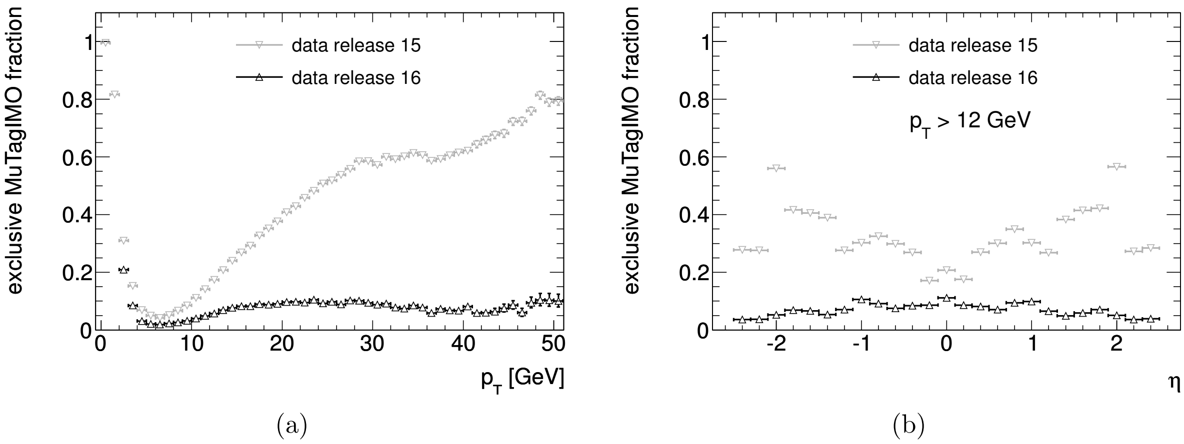

Figure 4.11: The fraction of MuTagIMO muons that were not identified by the Muid Combined algorithm is shown as a function of transverse momentum and pseudorapidity for first data processed in Athena release 15 and 16.

CHAPTER 5

Muon Identification Efficiencies

Physics analyses using muons require a detailed understanding of the performances of the muon identification algorithms. After having discussed the performance of one muon tagging algorithm, MuTagIMO in the last chapter, we will now determine the efficiencies of all ATLAS muon identification algorithms. These efficiencies are key ingredients in any cross section measurement of particles decaying into muons, as for example the W^+W^- cross section measurement that will be discussed in Chapter 6.
We chose the Tag-and-Probe method applied on the decay of J/ψ particles to measure these efficiencies. We show that this method provides an unbiased efficiency measurement of the MS identification, based on data itself. The efficiency includes these of the ID. However, the efficiencies of the trigger system will not be measured.
Since the experiments are dealing with complex event topologies in proton-proton collisions at energies never studied before, the accuracy of corresponding Monte Carlo simulations has to be verified and validated. We measure efficiencies on data and Monte Carlo simulations independently. The results are then compared and studied as a function of the transverse muon momentum for different detector regions.
This chapter is organized as follows. After choosing a dataset, the Tag-and-Probe method is explained in Section 5.2. Handling the background is the subject of 5.3. The detailed efficiency measurements on data are performed in 5.4, followed by an evaluation of the systematic uncertainties. In 5.6 efficiencies on simulated events are determined and compared to the corresponding efficiencies on data. Section 5.7 compares our results with the findings of previous studies within ATLAS. Finally, we conclude this chapter in 5.8.

5.1 Selected Dataset

We use the major part of the data recorded between the 23rd of April and the 18th of October 2010 by ATLAS, corresponding to an integrated luminosity of $\mathcal{L} = 18.13\ \mathrm{pb}^{-1}$. We select events where at least 90 % of the detector was operational and the magnets were at nominal current. In addition, at least two reconstructed muons of any type are required. To measure the muon identification efficiencies on simulated events, we use Pythia Monte Carlo samples of J/ψ particles decaying into muons [1].

5.2 Tag-and-Probe

The Tag-and-Probe method utilizes the fact that two simultaneous muons are produced in the decay of a J/ψ particle or Z-boson. Hence, two real muons are present in these events, allowing to measure muon identification efficiencies on data. While these studies can be performed on the Z-boson resonance profiting from very little backgrounds, we choose to use the low p_{T} muons from J/ψ decays. This allows us to measure the efficiency *turn-on curve* as well as the *plateau region* of the algorithms. While the turn-on curve refers to the characteristic threshold at low muon momenta where the individual algorithms become operational, the plateau region refers to the efficiency at higher transverse muon momenta where the efficiency is constant. An additional benefit of using the J/ψ instead of the Z-boson resonance is the large production cross section of the J/ψ particles, which is about two orders of magnitude larger than the Z-boson cross section. This provides the necessary statistics to probe muons in the p_{T} range from 2 to 20 GeV.

5.2.1 The Method

One of the muons from the J/ψ decay, the so called *tag*, needs to pass tight quality cuts to reject backgrounds and is in addition required to have triggered the event. The latter requirement prevents trigger biases. The tag muons should not be confused with the segment tagged or calorimeter tagged muons, see 3.6.

The other muon is called *probe*, since it is used to "probe" the algorithm under investigation. The probe muon needs to be identified by an algorithm independent of the algorithm whose efficiency is to be determined. This is of utmost importance since the measured efficiencies will otherwise be biased. Figure 5.1 illustrates the method, showing both real muons (dashed black lines) from the J/ψ decay traversing the detector. The reconstructed tag muon also fired the muon trigger (for details on the muon triggering, see 2.3.4 and 3.2). The probe is shown as a calorimeter tagged muon, or calo muon which is independent of the MS measurements used by the algorithm-to-probe to identify the same real muon. Probes identified by the algorithm under investigation are labeled *matched*. If the algorithm fails to reconstruct the probe muon, it is labeled *missed*. The invariant mass distribution of missed and matched muons is shown in Figure 5.2(b) for muons identified by Muid Combined (and MuTagIMO). For a detailed description of the algorithms, the reader is referred to 3.6.

The efficiency is then given by

$$\epsilon := \frac{matched}{matched + missed} \quad . \tag{5.1}$$

[1]The simulated dataset are available for ATLAS collaboration members, see Appendix E.2. For details on the ATLAS event simulation, see 3.3.

This efficiency is measured for different p_T and η regions to get a detailed understanding of the algorithm efficiencies and detector performance.

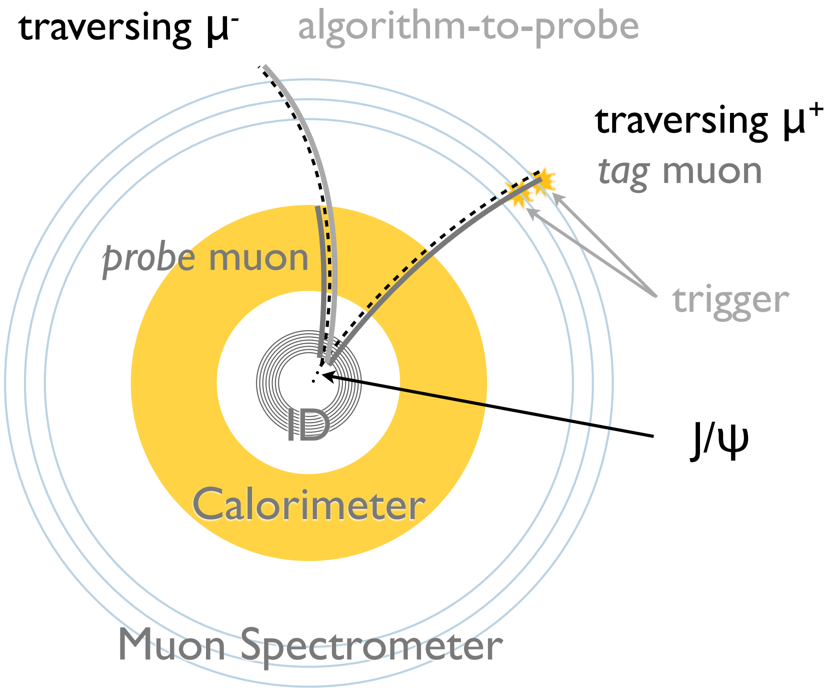

Figure 5.1: The Tag-and-Probe method is illustrated showing a J/ψ decaying into two opposite sign muons (black, dashed) in a simplified cross section of the ATLAS barrel. In the displayed example, the μ^+ is identified as the tag muon, while the probe muon is shown as the calorimeter tagged muon originating from the traversing μ^-. The muon reconstructed by the algorithm whose efficiency is to be determined is shown in light grey.

The correct choice and usage of the probe is essential for an unbiased efficiency measurement. Most commonly, all ID tracks are used as probes [2] since the ID measurements are independent of the MS measurements. However, in proton-proton collisions there are many tracks, originating mainly from QCD processes [3]. Hence, an efficiency measurement based on ID tracks faces a large background, which results in relatively large systematical errors. To reduce these errors, we use calo muons, see 3.6.5. Since the calorimeter provides again MS independent measurements, this additional requirement on the probe does not affect or bias the measured efficiencies, but reduces the background significantly and hence leads to a preciser measurement. Figure 5.2 shows the invariant $\mu^+\mu^-$ mass spectrum of the tag and probe pair (without the cut on the invariant mass). A subset of the selected dataset, corresponding to 3 pb^{-1} of integrated luminosity is used for this comparison. In Figure 5.2(a) [44] ID tracks are used as probes while Figure 5.2(b) shows

[2] The probe muon is hence not required to be identified as a muon by a muon algorithm in this case.
[3] The average number of ID tracks per event in the selected data sample is ≈ 12 [43].

the same spectrum using calo muons as probes. The visible peak at the J/ψ mass in the unmatched/missed probe distributions show the inefficiencies of the algorithms. These inefficiencies become significantly smaller if the muon segment tagger muons are added to the combined muons, as is visible in the plots. Comparing Figures 5.2(a) and 5.2(b) the large number of unmatched probes in Figure 5.2(a), corresponding to the large background introduced with the ID track probes becomes apparent.

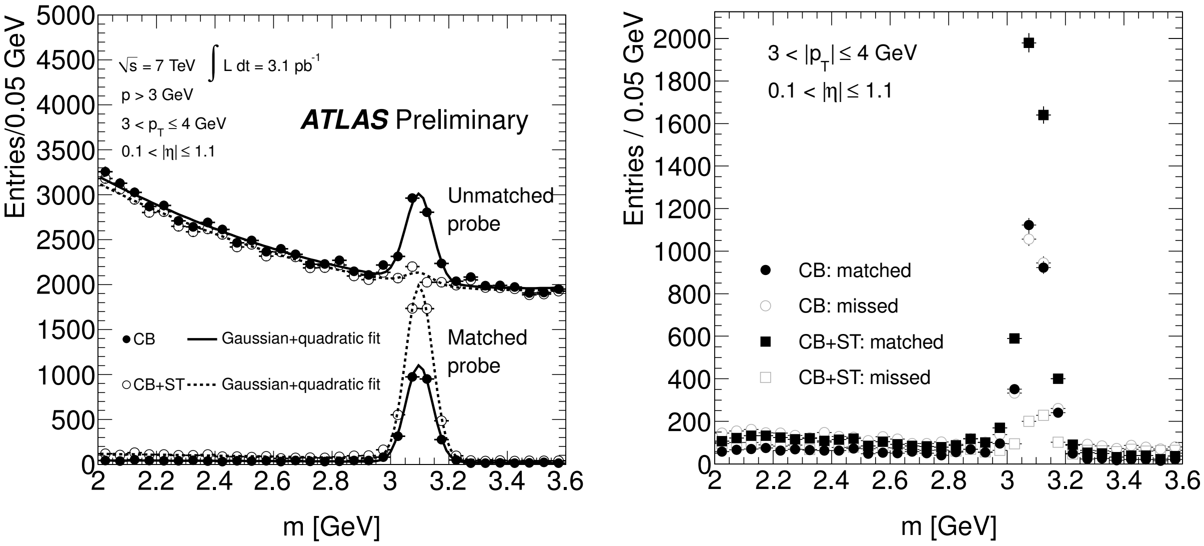

(a) ID track probes

(b) calo muon probes

Figure 5.2: The invariant $\mu^+\mu^-$ mass spectrum of the tag and probe pair is shown for probes that were matched and for those that were missed/unmatched by the respective algorithm(s). Here, these algorithms are the combined muon algorithm (CB) with and without adding segment tagged (ST) muons.

The requirements on the probe muon are independent of the muon identification in order to not bias the efficiencies in any way. The momentum cut on the probe muon rejects calo muons, whose momentum is too low to reach the muon spectrometer. The additional requirements on tag and probe tracks further reduce muon pairs in the selection that do not come from a J/ψ decay. The charges, invariant mass and the common vertex are calculated from Inner Detector measurements.
The requirements on the tag and probe muons are as follows:

1. **tag muon** requirements

   - identified as combined muon (see 3.6.2)
   - $p_T > 4$ GeV

- fired muon trigger and hence caused the event to be recorded (for detailed trigger requirements see Appendix B)
- ID track quality cuts (for details see Appendix C)

2. **probe muon** requirements

- identified as calo muon (see 3.6.5)
- $p > 3$ GeV
- same ID track quality cuts as on the tag muon

3. **additional requirements** on the tag and probe pair

- opposite charge : $\mu^+\mu^-$
- invariant mass at J/ψ resonance : $m_{\mu^+\mu^-} \in [2.65; 3.55]$ GeV
- coming from a common vertex, i.e. a common vertex can be successfully fitted to the two ID tracks of the muons : $\chi^2_{vertexfit} < 6$

5.2.2 The Selected Tag

Out of all muons identified by the Muid muon algorithms in the selected dataset, 20.9 % fulfilling the requirements on a tag muon. Figure 5.3 shows some key distribution of selected tag muons. Their spatial distribution is shown in Figure 5.3(b) while the projection in ϕ and η are shown in 5.3(a) and (d). The corresponding p_T-spectrum is shown in Figure 5.3(c). The peaks at 6 GeV, 10 GeV and 13 GeV results from events where the threshold of the lowest unprescaled trigger was set to the corresponding values, see Appendix B for details.

5.2.3 The Selected Probe

As mentioned in 5.2.1 we use calo muons as probes. Besides being independent of the MS system and providing a significantly cleaner J/ψ signal compared to ID probes, there are additional characteristics that are important. One essential feature of the probe is its global distribution. Since the muon identification efficiencies depend strongly on the geometrical detector regions that are traversed by the muons, all parts of the detector need to be covered in order to not introduce biases to the overall efficiencies. Figure 5.4(b) shows an $\eta - \phi$ map of the selected calo muon probes, while Figure 5.4(a) and (d) show the respective projections. As the plots shows, the full detector is covered.
Another desired characteristic of the probe is a high efficiency. This leads to large statistics and hence smaller statistical uncertainties on the measured efficiencies. The integrated efficiency of the calorimeter taggers is measured to be 76.7 ± 0.2 % for muons with $p_T \geq 2$ GeV and reaches 85.4 ± 0.2 % for muons with $p_T \geq 4$ GeV. To measure this efficiency, the Tag-and-Probe technique is used with combined muons as probes to test the independent calo muon algorithm. The efficiency as a function of p_{T} and η is shown in Figure 5.5.

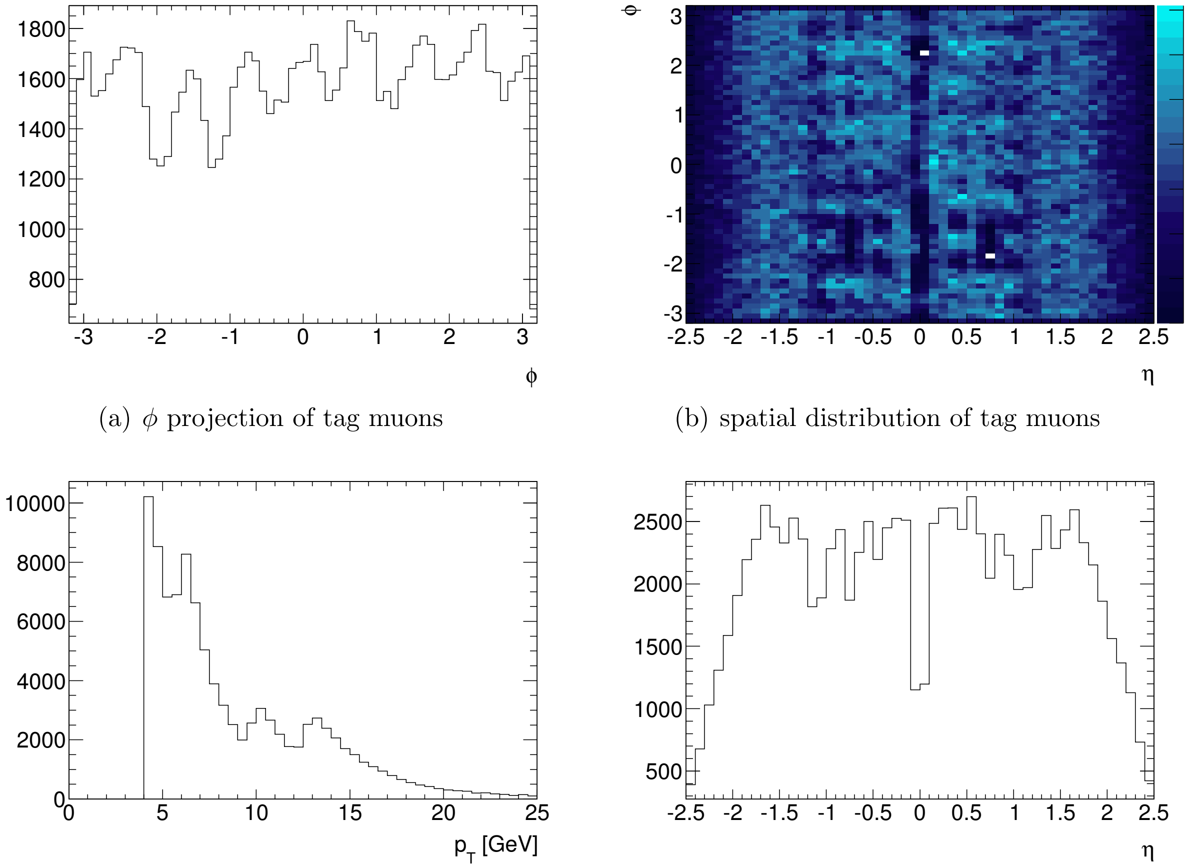

(a) ϕ projection of tag muons

(b) spatial distribution of tag muons

(c) transverse momentum of tag muons

(d) η projection of tag muons

Figure 5.3: (a) shows an $\eta - \phi$ map and (b) the p_{T}-spectrum of tag muons in events that pass the Tag-and-Probe selection.

The missing efficiency at $\eta = 0$ is due to the MS acceptance hole (see 2.3.4), where no combined muons to probe the calorimeter tagger can be reconstructed.
The calorimeter tagger requires an ID track with a transverse momentum of $p_T \geq 2$ GeV. The entire p_T-spectrum of the selected probe muons, i.e. the probes found in events where also a corresponding tag muon was found and the additional requirements of the tag and probe pair are fulfilled is shown in Figure 5.4(c).
We conclude, that the calo muons are suitable probes for the subsequent measurements.

5.3 Background

Although the calo muons provide a clean signal selection, a small background contamination is still present, as visible in the sidebands in Figure 5.2(b). We use a *sideband subtraction* method to measure the background in the mass window region. The background contamination under the J/ψ signal is estimated from two equally sized intervals

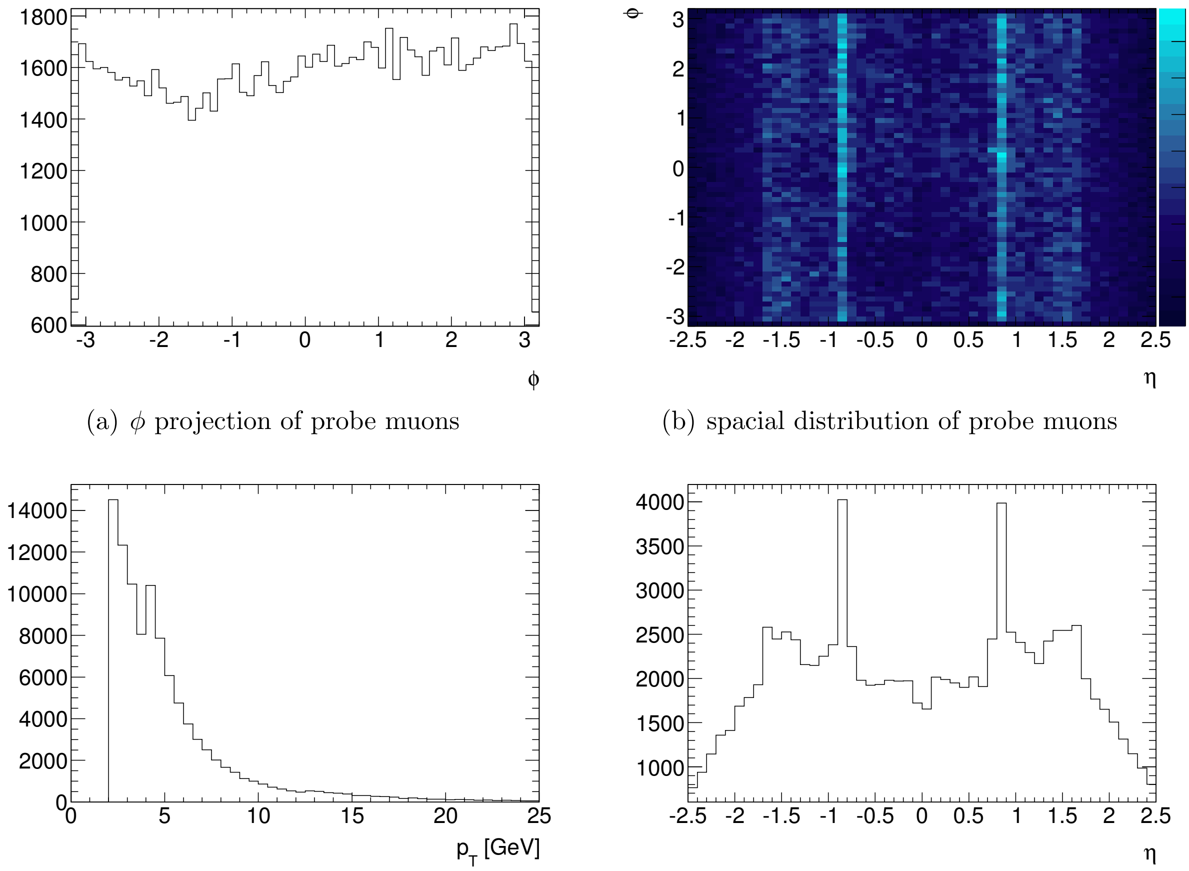

(a) ϕ projection of probe muons

(b) spacial distribution of probe muons

(c) transverse momentum of probe muons

(d) η projection of probe muons

Figure 5.4: (a) shows an $\eta - \phi$ map and (b) the p_{T}-spectrum of probe muons in events that pass the Tag-and-Probe selection.

above and below the J/ψ resonance in the invariant $\mu^+\mu^-$ mass spectrum. We use the intervals $[2.65, 2.95[$ GeV and $]3.25, 3.55]$ GeV as our sidebands, while the signal region is defined as $[2.95, 3.25]$ GeV. The sidebands are then subtracted from the signal region to obtain an estimate of the J/ψ signal. The efficiency given in equation 5.1 is hence modified to

$$\epsilon := \frac{matched - (\Delta_{matched}/2)}{matched - (\Delta_{matched}/2) + missed - (\Delta_{missed}/2)} \quad . \tag{5.2}$$

Δ_{missed} refers to the probes in the sidebands that were missed and $\Delta_{matched}$ correspondingly to the once that were matched. The factor $1/2$ results from the size of the sidebands compared to the signal region.

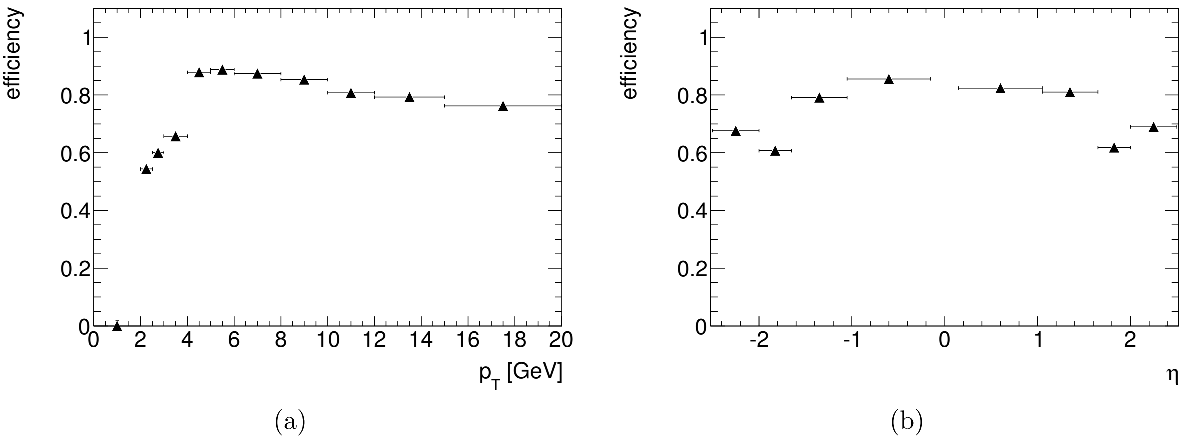

Figure 5.5: The efficiency of the ATLAS calorimeter muon tagger is shown as a function of transverse momentum (a), and pseudorapidity (b).

5.4 Measured Efficiencies

The efficiencies are measured as a function of the transverse muon momentum for four eta bins, corresponding to four different detector regions. They are grouped into efficiencies of the combined algorithms, the segment taggers and the combination of the two. The displayed errors are statistical. A detailed list of systematic errors can be found in Table 5.1.

5.4.1 Combined Muons

As described in 3.6.2 and 3.6.4 the Muid algorithm family consists of two independent combined muon identification algorithms, Muid Combined and MuGirl refitted. Both perform very well, showing a steep turn-on curve at low transverse momenta and a high efficient, flat plateau for $p_{\mathrm{T}} > 6$ GeV, see Figures 5.6. Combining the two algorithms leads to an outstanding efficient muon reconstruction, showing very steep turn-on curves as well as a flat plateau at efficiencies close to one for all detector regions. This combination is hence used by various physics analyses throughout ATLAS.
The combined algorithm of the Staco collection shows particularly in the detector barrel a significantly flatter turn-on curve than the Muid combined algorithms (see Figure 5.6(a)), reaching the plateau region only at $p_{\mathrm{T}} > 12$. This efficiency loss at low transverse momentum can be partially recuperated using MuTag, the segment tagger of the Staco collection, as will be shown in 5.4.3.

5.4.2 Segment Tagged Muons

Figure 5.7 shows the efficiencies of the 2 independent Muid segment taggers, MuTagIMO and MuGirl. MuTag is not independent and only adds muons that were missed by Staco

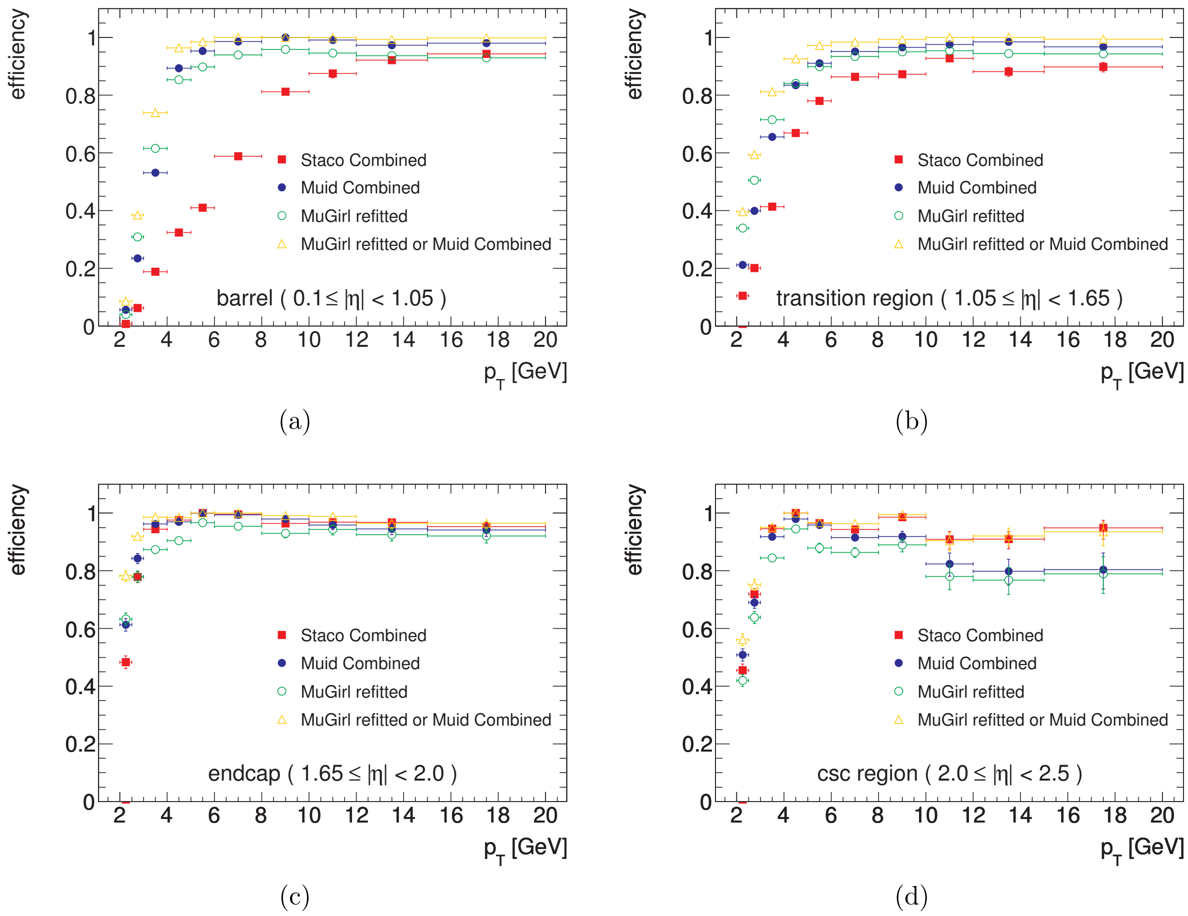

Figure 5.6: The efficiency of the ATLAS combined muon algorithms are shown for four detector regions.

Combined, see 3.6.3 [4]. Therefore, a direct comparison with the Muid segment taggers does not make sense and we do not include the MuTag efficiency in Figure 5.7.
Both, MuTagIMO and MuGirl show the high efficiencies expected from segment tagger algorithms. The major difference between the two is the turn-on curve, clearly visible for $|\eta| \leq 2$, see Figures 5.7(a), 5.7(b), 5.7(c). While the steep turn-on curve of MuGirl starts at an efficiency $\approx 10\,\%$ for a transverse muon momentum of 2 GeV in the barrel region, MuTagIMO already reaches almost $60\,\%$. Throughout all detector regions, MuTagIMO reaches its plateau sooner than MuGirl, at approximately 5 GeV, and is on average about $4\,\%$ points more efficient in the plateau.

[4]The MuTag efficiencies hence drop with p_{T} to values close to 0 once Staco Combined reaches its plateau. It is meant to be used in combination with Staco, see 5.4.3.

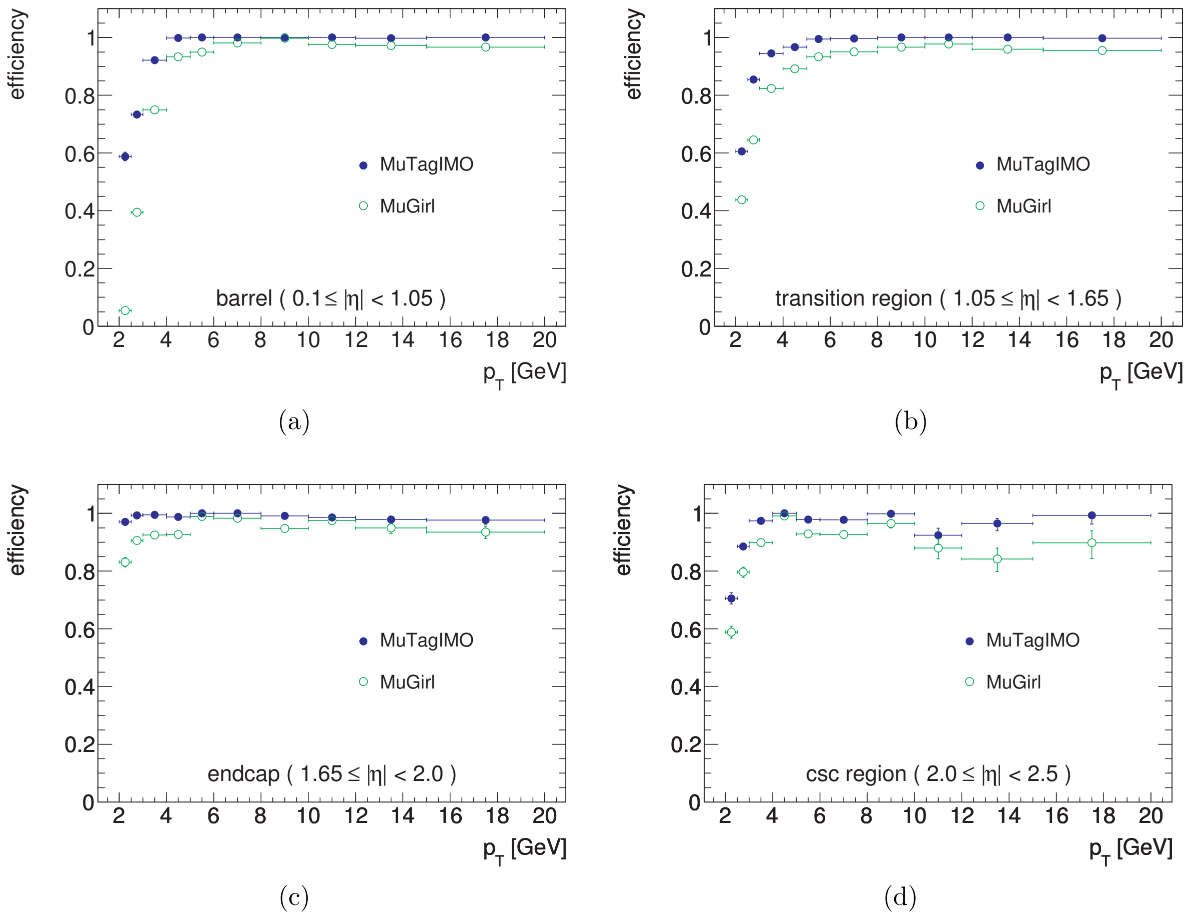

Figure 5.7: The efficiency of the ATLAS segment tagged muon algorithms of the Muid family are shown for four detector regions.

5.4.3 Segment Tagged or Combined Muons

The combination of combined algorithm and segment taggers yields the most efficient muon identification. Since MuGirl refitted takes MuGirl muons as an input, the combination of these two algorithms is omitted and only the combination of MuTagIMO and Muid Combined as well as MuGirl and Muid Combined are shown for the Muid collection. Performances, particularly for MuTagIMO in combination with Muid Combined are excellent and in all detector regions higher or equal to the two other algorithm combination shown in Figure 5.8. Though MuTag can recuperate a large part of the Staco Combined efficiency losses at low p_{T}, seen in 5.4.1, it does not reach the performance of the high efficient MuTagIMO - Muid Combined combination. Since MuTag does not tag ID tracks with $|\eta| > 2$ the Staco or MuTag efficiency drops significantly for low momenta in Figure 5.8(d). The late turn-on of MuGirl in the detector barrel, seen in 5.4.2 propagates into its combination with Muid Combined, compare Figures 5.7(a) and 5.8(a).
The plateau efficiencies reach a similar level for all algorithm combinations. The largest

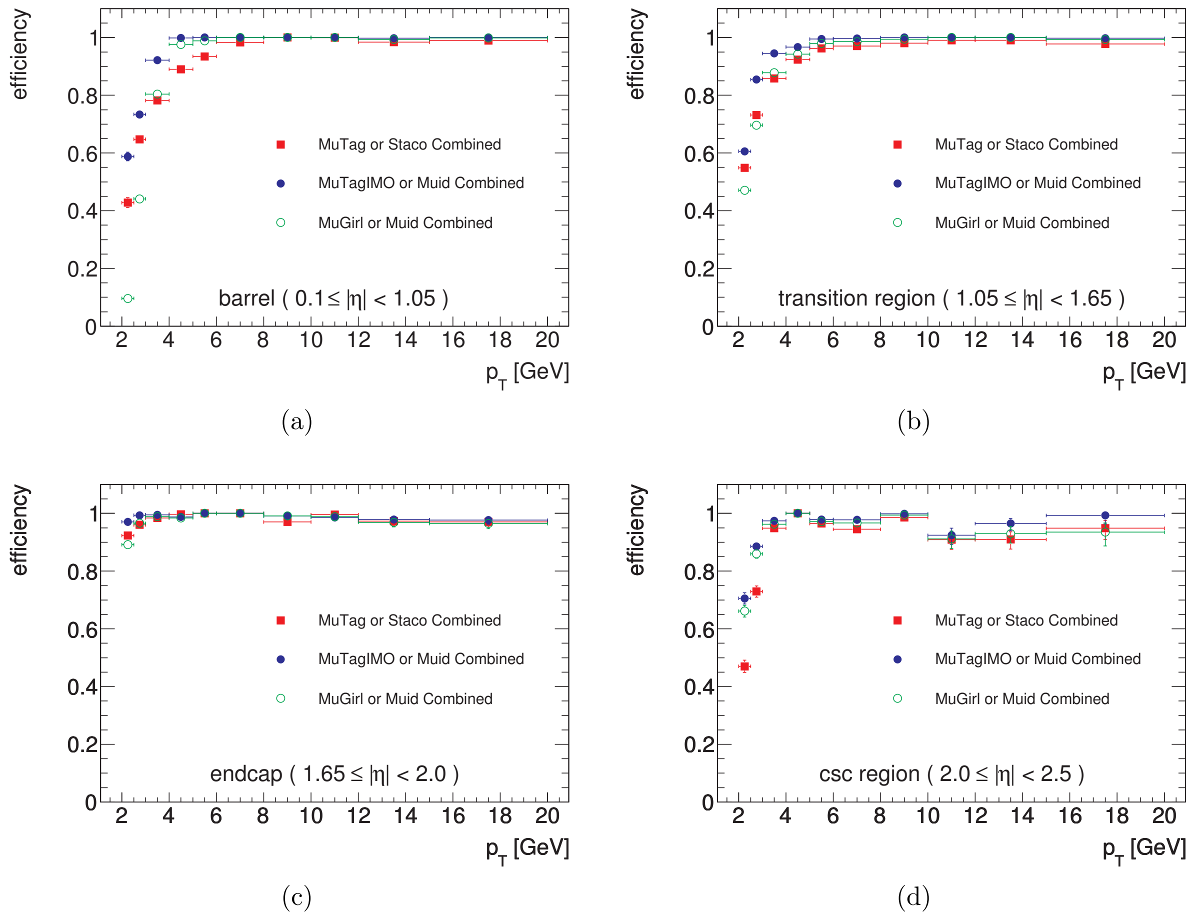

Figure 5.8: The efficiency of the combination of segment tagged and combined muon algorithms are shown for four detector regions.

discrepancy is observed comparing the MuTagIMO - Muid Combined combinations to the Staco combination, with the Muid combination being on average approximately 2 % points more efficient in the plateau region, see Table 5.1.

5.5 Systematic Uncertainties

The systematic uncertainties on the performed efficiency measurements are studied for the following sources:

1. **trigger**: The tag muon is required to be matched to the corresponding L2 muon triggers for the first data periods up to period F. For the later periods, statistics of muons firing the next higher threshold triggers is sufficient and we require the tag muon to be matched to `EF_mu13` for data periods $F2_2$ to G4 and `EF_mu15` for G5, G6 and H, which makes the bulk of the data sample. Details on the data periods

and corresponding triggers are given in Appendix B.

2. **calorimeter identification**: Two independent calorimeter taggers are available, as discussed in 3.6.5. For our efficiency measurement we do not distinguish between calo muons reconstructed by one or the other. We evaluate the systematics introduced by the calorimeter taggers by choosing only muons reconstructed by one of them, the CaloLikelihood tagger. Systematics are calculated for 4 independent detector regions individually, corresponding to the η binning used for the efficiency plots shown in 5.4. The quoted systematics are the weighted average of the systematics uncertainties in these detector regions. The weight is given by the number of tag and probe pairs in the corresponding detector region.

3. **sideband subtraction**: The size of the sidebands as well as the signal region are increased from 0.3 GeV to 0.4 GeV, subtracting events in the intervals $[2.5; 2.9[$, $]3.3, 3.7]$ GeV from the signal region $[2.9, 3.3]$ GeV.

4. **background shape**: To evaluate possible systematic uncertainties introduced by the chosen background subtraction method, we simultaneously fit the distributions of missed and matched probe muons as a function of the invariant dimuon mass in the region $m_{\mu^+\mu^-} \in [2, 3.6]$ GeV. The fit model describing the J/ψ signal in the matched probes distribution is a double-sided exponential that is convoluted with a gaussian. The signal in the missed probe distribution, which corresponds to the inefficiency of the algorithm under investigation is modeled using a Breit-Wigner function convoluted with a gaussian. The backgrounds are modeled by the added background functions.

$$\begin{aligned} f_{matched}(m) &= \epsilon N \left(\left[H(\mu) e^{-\gamma m} + (1 - H(\mu))\, e^{\gamma m} \right] * e^{-\frac{1}{2}(\frac{m}{\sigma_{matched}})^2} \right) + b_{matched}(m) \\ f_{missed}(m) &= (1-\epsilon) N \left(\frac{1}{(m-\mu)^2 + \frac{1}{4}\sigma_{missed}^2} * e^{-\frac{1}{2}(\frac{\mu}{\delta})^2} \right) + b_{missed}(m) \end{aligned} \tag{5.3}$$

N denotes the number of muon pairs in the signal peak, μ the mean and the σ_x are the widths of the signal distributions. γ and δ are additional free parameter. H depicts the Heaviside function. The $b_x(m)$ are the background functions. The efficiency ϵ obtained from the fit is compared to the one measured using the sideband subtraction method. All parameters in the functions are left free for the fit.
Choosing a linear background $b_x(m) = \alpha_x m + \beta_x$ confirms the results found by the sideband subtraction method precisely. This is expected since the sideband subtraction method assumes a linear background shape. The systematic uncertainties are obtained using an exponential background $b_x(m) = \alpha_x e^{\beta_x m}$. Since statistics, particularly for higher p_{T} bins in the missed probe muons distribution is too low to obtain stable fit results, we fit the distributions for the integrated statistics $p_{\mathrm{T}} > 2$ GeV and $-2.5 < \eta < 2.5$ and assume this uncertainty to be a constant, i.e. independent of p_{T} and η.

5. **kinematic selection**: The p_T requirement on the tag muon is increased to 4.5 GeV.

6. **purity of selection**: An additional requirement on the tag muon is introduced, to further purify the selection. We require the scattering significance of the tag muon to be smaller than 0.2 [45]. This quantity is only available for the muon algorithms of the Muid family.

Table 5.1 lists the 6 individual contributions to the overall systematic uncertainties, which is the squared sum of these contributions, of the measured efficiencies for muons above certain p_T values. The contribution from the background shape is obtained from the fit of the full statistics and is listed as a constant for each p_{T} value. The large systematic uncertainties on the calorimeter identification for the Staco Combined algorithm are due to the strong η dependence of its efficiency. Although, differences of the underlying η distributions of the two independent calorimeter taggers are taken into account for the different detector regions, some differences within the detector regions remain. This holds particularly for the detector barrel, where the Staco Combined efficiencies drop significantly for $|\eta| < 0.8$, see Figure 5.9. This strong dependence on η leads to the large observed systematic uncertainty.

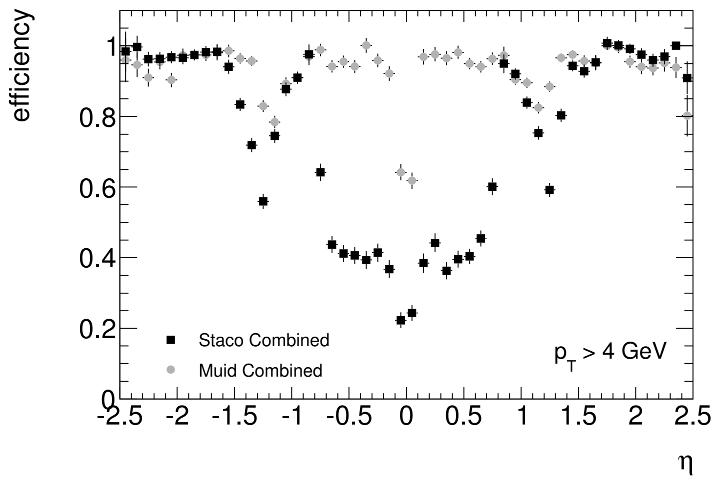

Figure 5.9: Staco and Muid Combined efficiencies as a function of pseudorapidity are compared for muons with at least four GeV transverse momentum.

algorithm	p_T [GeV]	ϵ	statistical error +	statistical error -	systematic error	trigger	calo id	sidebands	background shape	kinematic selection	background
Muid Combined	$p_T > 2$	72.49	0.68	0.67	2.98	0.39	2.52	-0.76	0.78	-1.09	0.07
	$p_T > 4$	92.75	0.37	0.39	1.44	-0.02	0.78	-0.92	0.78	0.02	-0.02
	$p_T > 8$	95.27	0.56	0.60	1.45	-0.01	1.15	-0.39	0.78	0.11	-0.03
	$p_T > 12$	94.60	0.62	0.68	1.07	0.06	0.69	-0.10	0.78	0.17	0.09
MuGirl refitted	$p_T > 2$	72.80	0.69	0.68	1.99	-0.04	1.22	-0.67	1.26	-0.62	0.19
	$p_T > 4$	89.29	0.46	0.48	1.84	-0.37	0.81	-0.99	1.26	0.11	0.08
	$p_T > 8$	91.88	0.71	0.75	2.25	-0.44	1.79	-0.21	1.26	0.15	0.10
	$p_T > 12$	91.30	0.82	0.87	1.61	-0.25	0.96	-0.06	1.26	0.16	0.03
Muid Combined + MuGirl refitted	$p_T > 2$	81.35	0.68	0.68	1.34	0.21	0.48	-0.76	0.59	-0.76	0.15
	$p_T > 4$	96.74	0.25	0.27	1.32	-0.13	0.58	-1.02	0.59	0.03	0.07
	$p_T > 8$	97.96	0.43	0.47	1.05	-0.04	0.74	-0.45	0.59	0.06	0.07
	$p_T > 12$	97.64	0.43	0.48	0.85	0.00	0.52	-0.30	0.59	0.07	0.09
Staco Combined	$p_T > 2$	55.68	0.71	0.70	5.37	-0.39	5.20	-1.21	0.05	-0.41	
	$p_T > 4$	73.52	0.79	0.80	5.26	-0.94	5.01	-1.26	0.05	0.30	
	$p_T > 8$	89.07	0.88	0.92	2.13	-0.66	1.97	-0.45	0.05	0.14	
	$p_T > 12$	91.58	0.85	0.90	1.75	-0.72	1.58	-0.19	0.05	0.13	
MuTagIMO	$p_T > 2$	91.71	0.52	0.53	0.98	0.08	0.47	-0.68	0.27	-0.43	0.13
	$p_T > 4$	98.67	0.14	0.16	1.07	-0.06	0.40	-0.95	0.27	0.04	0.10
	$p_T > 8$	99.00	0.34	0.39	0.84	0.09	0.63	-0.45	0.27	0.06	0.10
	$p_T > 12$	98.67	0.34	0.40	0.77	0.18	0.62	-0.28	0.27	0.08	0.14
MuGirl	$p_T > 2$	80.19	0.68	0.68	2.02	-0.15	1.71	-0.73	-0.56	-0.50	0.15
	$p_T > 4$	93.60	0.37	0.38	1.84	-0.31	1.38	-1.02	-0.56	0.11	0.02
	$p_T > 8$	95.04	0.57	0.61	1.46	-0.26	1.28	-0.33	-0.56	0.10	-0.00
	$p_T > 12$	94.26	0.67	0.72	1.26	-0.18	1.07	-0.29	-0.56	0.09	-0.02
MuTagIMO + Muid Combined	$p_T > 2$	91.71	0.52	0.53	0.98	0.08	0.47	-0.68	0.27	-0.43	0.13
	$p_T > 4$	98.67	0.14	0.16	1.07	-0.06	0.40	-0.95	0.27	0.04	0.10
	$p_T > 8$	99.00	0.34	0.39	0.84	0.09	0.63	-0.45	0.27	0.06	0.10
	$p_T > 12$	98.67	0.34	0.40	0.77	0.18	0.62	-0.28	0.27	0.08	0.14
MuGirl + Muid Combined	$p_T > 2$	84.52	0.66	0.66	1.22	0.05	0.58	-0.78	0.37	-0.61	0.16
	$p_T > 4$	97.21	0.23	0.25	1.22	-0.14	0.55	-1.02	0.37	0.04	0.08
	$p_T > 8$	98.07	0.41	0.46	0.93	-0.00	0.72	-0.44	0.37	0.05	0.10
	$p_T > 12$	97.74	0.43	0.49	0.74	0.03	0.55	-0.29	0.37	0.06	0.13
MuTag + Staco Combined	$p_T > 2$	85.69	0.68	0.69	1.86	0.19	1.50	-0.60	0.82	-0.36	
	$p_T > 4$	95.33	0.36	0.37	1.21	0.00	0.49	-0.72	0.82	0.15	
	$p_T > 8$	97.51	0.45	0.50	1.25	-0.20	0.84	-0.36	0.82	0.11	
	$p_T > 12$	97.16	0.52	0.59	0.99	-0.15	0.45	-0.28	0.82	0.03	

Table 5.1: Efficiencies of all muon algorithms available for the ATLAS detector, as well as sensible combinations of algorithms are listed with statistical and systematic uncertainties. The efficiencies are integrated over η and displayed for different transverse momenta. The total systematic error is the squared sum of the individual contributions. All values are in %.

5.6 Monte Carlo - Data Comparisons

The efficiencies shown in the previous section are now compared to the corresponding efficiencies from simulation. The scaling factor is defined as

$$\text{scaling factor} := \frac{\epsilon_{data}}{\epsilon_{simulation}} \quad . \tag{5.4}$$

The asymmetric statistical errors of the efficiencies are propagated individually for the upper and lower errors. No systematic errors are shown in the plots. The average scaling factor per eta region is shown on the corresponding plot and is obtained by fitting a constant over the full p_{T}-range.
While the plateau regions of the algorithms are expected to show a good agreement between data and Monte Carlo, a similar level of agreement will be very challenging to achieve for the turn-on curves. Already small differences in the material description can shift the thresholds and since the algorithm turn-on curves are very steep, this results in significant disagreements.
Figures 5.10 and 5.11 show the scaling factors (sf) as a function of transverse momentum for the individual muon algorithms and their combinations listed in Table 5.1, for the four previously defined detector regions.

5.6.1 Combined Muons

Data and simulation agree well for combined muons, as shown in the top four rows of Figures 5.10 and 5.11. Some fluctuating discrepancies are observed in the threshold curves and partially do not lie within the plotting range [5]. However, as will be shown in 5.6.3, adding more statistics to the low momentum bins decreases the observed discrepancies, which indicates that they are mainly of statistical nature.
The plateau regions are in good agreement for all Muid algorithms while Staco combined shows some small deviations of several percent in the transition and forward region.

5.6.2 Segment Tagged Muons

Both Muid segment taggers show a good agreement between data and simulation as the central rows in Figures 5.10 and 5.11 show. Even the threshold curve of MuTagIMO shows an excellent agreement, while for the MuGirl one only minor deviations are observed. The efficiencies in the plateau regions are also well described. The scaling factors for MuGirl in the transition and endcap region suggest that the Monte Carlo plateau efficiencies in this region are systematically overestimated by a few percent. However, on average, data and simulation efficiencies of MuGirl agree within two percent. The MuTagIMO efficiencies in data and simulation even agree on a per-mill level.
As in 5.4.2 we omit MuTag at this point and show instead the agreement of the combination of MuTag and Staco Combined in the subsequent subsection.

[5] See Appendix D for the values and errors of these scaling factors.

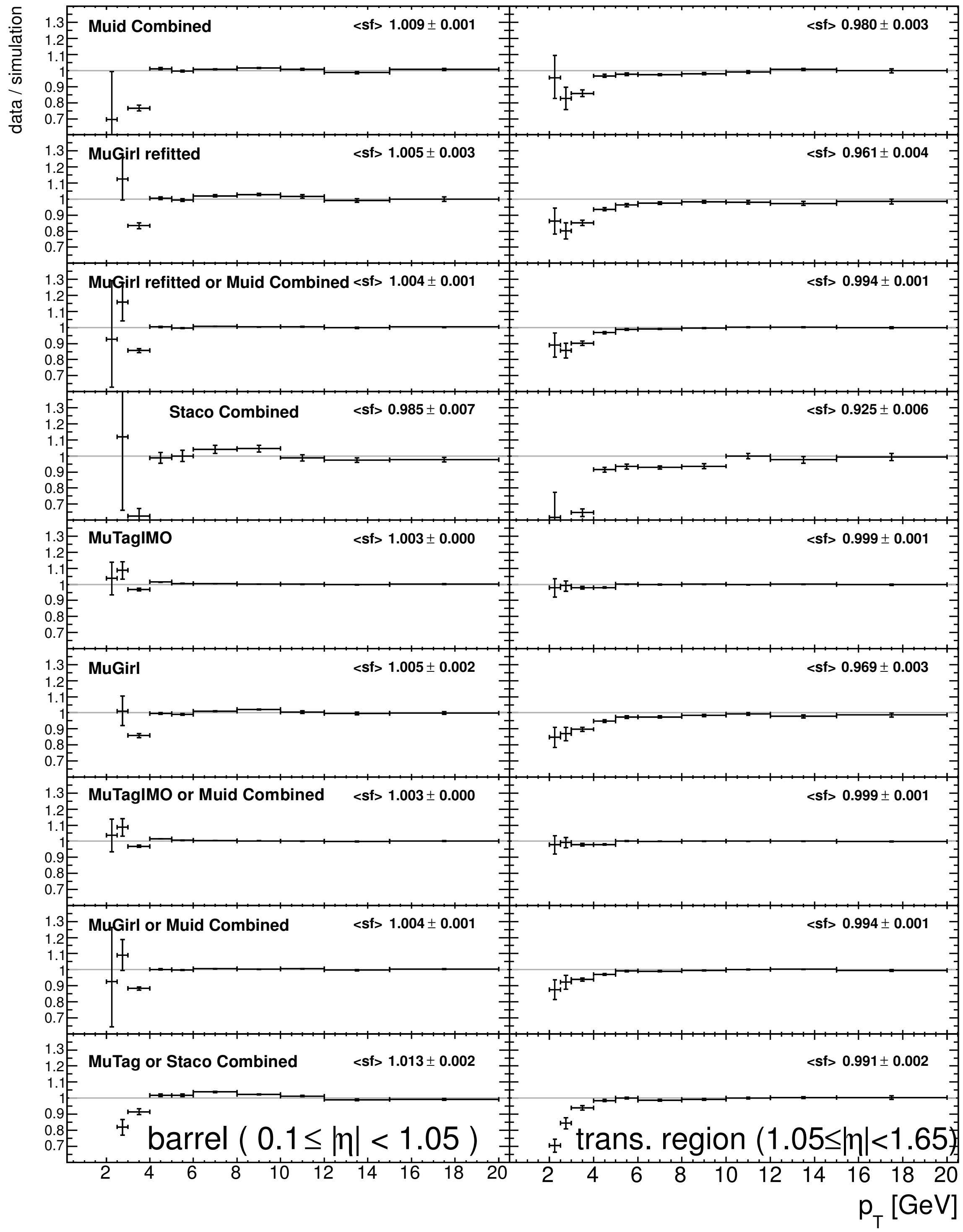

Figure 5.10: The ratios of efficiencies on data and simulation are shown for the barrel and transition region for all ATLAS muon identification algorithms and various of its combinations.

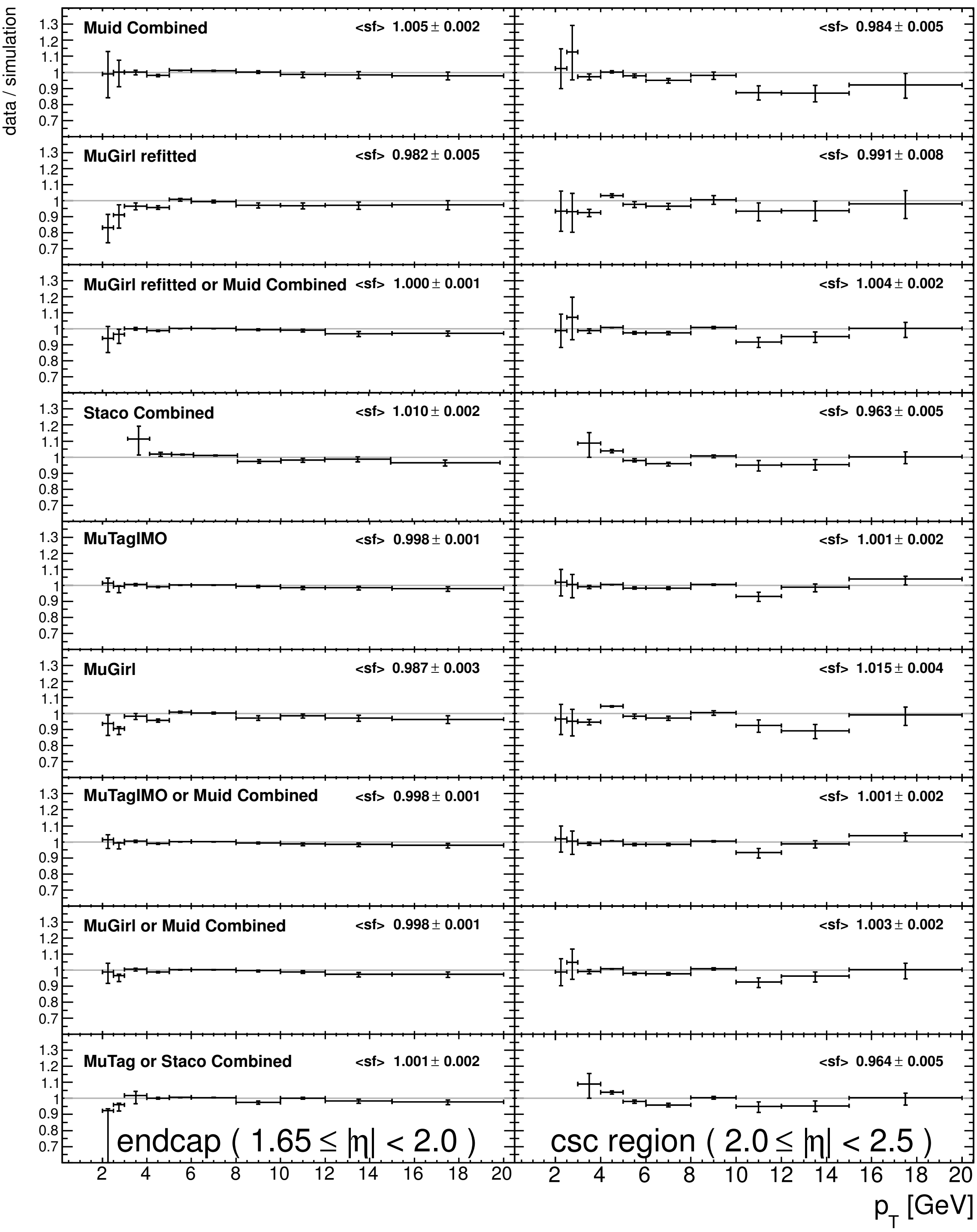

Figure 5.11: The ratios of efficiencies on data and simulation are shown for the endcap and forward detector region for all ATLAS muon identification algorithms and various of its combinations.

5.6.3 Segment Tagged or Combined Muons

Combining segment tagger and combined algorithms leads in addition to highest efficiencies also to the best agreement of data and simulation, as the lower rows of plots in Figure 5.10 and 5.11 show. A particularly excellent agreement of data and Monte Carlo simulation on a per-mill-level for all detector regions is achieved when combining MuTagIMO and Muid Combined. Also the combination of MuGirl and Muid Combined reaches on average a per-mill level agreement. The MuTag - Staco Combined combination suffers particularly in the forward region, since MuTag is not operating at $|\eta| > 2$. But also in the remaining detector regions, the data - MC agreement in the threshold curves is not excellent and deviations of several 10 % are observed for the lower p_{T} bins. However, on average also the algorithm combination of the Staco family shows a good agreement between data and simulated efficiencies, reaching a one percent level.

5.7 Comparison to High Momentum Muons

As mentioned in the introduction 5.2 the Tag-and-Probe efficiency measurement can also be performed using muons from Z-boson decays. These muons carry significantly larger momenta, due to the approximately 30 times larger mass of the Z-boson compared to the J/ψ. The very clean two muon final state with hardly any backgrounds left at the given invariant mass scale allows for a precise measurement of the plateau region of the muon reconstruction algorithms. Once reached, the efficiency plateaus are expected to be invariant of the transverse muon momentum. Hence, one would expect to find the same plateau efficiencies using the J/ψ or the Z-boson resonance. Table 5.2 compares the results of this chapter with a measurement performed in the *Muon Combined Performance* group of ATLAS using a Tag-and-Probe technique on the Z-boson resonance [46]. Although the efficiencies of the individual algorithms agree all within the errors, a 1.2 % discrepancy for the combined algorithms can be noted. This discrepancy can be understood considering the respective physical event topologies. Since these high momentum muons are the remnants of highly boosted J/ψ's the opening angle between the decay products is very small and hence identifying both muons individually is more difficult, the efficiency decreases. These efficiency losses however can be recuperated using the segment taggers which do not require independent tracks in the MS. Consequently, the efficiencies of the combination of segment tagger and combined algorithm measured on J/ψ and Z-boson sample agree better. The errors on the efficiencies measured on the Z-boson sample are statistical.
To compare the scaling factors we fit a horizontal line through the two p_{T}-bins $[12; 15]$ and $[15, 20]$ GeV of the scaling factor integrated over all η. This yields numbers corresponding to the scale factors quoted in [46]. However, highly boosted J/ψ's producing muons with $p_{\mathrm{T}} > 12$ GeV are very rare in simulation. The uncertainty on the scaling factors from J/ψ's is hence large. Table 5.3 lists the scaling factors obtained from the J/ψ and Z-boson measurements. The errors on the scaling factors of the Z-boson sample are again of statistical nature. For the scaling factors from J/ψ, the statistical errors are given by the fit, taking statistical uncertainties of the fitted points into account. Scaling factors

for the Muid algorithm agree well within the errors while some deviation of the order of one percent is seen for the Staco algorithms.

	J/ψ (for muon $p_{\mathrm{T}} > 12$ GeV)	Z
Muid Combined	$94.6\,^{+0.6}_{-0.7}\,(\mathrm{stat.}) \pm 1.1\,(\mathrm{sys.})$	95.8 ± 0.1
Staco Combined	$91.6\,^{+0.8}_{-0.9}\,(\mathrm{stat.}) \pm 1.7\,(\mathrm{sys.})$	92.8 ± 0.2
MuTagIMO + MuidCombined	$98.7\,^{+0.3}_{-0.4}\,(\mathrm{stat.}) \pm 0.8\,(\mathrm{sys.})$	98.0 ± 0.1
MuTag + Staco Combined	$97.2\,^{+0.5}_{-0.6}\,(\mathrm{stat.}) \pm 1.0\,(\mathrm{sys.})$	97.0 ± 0.1

Table 5.2: Muon reconstruction efficiencies from Tag-and-Probe measurements on J/ψ's and Z's are shown for selected combined and combined + segment tagged algorithms. All values are given in %. The errors on the efficiencies obtained from the Z sample are purely statistical.

	J/ψ (for muon $p_{\mathrm{T}} > 12$ GeV)	Z
Muid Combined	0.999 ± 0.005	0.995 ± 0.002
Staco Combined	0.969 ± 0.008	0.989 ± 0.003
MuTagIMO + MuidCombined	1.001 ± 0.003	1.001 ± 0.002
MuTag + Staco Combined	0.985 ± 0.004	1.003 ± 0.002

Table 5.3: The ratio of data and Monte Carlo efficiencies from Tag-and-Probe measurements on J/ψ's and Z's is shown for selected combined and combined + segment tagged algorithms.

5.8 Conclusion

The first $18.1\,\mathrm{pb}^{-1}$ of data reprocessed in November 2010 with Athena release 16 show already a very high performant muon reconstruction and identification chain, considering the early stage of the experiment. We measured turn-on curves and the efficiency plateaus of all available ATLAS muon algorithms, as well as various of their combinations. Efficiencies from data were compared to the ones from corresponding Monte Carlo simulations. While the efficiency plateaus agree well, partially even up to a per-mill-level, deviation up to many 10 % were found in the turn-on curves at low muon momenta. The results were subsequently compared to an independent Tag-and-Probe measurement using the Z-boson resonance, revealing a particularly good agreement for the combination of combined algorithms and segment taggers.
Our studies confirm the expectations that the segment taggers are the most efficient

muon identification algorithms and essential to identify low momentum muons. We can also conclude that the algorithms of the Muid family are in general higher efficient than the corresponding algorithms of the Staco family.

CHAPTER 6

W^+W^- Cross Section Measurement

Up to this point we discussed the essential development and performance of software to reconstruct and identify muons in the recorded first ATLAS data. In this chapter we apply the developed expertise and utilize the results of the previous chapters to perform a physics analysis.
As has been discussed in Chapter 1 the measurement of the production of W-pairs, i.e. W^+W^- events presents an important test of the Standard Model and its non-abelian structure of the weak force. Based on our results in the previous chapters, we choose to measure the Standard Model W-pair production, with the two W-bosons decaying into $\mu^+\nu_\mu$ and $\mu^-\bar{\nu}_\mu$. Besides the importance for the Standard Model validation, a precise measurement of the W^+W^- cross section is also essential for Higgs boson searches, one of the main goals of the LHC and the ATLAS collaboration, as has been discussed in chapters 1 and 2. One of the most promising channels, with a distinctive event topology as well as a comparatively large production cross section is the decay of a SM Higgs boson into W^+W^- which further decay leptonically. For Higgs boson masses larger than 135 GeV, the decay into a pair of W-bosons is the dominant Higgs boson decay channel [66]. In the corresponding Higgs boson searches, the production of W^+W^- events in the Standard Model represents the leading background, which is non resonant and irreducible. This background needs to be controlled and understood and a precise measurement of its production cross section is thus essential.
The W^+W^- production cross section has already been determined in an initial measurement performed by the ATLAS Collaboration [47]. In the analysis presented in this chapter, we will use twice as much data and enhance the signal selection with an improved choice of muon identification algorithms.

After a brief description of the method we use to extract the cross section, we define our dataset and select the corresponding simulated signal and the relevant simulated backgrounds. The event selection and the following cut-flow are detailed in Section 6.4. To reduce the reliance on simulation in our measurement, we use a data-driven technique to scale the MC backgrounds to data. This is explained in 6.5. The systematic uncertainties are discussed subsequently in 6.6. We then present our results on the W^+W^- cross section in 6.7. Section 6.8 compares our findings with the already existing measurements performed at the LHC, while 6.9 gives an outlook on the Standard Model Higgs boson.

6.1 Determine the Cross Section

We chose a cut-and-count analysis to extract the cross section, where after the selection the number of background events is subtracted from the observed data events. The yield is divided by the geometrical acceptance and efficiency of the selection as well as the luminosity of the selected dataset, i.e.

$$\sigma = \frac{N_{\text{data}} - N_{\text{bkg}}}{\epsilon\, \mathcal{A}\, \mathcal{L}} \quad . \tag{6.1}$$

Since we restrict our signal selection to the two muon final state, we have to scale our result by the corresponding branching fraction of $W^+W^- \to \mu^+\mu^-\nu_\mu\bar{\nu}_\mu$ to obtain the full W^+W^- production cross section.

6.2 Selected Dataset

We select all data events recorded with Athena release 16 in 2011 that were triggered by at least one single muon trigger [1]. In addition, we require that at least 90 % of all sub-detector systems were operational and both magnet systems were running at nominal current [2]. These requirements hold for the very main part of the data recorded between the 22nd of March and the 22nd of August and correspond to an integrated luminosity of $\mathcal{L} = (2052.49 \pm 75.94)\ \text{pb}^{-1}$. The Athena release changed after the 22nd of August 2011. Data reconstructed with different Athena releases can not consistently be combined, which determines the size of our dataset.

6.3 Simulated Signal and Background Processes

To determine the cross section we need to know the number of background events that will eventually remain after the final selection. It is hence important to model all relevant background processes. Additionally, it is necessary to simulate the signal processes to determine the acceptance corrections for the cross section. This section focusses on the selected simulated physics processes, while the corresponding ATLAS samples are listed, together with their cross sections in Appendix E.3.

Monte Carlo samples are usually produced before all relevant information of the recorded data that it should model is precisely known, as for example the position of the primary vertex or the observed number of pile-up events. Consequently, it is necessary to reweight and scale key quantities of the simulated sample to the recorded data. One essential

[1] The exact trigger requirements on the selected muons will be discussed in Section 6.4.

[2] The ATLAS sub-detector systems were on average to $> 98\,\%$ operational, as detailed in Table 2.2.

quantity is the pile-up which needs to be reweighted for all Monte Carlo sets to match the given data. A common tool of the ATLAS collaboration was used to reweight the average number of pile-up interactions in the used MC samples to the ones found in the selected dataset [3].
The trigger as well as the reconstruction and identification efficiencies of the muons selected in our analysis are an essential ingredient in the extraction of the cross section and hence need to be precisely modeled as well. The Tag-and-Probe method on data is commonly used to determine the scaling factors for these efficiencies, as has been discussed in Chapter 5.

In our analysis of the inclusive two muon final state, we do not distinguish between W-bosons decaying into muons and W-bosons decaying into τ's which subsequently decay into a muon and the corresponding neutrinos. We therefore include MC samples with τ's in the final states. A fraction of $(17.39 \pm 0.04)\,\%$ [1] of the τ's will decay into a muon and hence be included in our selection. However, about half of the generated samples are inclusive lepton samples and hence also include the corresponding electron final state. For consistency, we add therefore the electron final states to the samples that are produced for the individual lepton flavors. However, the probability of an electron to fake a muon that passes the full selection is negligible ($< 10^{-5}$) and hence these samples do not lead to any contribution in our measurement.

6.3.1 Monte Carlo Signal

Figure 1.6 in Chapter 1 already showed the Standard Model W^+W^- production processes. The dominant process is $q\bar{q} \rightarrow W^+W^-$, which is modeled using next-to-leading order matrix element calculations. Less than $3\,\%$ of all W-pairs are produced via gluon fusion. The simulated processes are summarized with the corresponding cross sections in Table 6.1. More details on the individual processes and samples are given in Appendix E.3.

simulated processes and cross sections [pb]

$q\,\bar{q}$	$\rightarrow$	$W^+\,W^-$	$\rightarrow$	$l^+\,l'^-\,\nu_l\,\bar{\nu}_{l'}$	4.19
$g\,g$	$\rightarrow$	$W^+\,W^-$	$\rightarrow$	$l^+\,l'^-\,\nu_l\,\bar{\nu}_{l'}$	0.11

Table 6.1: The simulated signal processes are shown where $l, l' \in \{e, \mu, \tau\}$. The final state with two electrons is not included. The given cross sections are at next-to-leading order.

6.3.2 Monte Carlo Backgrounds

The relevant backgrounds can be divided in four groups. We list them in the order of their contributions after the full event selection:

[3] We use the software package `PileupReweighting-00-00-16`, available to ATLAS collaboration members.

- **top**: One of the major backgrounds that remains after the requirements on the missing transverse energy are top events. We include $t\bar{t}$ production as well as single top samples produced in the s- and t-channel diagrams. Since the top quark decays into a W-boson and a b-quark which further decays to create a hadronic jet in the event, applying a jet veto rejects a large fraction of top events. However events in which the associated jets escape the detector or have transverse momenta smaller than 25 GeV will end up in the final W^+W^- signal selection.

- **W+jets**: Events in which a produced W-boson decays in its muon channel and a QCD jet either contains a muon from e.g. a b decay, or else produces a muon through e.g. a π or K meson decay contribute to the background as well. These events have intrinsic missing transverse energy from the W-boson decay. The large production rate of $W^\pm + \text{jets} \rightarrow \mu^\pm \overset{(-)}{\nu}_\mu + X$ compensates for the very small probability of a jet to be misidentified as an isolated muon.

- **Z+jets**: Selecting events with two oppositely charged muons selects Drell-Yan processes whose production cross sections are many orders of magnitude larger than the W^+W^- cross section, see Section 1.4.3. However, due to the absence of neutrinos in the final state, no missing transverse energy is created in these events. Consequently, a missing energy requirement, as well as an invariant mass cut to remove Z-bosons reduce this background significantly. Nevertheless, the presence of mis-measured jets in Drell-Yan events can be an independent source of missing transverse energy and the large production cross section still leads to a background contribution even after all selection requirements.

- **WZ/ZZ/Wγ**: The final and smallest contribution to the W^+W^- backgrounds is coming from additional di-boson productions. An event with the process $W^\pm Z \rightarrow \mu^\pm \overset{(-)}{\nu}_\mu \mu^+\mu^-$ in which one of the muons of the decaying Z-bosons is missed by the detector can mimic a W^+W^- event. Cases in which two out of the four muons in the decay of two Z-bosons are missed by the detector are very rare but nevertheless taken into account. Likewise are $W\gamma$ events, where the photon is in extremely rare cases misidentified as a muon. The events where a Z-boson is produced with an associated photon are already included in the Z+jets samples.

Table 6.2 summarizes the simulated background processes, while more details on the generations of the individual processes are given in Appendix E.3.

simulated processes and cross sections [pb]

top			
$t\,\bar{t}$	$\rightarrow$	$l'^{\pm}\ \overset{(-)}{\nu}{}'_l\ +X$	91.42
$W^{\pm}\ \overset{(-)}{t}$	$\rightarrow$	X	15.60
$\overset{(-)}{t}$	$\rightarrow$	$l'^{\pm}\ \overset{(-)}{\nu}{}'_l\ +X$ (t-channel)	13.86
$\overset{(-)}{t}$	$\rightarrow$	$l'^{\pm}\ \overset{(-)}{\nu}{}'_l\ +X$ (s-channel)	1.00

WZ/ZZ/Wγ			
$W^{\pm}\,\gamma$	$\rightarrow$	$l^{\pm}\ \overset{(-)}{\nu}_l\ \gamma$	53.76
$W^{\pm}\,Z$	$\rightarrow$	$l'^{\pm}\ \overset{(-)}{\nu}{}'_l\ q\,\bar{q}$	2.62
$W^{\pm}\,Z$	$\rightarrow$	$q'\,\bar{q}\,l'^{+}\,l'^{-}$	0.78
$W^{\pm}\,Z$	$\rightarrow$	$l'^{\pm}\ \overset{(-)}{\nu}{}'_l\ l''^{+}\,l''^{-}$	0.25
$Z\,Z$	$\rightarrow$	$l'^{+}\,l'^{-}\ q\,\bar{q}$	0.80
$Z\,Z$	$\rightarrow$	$l'^{+}\,l'^{-}\ \nu_{l''}\,\bar{\nu}_{l''}$	0.23
$Z\,Z$	$\rightarrow$	$l'^{+}\,l'^{-}\ l''^{+}\,l''^{-}$	0.06

Z+jets			
$Z+$Np0	$\rightarrow$	$l^{+}\,l^{-}+$Np0	1811.56
$Z+$Np1	$\rightarrow$	$l^{+}\,l^{-}+$Np1	388.86
$Z+$Np2	$\rightarrow$	$l^{+}\,l^{-}+$Np2	151.60
$Z+$Np3	$\rightarrow$	$l^{+}\,l^{-}+$Np3	38.34
$Z+$Np4	$\rightarrow$	$l^{+}\,l^{-}+$Np4	9.20
$Z+$Np5	$\rightarrow$	$l^{+}\,l^{-}+$Np5	2.49

W+jets			
$W^{\pm}+$Np0	$\rightarrow$	$l^{\pm}\ \overset{(-)}{\nu}_l\ +$Np0	16605.84
$W^{\pm}+$Np1	$\rightarrow$	$l^{\pm}\ \overset{(-)}{\nu}_l\ +$Np1	3128.88
$W^{\pm}+$Np2	$\rightarrow$	$l^{\pm}\ \overset{(-)}{\nu}_l\ +$Np2	907.21
$W^{\pm}+$Np3	$\rightarrow$	$l^{\pm}\ \overset{(-)}{\nu}_l\ +$Np3	244.07
$W^{\pm}+$Np4	$\rightarrow$	$l^{\pm}\ \overset{(-)}{\nu}_l\ +$Np4	61.67
$W^{\pm}+$Np5	$\rightarrow$	$l^{\pm}\ \overset{(-)}{\nu}_l\ +$Np5	16.75

Table 6.2: The simulated background processes are shown schematically, with $l \in \{\mu, \tau\}$ and $l', l'' \in \{e, \mu, \tau\}$. X denotes all additional particles in the possible final states. NpX stands for the generated additional number of X partons in the event.

6.4 Event Selection

The W^+W^- event selection begins with the choice of the muon identification algorithm(s). While the official ATLAS analysis selects Staco Combined muons with $p_{\mathrm{T}} \geq 25$ GeV for one and $p_{\mathrm{T}} \geq 20$ GeV for the other muon respectively, we choose to use the Muid muon collection, requiring one Muid Combined and one MuTagIMO or Muid Combined muon. Following the results of Chapter 5, the efficiency of identifying the two muons in our signal increases by about 10 %, compared to the identification efficiency selecting two Staco Combined muons. We further increase our signal selection efficiency by lowering the transverse momentum requirement to 20 and 15 GeV respectively.
The additional preselection criteria, the necessary event cleaning as well as the full cut-flow are discussed in the following subsections.

6.4.1 Preselection

Besides the selection discussed in Section 6.2 the following preselections are made:

- **trigger**: We select events that were triggered by the lowest threshold, unprescaled trigger in our dataset. The main unprescaled selected trigger is `EF_mu18_MG` with a threshold of $p_{\mathrm{T}} \geq 18$ GeV and a pseudorapidity coverage of $|\eta| \leq 2.4$. To enhance the overall trigger efficiency, events triggered by `EF_mu40_MSonly_barrel` are added. This trigger is solely based on measurements in the Muon Spectrometer and in addition restricted to $|\eta| < 1.05$ with a transverse momentum threshold of $p_{\mathrm{T}} >$ 40 GeV [4].

- **overlap removal**: In rare cases a muon traversing the detector radiates off a photon that fakes an electron cluster in the calorimeters. The muon can hence be misidentified as an electron. To prevent this, electrons with $p_{\mathrm{T}} > 20$ GeV within a cone of $\Delta R < 0.1$ around the muon are removed from the event.

- **invariant mass**: Since no Drell-Yan processes with invariant masses below 10 GeV are simulated we apply a cut on the invariant mass of the two muons and require $m_{\mathrm{inv.}} > 15$ GeV.

6.4.2 Event Cleaning

The following requirements remove problematic events:

- **LAr hole**: For a share of the recorded data a small part of the LAr calorimeter was not operational leading to a hole in the acceptance [81]. Events with jets with transverse momenta larger than 25 GeV that fall in the close vicinity of the LAr

[4] Due to the increased instantaneous luminosity the triggers had to be slightly modified for the data recorded in August. While the thresholds and coverage stayed the same, a three instead of a two station coincidence was required for this part of the data. The corresponding triggers are labeled `EF_mu18_MG_medium` and `EF_mu40_MSonly_barrel_medium`.

hole are rejected both, in data as well as in the Monte Carlo samples, in which the acceptance hole is simulated.

- **LAr flag**: In rare cases noise bursts in the LAr calorimeters occur that make a reliable $E_{\mathrm{T}}^{\mathrm{miss}}$ measurement impossible. These data events are flagged and removed from the selection.

- **$E_{\mathrm{T}}^{\mathrm{miss}}$ cleaning**: Not all reconstructed jets always result from physics processes in the corresponding event. Hardware problems, cosmic-ray showers or background events to the LHC beams can create jets. Common ATLAS tools are in place to identify these jets as *bad* jets. Events in which a jet with $p_{\mathrm{T}} > 20$ GeV is identified to be a bad jet and does not overlap with a selected muon in a ΔR cone of 0.3, are rejected [81]. This cleaning process is only relevant and performed on data.

6.4.3 Full Selection

After the preselection and event cleaning, we apply various cuts to select W^+W^- candidates. The requirements are grouped into seven steps which are detailed and illustrated by a selection of corresponding distributions.

1. **Muons**: We select events with exactly 2 muons. The requirements on the muons are:

    - **algorithms**: One muon needs to be identified by the Muid Combined algorithm. The second muon needs to be identified by the Muid Combined or the MuTagIMO algorithm. See 3.6.2, 3.6.3 as well as Chapter 4 for details on these identification algorithms.
    - **transverse momentum**: Both muons are required to have $p_{\mathrm{T}} > 15$ GeV.
    - **pseudorapidity**: The muons are required to lie within $|\eta| < 2.4$.
    - **isolation**: To reduce the number of background events, the muons are required to be isolated. The sum of all ID transverse track momenta in a ΔR cone of 0.2 around the muon trajectory is required to be smaller than 10 % of the transverse muon momentum. The deposited transverse energies in the calorimeters in a ΔR cone of 0.2 around the traversing muon track are required to be smaller than 15 % of the transverse muon momentum.
    - **impact parameter**: The longitudinal impact parameter of each muon is required to be smaller than 10 mm. For the transverse impact parameter, we require $d_0/\sigma_{d_0} < 10$.
    - **ID track requirements**: Various requirements on the ID tracks of the selected muons are applied which are detailed in Appendix C.

    Figure 6.1 shows the transverse momentum spectra of the selected leading and subleading muons. We observe an excellent agreement between data and simulation at the per-mill level.

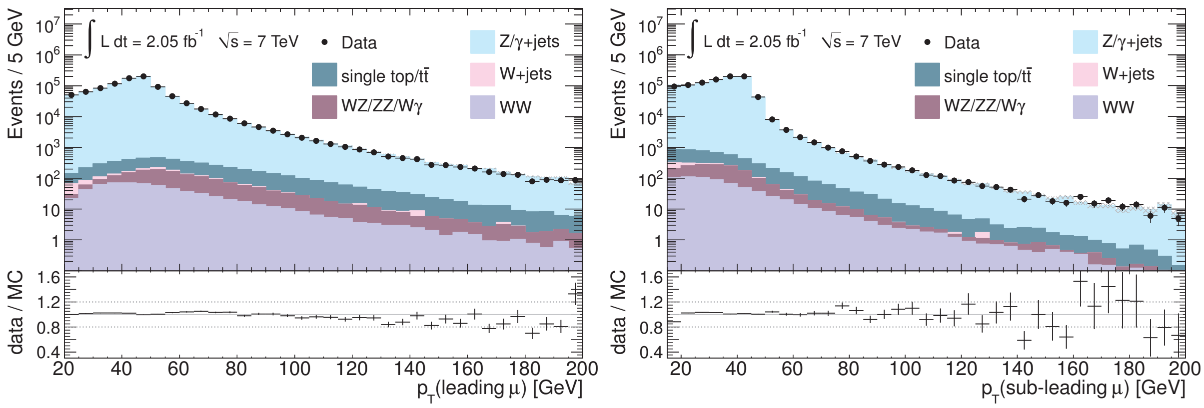

(a) leading muon (b) sub-leading muon

Figure 6.1: The transverse momentum spectra of the selected leading and sub-leading muons are shown (step 1 in the cut-flow). The errors are statistical.

2. **Trigger Matching**: To prevent trigger biases, at least one of the two selected muons needs to be successfully matched to the muon trigger that had the event recorded. The matching is performed using a ΔR cone of 0.1. Since the threshold of the main used muon trigger, `EF_mu18_MG(_medium)` is at $p_T = 18$ GeV we require the matched muon to have a transverse momentum of at least 20 GeV to ensure that the trigger already reached its plateau efficiency. This reduces the systematic uncertainties. For the events triggered by `EF_mu40_MSonly_barrel(_medium)` with a threshold of $p_T = 40$ GeV we require the corresponding matched muon to have a transverse momentum larger than 42 GeV.

3. **Opposite Charge**: The two muons are required to have opposite charge.

4. ***Z* Mass Veto**: To reject Z-boson events a cut on the invariant mass distribution of the two selected muons is applied and events with $|91.1876 - m_{\text{inv.}}|[\text{GeV}] < 15$ GeV are rejected.
   Figure 6.2 shows the invariant mass distribution on a logarithmic scale after requiring the muons to have opposite charge. The Z-boson events are clearly visible in the peak at around 90 GeV.

5. **Missing Transverse Energy**: Up to this point the selection is dominated by Drell-Yan processes. A cut on the missing transverse energy substantially reduces this background. We require $E_{\text{T,rel.}}^{\text{miss}} > 45$ GeV. Details on the calculation of the missing transverse energy are discussed in Section 3.5.
   Figure 6.3 shows the distribution of the relative transverse missing energy before the cut on it is applied. We observe a very good agreement between data and simulation over the entire spectrum with the average agreement being better than 6 %.

6. **Jet Veto**: Top quark events are rejected by applying a jet veto. All events with at least one jet are rejected. A jet is defined as:

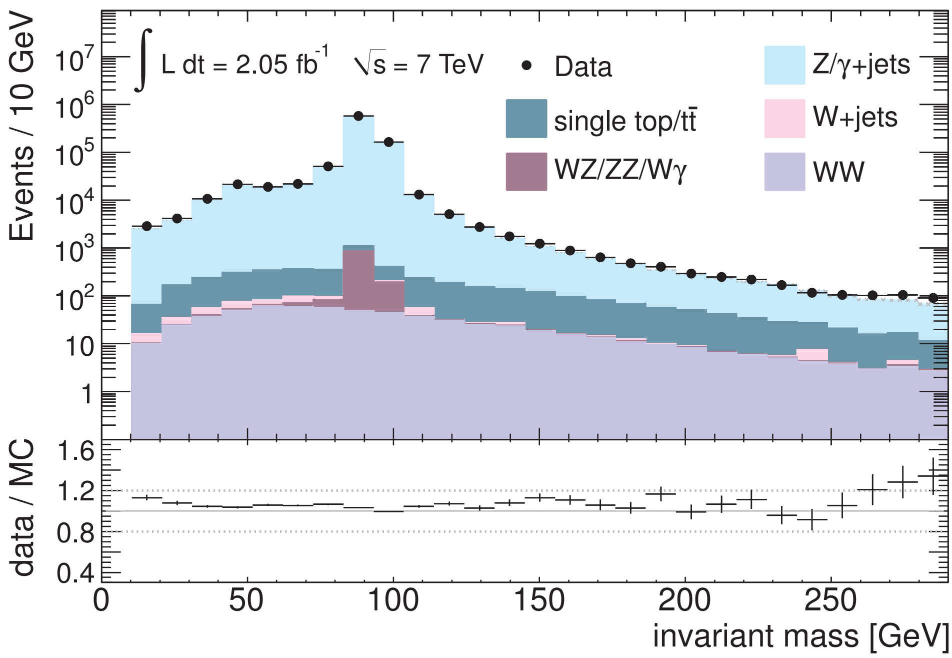

Figure 6.2: The invariant transverse mass of the two selected muons with opposite charge is shown (step 3 in the cut-flow). The errors are statistical.

- being reconstructed with an anti-k_T jet algorithm using a cone of 0.4, see Section 3.4, [82].
- having a transverse momentum of at least 25 GeV.
- lying within the pseudorapidity range $|\eta| < 4.5$.

Figure 6.4 shows the number of jets in the events remaining after cut-flow step 5. We see that the spectrum is entirely dominated by top quark events once there is at least one jet reconstructed in the event. We hence only select the 0-jet bin.

7. **Dilepton Transverse Momentum**: The two muon system is required to satisfy $p_T^{\mu\mu} > 30$ GeV. Figure 6.5 motivates this cut. The majority of the remaining Drell-Yan background can be rejected without cutting significantly in the signal acceptance. Data and simulation agree well within their statistical uncertainties.

For each step, the number of selected events in data as well as the corresponding normalized numbers of the sum of the Monte Carlo background samples, the Monte Carlo signal and the sum of Monte Carlo signal and backgrounds are listed in Table 6.3. The difference between the number of selected events in data and Monte Carlo events in the cut-flow steps 1 to 4 of up to 5.7 % can be explained by the systematic uncertainties of the MC samples that cover the observed discrepancy. Table 6.4 lists the event yields for the individual backgrounds.

Figure 6.7 shows some selected distributions after the full cut-flow. The leading and sub-leading muon transverse momenta, the opening angle $\Delta\phi$ between the two selected

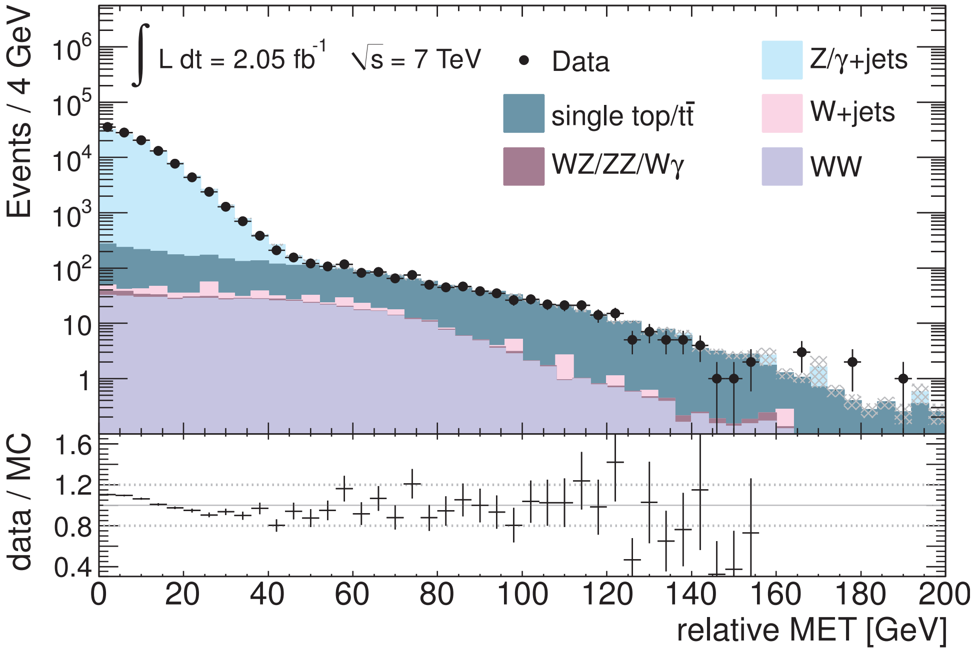

Figure 6.3: The $E_{\mathrm{T,rel.}}^{\mathrm{miss}}$ distribution is shown after the Z-boson mass veto is applied (step 4 in the cut-flow). The errors are statistical.

muons as well as the missing transverse energy are shown. In addition, Figures 6.7(e) and (f) combine the measured muon momenta and the reconstructed $E_{\mathrm{T}}^{\mathrm{miss}}$ to the transverse mass m_{T} and the total transverse momentum of the W^+W^- candidates $p_{\mathrm{T}}^{\mathrm{tot}}$. They are defined as

$$m_{\mathrm{T}} = \sqrt{(E_{\mathrm{T}}^{\mu\mu} + E_{\mathrm{T}}^{\mathrm{miss}})^2 - \left(p_x^{\mu\mu} + E_{\mathrm{T},x}^{\mathrm{miss}}\right)^2 - \left(p_y^{\mu\mu} + E_{\mathrm{T},y}^{\mathrm{miss}}\right)^2} \quad (6.2)$$

$$p_{\mathrm{T}}^{\mathrm{tot}} = \sqrt{\left(p_x^{\mu_1} + p_x^{\mu_2} + E_{\mathrm{T},x}^{\mathrm{miss}}\right)^2 + \left(p_y^{\mu_1} + p_y^{\mu_2} + E_{\mathrm{T},y}^{\mathrm{miss}}\right)^2} \quad . \quad (6.3)$$

Data and Monte Carlo simulations agree well within the statistical uncertainties, which are shown for data as well as for the simulated samples. The Monte Carlo statistics of the W+jets processes that remain after the full selection are very limited, leading to large statistical uncertainties on the contribution of this background.
Figures 6.7(a) and (b) show that the lowered transverse momentum threshold, particularly on the sub-leading muon increases the selected signal considerably. We observe, that the distribution of the opening angle between the two muons is rather flat and only falls off for very large angles. Hence, almost no events with the two muons being back-to-back are observed, which is expected since the neutrinos in the W-boson decays also carry away a considerable part of the total momentum.
Figure 6.6 shows one of the W^+W^- candidate events [5], where the μ^+ with $p_{\mathrm{T}} = 34.6$ GeV

[5] The corresponding ATLAS event number is 86117193 in run 187014. The event display was created using the ATLAS VP1 software [49].

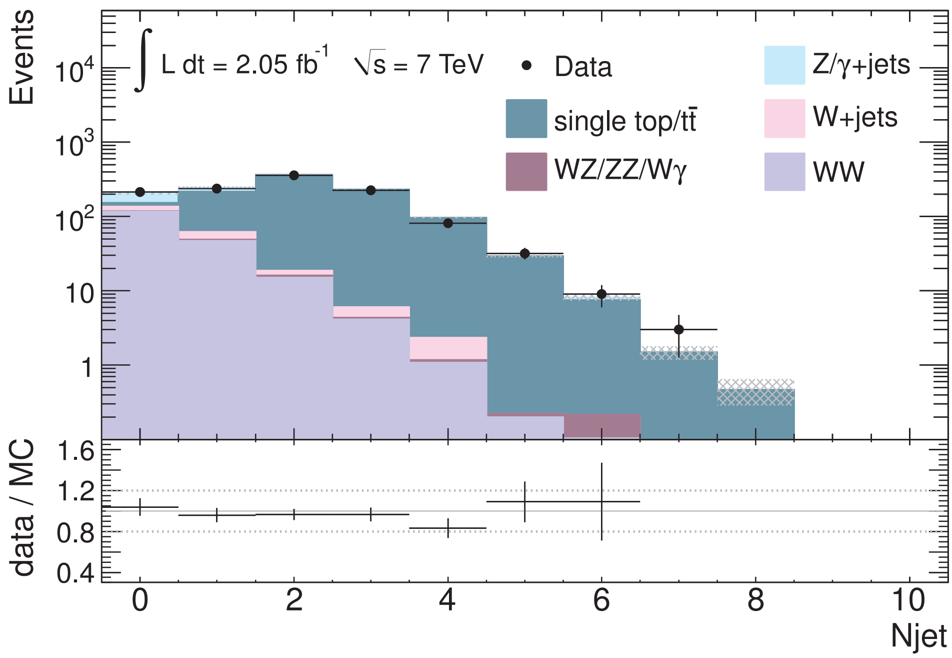

Figure 6.4: The number of jets in the events remaining after the requirement on the missing transverse energy is shown (step 5 in the cut-flow). The errors are statistical.

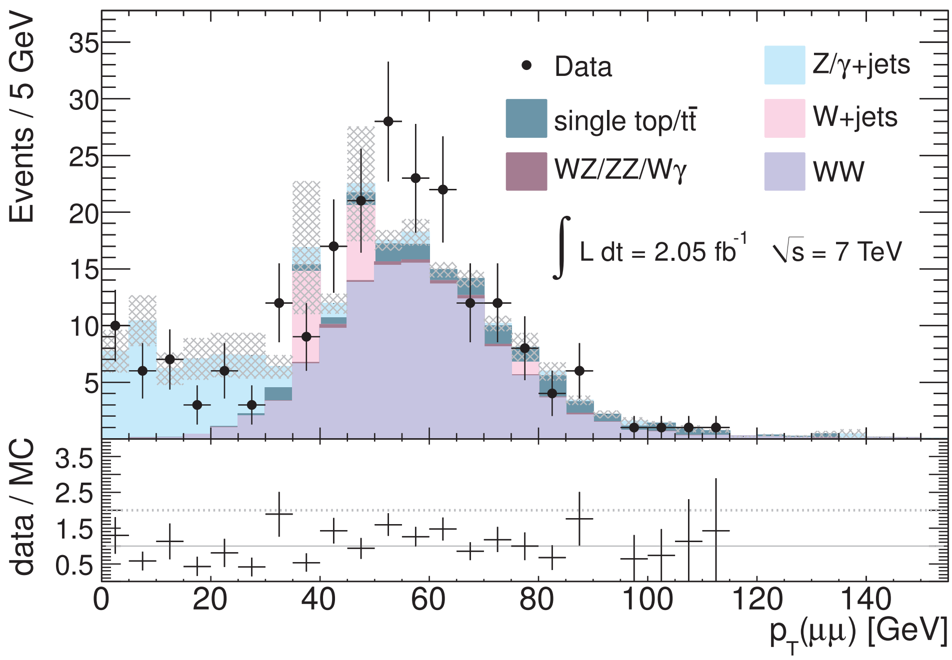

Figure 6.5: The transverse momentum of the two-muon system is shown after the jet-veto (step 6 in the cut-flow). The displayed errors on data as well as on MC are statistical.

cuts	data	Σ_{all} MC	W^+W^-	Σ_{bkg} MC
1.: 2 good muons	938585 ± 968.8	932788 ± 733	670.1 ± 3.9	932118 ± 733
2.: trigger, leading p_{T}	906339 ± 952.0	880488 ± 708	640.5 ± 3.8	879848 ± 708
3.: opposite charge	905829 ± 951.8	880350 ± 707	640.4 ± 3.8	879710 ± 707
4.: Z veto	115007 ± 339.1	108764 ± 254	500.3 ± 3.4	108264 ± 254
5.: $E_{\text{T,rel.}}^{\text{miss}} > 45\ GeV$	1162 ± 34.1	1196.7 ± 13.9	184.9 ± 2.1	1011.7 ± 13.7
6.: Jet veto	214 ± 14.6	206.2 ± 9.5	117.1 ± 1.7	89.1 ± 9.4
7.: $p_T^{\mu\mu} > 30$	179 ± 13.4	160.1 ± 8.3	113.7 ± 1.6	46.4 ± 8.1

Table 6.3: The event counts for the defined steps in the cut-flow are shown for data, the sum of all simulated samples, as well as MC signal and the sum of the MC backgrounds samples. The event yields of the Monte Carlo samples are normalized to the luminosity of the selected dataset. The quoted errors are statistical.

cuts	WZ/ZZ/Wγ	W+jets	Z+jets	top
1.: 2 good muons	1077.3 ± 10.9	232.7 ± 23.5	927546 ± 732	3262.2 ± 14.3
2.: trigger, leading p_{T}	1045.0 ± 10.8	203.5 ± 22.5	875506 ± 707	3093.1 ± 14.0
3.: opposite charge	1024.0 ± 10.8	171.7 ± 20.5	875451 ± 707	3062.5 ± 13.9
4.: Z veto	36.7 ± 1.7	133.5 ± 18.6	105700 ± 253	2393.2 ± 12.2
5.: $E_{\text{T,rel.}}^{\text{miss}} > 45\ GeV$	6.3 ± 0.4	34.5 ± 9.0	97.0 ± 7.0	874.0 ± 7.6
6.: Jet veto	2.6 ± 0.3	15.8 ± 7.7	51.7 ± 5.1	18.9 ± 1.6
7.: $p_T^{\mu\mu} > 30$	2.6 ± 0.3	15.8 ± 7.7	9.5 ± 2.1	18.5 ± 1.6

Table 6.4: The event counts for the defined steps in the cut-flow are shown for the individual MC background samples. The event yields of the Monte Carlo samples are normalized to the luminosity of the selected dataset . The quoted errors are statistical.

is identified by MuidCombined and MuTagIMO [6] while the μ^- with $p_{\text{T}} = 33.2$ GeV and $\eta = 0.1$ falls in the $\eta = 0$ acceptance hole of the ATLAS muon system and is hence missed by the combined algorithm and only identified by MuTagIMO. The invariant mass of the two muons is $m_{\text{T}} = 124.75$ GeV. The missing transverse energy is illustrated with a blue arrow.

We conclude that the chosen requirements lead to a fairly pure selection of W^+W^- events with only minor contributions from background processes. Data and Monte Carlo show in addition a good agreement, which we will however scrutinize further in the subsequent section.

[6] The combined track is colored red.

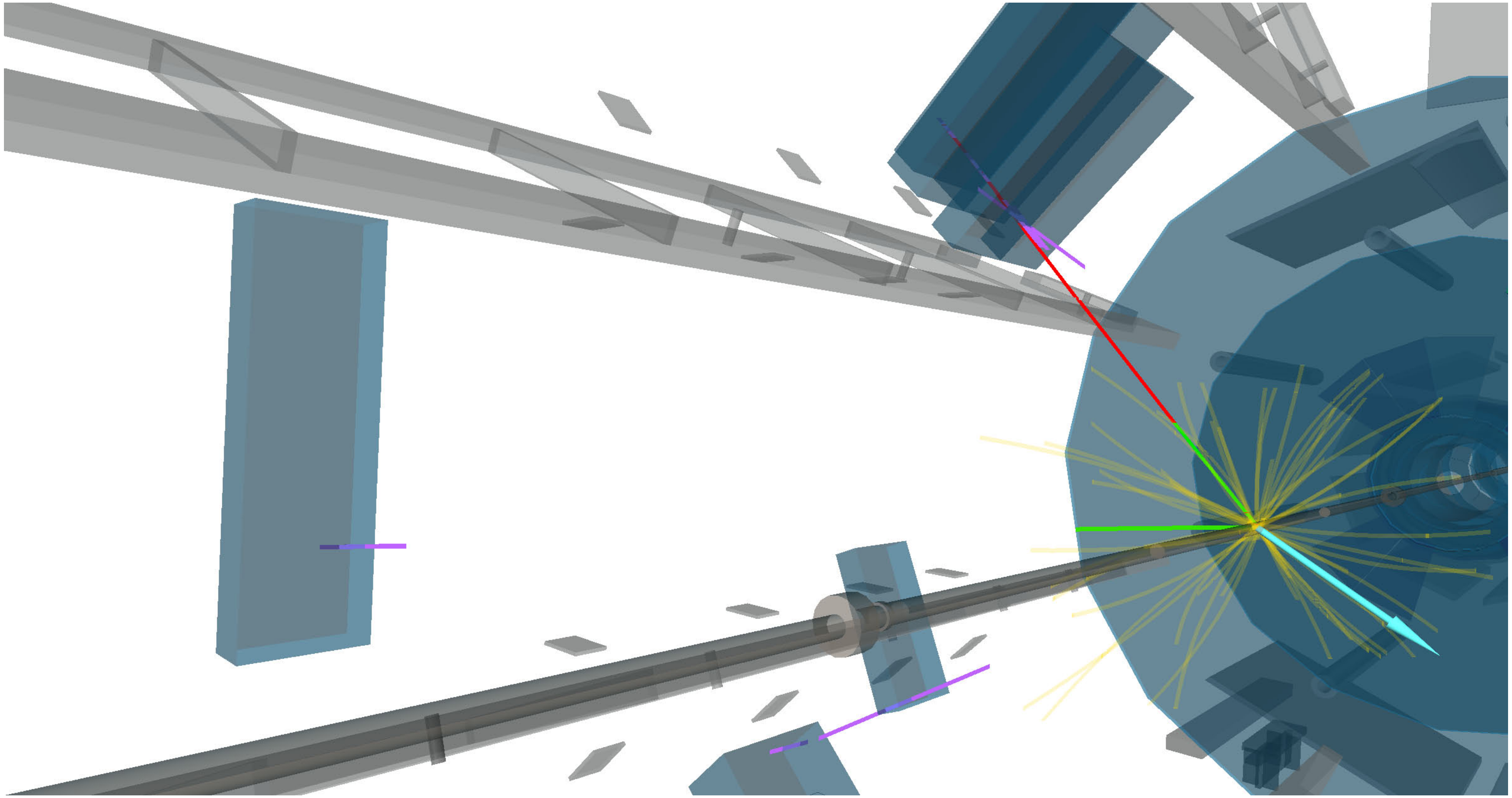

Figure 6.6: Event display of a W^+W^- candidate in ATLAS. The track of the combined muon is depicted in red, the one of the segment tagged muon is depicted in green. The cyan arrow illustrates $E_{\mathrm{T}}^{\mathrm{miss}}$. Inner Detector tracks with $p_{\mathrm{T}} > 1$ GeV are shown in yellow and segments in the muon system are shown in purple.

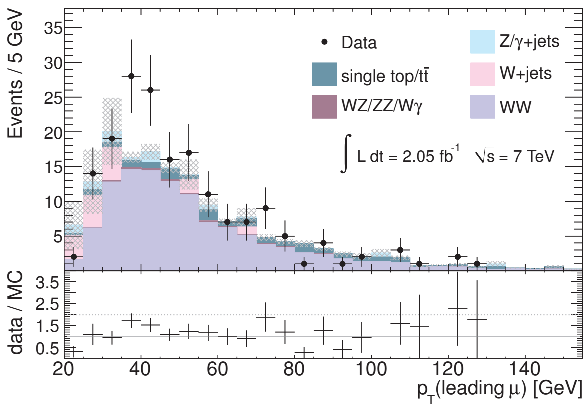

(a) leading muon

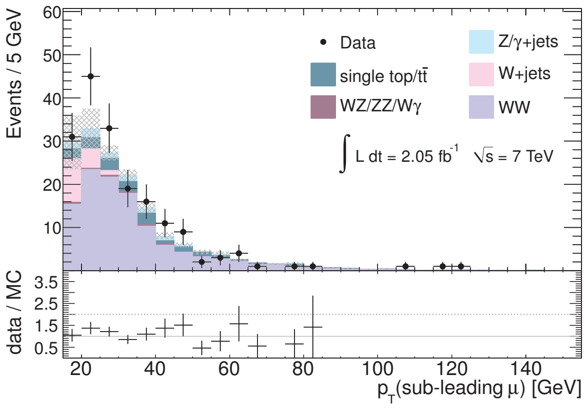

(b) sub-leading muon

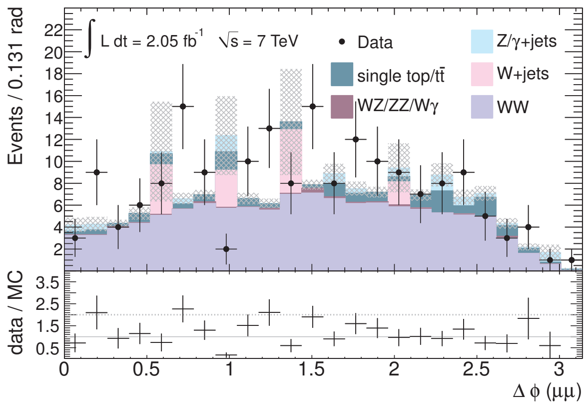

(c) opening angle

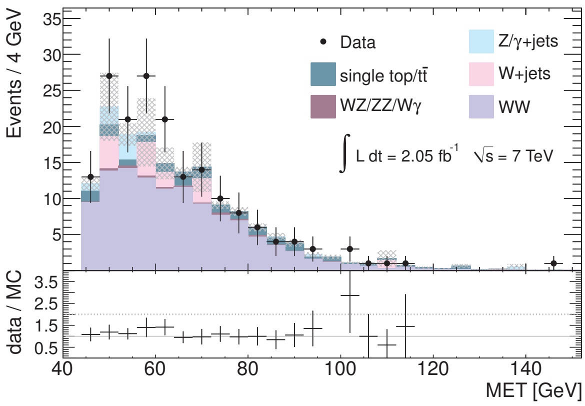

(d) missing transverse energy

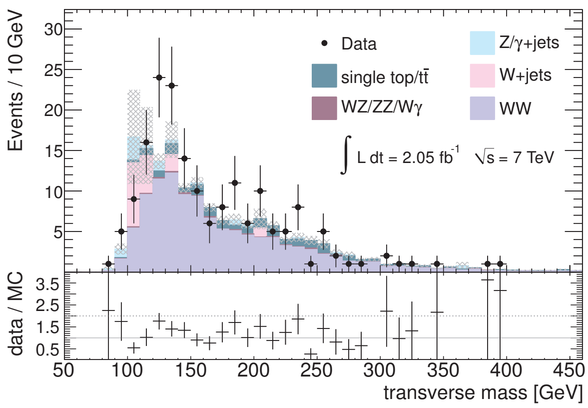

(e) transverse mass

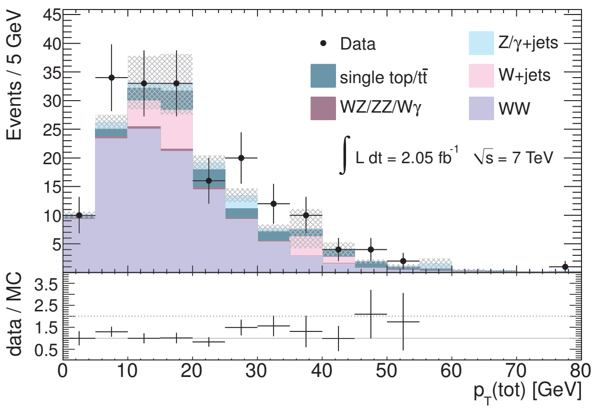

(f) total transverse momentum

Figure 6.7: The transverse momentum spectrum of the leading (a) and sub-leading (b) muon are shown in the first row. The opening angle between the two leptons (c) as well as the $E_{\mathrm{T}}^{\mathrm{miss}}$ (d) are shown in the second row. In the third row, (e) shows the transverse mass distribution of the muons and the $E_{\mathrm{T}}^{\mathrm{miss}}$ while the total transverse momentum defined as the sum of the two muon momenta and the $E_{\mathrm{T}}^{\mathrm{miss}}$ is shown in (f). All distributions are shown after the full selection was applied.

6.5 Data-Driven Background Normalization

The modeling of the different backgrounds that we identified in 6.3.2 has a crucial impact on our cross section measurement as has been briefly discussed in Section 6.1. Since we seek to limit our reliance on the Monte Carlo samples we use a data-driven way to scale the simulated top, Z+jets and W+jets samples to data and estimate the systematic uncertainties using control regions. These regions in phase-space are chosen to enhance one particular background which allows us to compare data to MC for that background. In each control region we calculate the scale factor s_α for the corresponding background α, i.e.

$$s_\alpha := \frac{\text{data}}{\text{MC}} := \frac{N_{\text{data}} - N_{\sum_{\text{bkg}} \text{MC}}}{N_\alpha} = 1 + \frac{N_{\text{data}} - N_{\text{MC}}}{N_\alpha} \tag{6.4}$$

with N_{data} being the number of muon pairs in the control region in data while $N_{\sum_{\text{bkg}} \text{MC}}$ is the number of corresponding muon pairs in the sum of all Monte Carlo samples defined in Section 6.3 but α. N_α is correspondingly the number of muon pairs in the selected background α in the control region. N_{MC} denotes the number of muon pairs in the control region in the sum of all processed Monte Carlo samples, hence $N_{\text{MC}} = N_{\sum_{\text{bkg}} \text{MC}} + N_\alpha$. The error on the scale factor is used as the corresponding systematic uncertainty. The scale factors of the three leading backgrounds will be determined in the subsequent sections. The result is already summarized in Table 6.5.

background	scale factor
top	0.886 ± 0.041
W+jets	1.299 ± 0.159
Z+jets	0.930 ± 0.067

Table 6.5: The scale factors for the identified backgrounds that were measured in the individual control regions are given together with their uncertainties.

6.5.1 Top Background

The top background is estimated using a control region very similar to the final selection. All requirements up to cut-flow step 6 are identical. Instead of a jet-veto we however require at least one b-tagged jet to enhance the top background. We define a b-tagged jet as a jet with transverse momentum larger than 25 GeV that is identified to originate from a *b*-quark [7]. Figure 6.8 shows the transverse mass distribution as well as the number of jets in the control region. The selection is very pure in top events with practically no contributions from other physics processes.

[7] Technically speaking, the SV0 tagger algorithm at the operation point SV0 > 5.85 to identify *b*-jets is used.

Following the method in Equation 6.4 we calculate

$$s_{\text{top}} = 1 + \frac{N_{\text{data}} - N_{\text{MC}}}{N_{\text{top}}} \tag{6.5}$$

with N_{data} being the number of muon pairs in the control region in data, while N_{MC} denotes the number of muon pairs in the control region in the sum of all processed Monte Carlo samples. N_{top} is the corresponding number in only the top MC samples. We find a reasonable data - Monte Carlo agreement of $s_{\text{top}} = 0.886 \pm 0.041$.

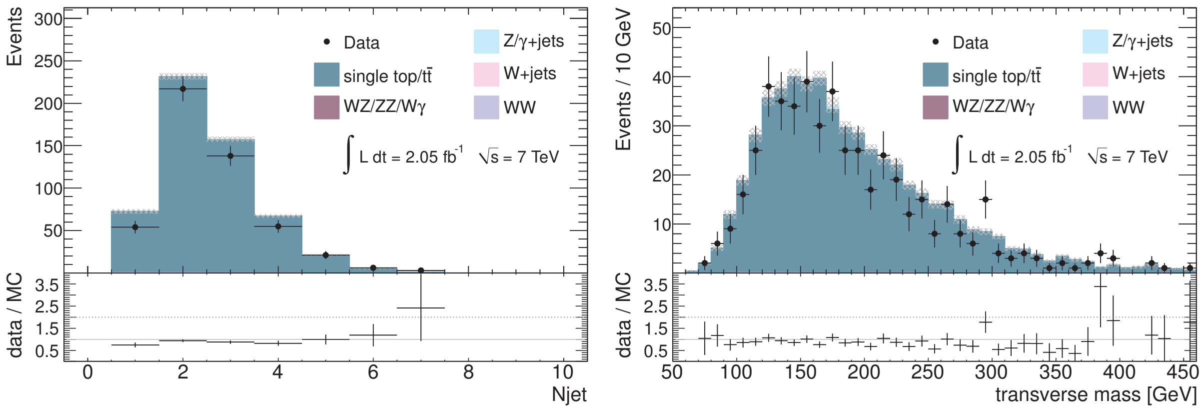

(a) number of jets

(b) transverse mass

Figure 6.8: The number of jets as well as the transverse mass distribution is shown for the top control region before the scaling.

6.5.2 W+jets Background

Defining a control region for the W+jets background is more challenging than for the top background. Again, we follow the in 6.4.3 defined cut-flow up to step 6, however this time loosening the isolation requirements by only requiring one of the two muons to pass the isolation cuts. Contrary to the definition of the top control region, we reject events with b-tagged jets as well as events with more than 1 jet. This reduces strongly the contributions from top processes. Figure 6.9 shows the distributions of transverse mass and missing transverse energy in the control region.

A way to further increase the purity of W+jets events in the control region is to ask for same sign, instead of opposite sign muons. This control region is however likely to select different physics processes where the second muon results from pion or kaon decays and is not directly related to the muon of the W-boson decay. In order to get a realistic estimate of the W+jets background in our cross section measurement, we hence decide to use the scale factor retrieved in the opposite sign W+jets control region, $s_{\text{W+jets}} = 1.299 \pm 0.159$. The scale factors of both control region do however agree within the uncertainty. The scale factor in the same sign control region is found to be $s_{\text{W+jets}}^{\text{same sign}} = 1.254 \pm 0.246$.

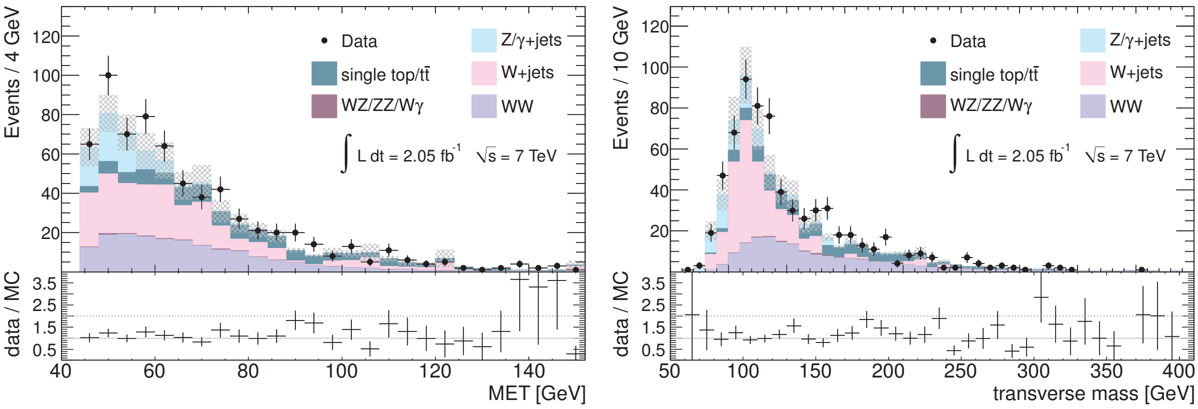

(a) missing transverse energy (b) transverse mass

Figure 6.9: The unscaled distributions of $E_{\mathrm{T}}^{\mathrm{miss}}$ and the transverse mass in the W+jets control region is shown.

6.5.3 Z+jets Background

Defining a control region for the Z-boson background is straight forward. We use the event selection up to step 4 in the cut-flow and then invert the invariant mass cut to select events with invariant masses of the muon pairs within 15 GeV of the Z-boson mass. Afterwards, the $E_{\mathrm{T,rel}}^{\mathrm{miss}}$ requirement as well as the jet-veto are applied as in cut-flow steps 5 and 6. Although the requirement on the missing transverse energy eliminates the bulk of Z-boson and Drell-Yan events, the result is still a control region that is clearly dominated by Z-boson candidates. Figure 6.10 shows the distribution of the opening angle $\Delta\phi$ of the two muons as well as the transverse momentum of the leading muon. The scale factor is calculated to be $s_{\mathrm{Z+jets}} = 0.930 \pm 0.067$.

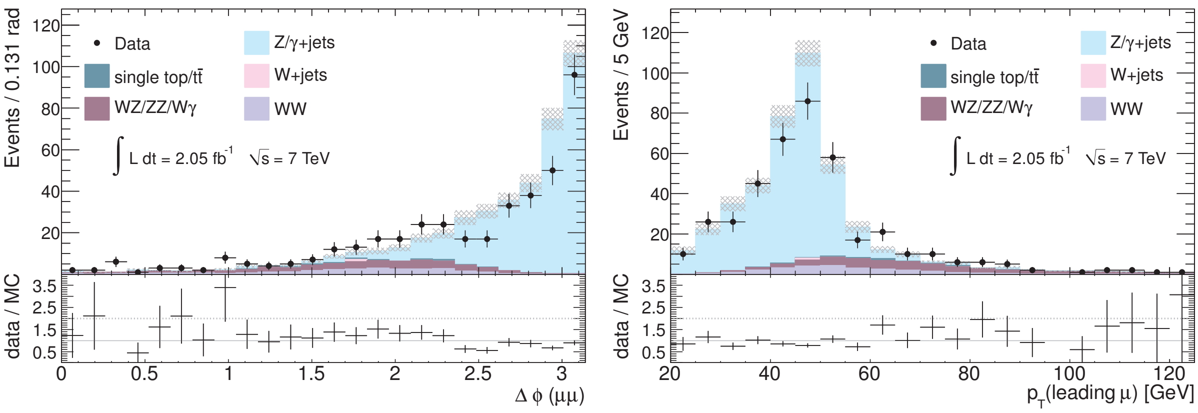

(a) opening angle (b) leading muon

Figure 6.10: The opening angle between the two muons as well as the leading muon p_{T} is shown for the Z+jets control region.

6.5.4 Scaling the Backgrounds

The individual top, W+jets and Z+jets background contributions and their statistical uncertainties are scaled with the corresponding scale factors. The control regions were chosen to mimic as closely as possible the phase-space of the full selection. We hence only scale the yields after the full selection, i.e. after cut-flow step 7, using the scale factors given in Table 6.5. Table 6.6 lists the scaled individual background contributions passing the full selection with their total uncertainty. The error on the individual scaling factors is taken as the systematic uncertainty on the corresponding scaled background yield. The di-boson background is not scaled and the quoted event yield is copied from Table 6.4. Its systematic error will be discussed in the subsequent section.

background	value		stat.		sys.
top	16.4	±	1.4	±	0.8
W+jets	20.5	±	10.0	±	2.5
Z+jets	8.8	±	1.9	±	0.6
WZ/ZZ/Wγ	2.6	±	0.3	±	0.1
Σ_{bkg}MC	48.3	±	10.3	±	2.7

Table 6.6: The scaled number of events passing the full selection is listed for the individual background contributions with statistical and systematic uncertainties. The di-boson background is not scaled.

6.6 Systematic Uncertainties

The systematic uncertainties on the measured cross section are separated into uncertainties from theoretical and experimental sources. The various contributions with their origin are listed below in detail. Table 6.7 summarizes the relative uncertainties of the various identified sources on the cross section.

6.6.1 Theoretical Uncertainties

The theoretical uncertainties on the measured cross section are dominated by the uncertainty on the $W \to \mu$ branching fraction which is known to an accuracy of approximately 1.4 %. Additional signal acceptance uncertainties arise from PDF and scale uncertainties. We identify the following sources of theoretical uncertainties:

- **scale**: The renormalization and factorization scales in the Monte Carlo event generation are each multiplied and divided by a factor two to estimate the effect on the Monte Carlo signal acceptance [56].

theoretical source	uncertainty [%]	experimental source	uncertainty [%]
scale	1.2	luminosity	3.7
PDF	1.6	trigger	1.0
branching fraction	2.7	p_{T}-smearing	0.1
WZ/ZZ/Wγ cross section	0.1	ϵ_{rec}	0.2
		isolation	0.2
		$E_{\mathrm{T}}^{\mathrm{miss}}$	3.3
		jet-veto	4.9
		background scaling	1.5
total theo. uncertainty	3.4	total exp. uncertainty	7.2

Table 6.7: The relative systematic uncertainties of the individual theoretical and experimental sources on the cross section are summarized.

- **PDF**: The uncertainties on the parton distribution functions have an effect on the acceptance of the MC signal. The systematic uncertainty of this contribution on the measured cross section is estimated comparing two independent PDF models to generate the MC signal, CTEQ [51] and MSTW [52]. More details on this estimation are given in [56].

- **branching fraction**: The measured W^+W^- signal in its two muon final state is scaled to the overall W^+W^- production using the branching fraction of $W^+W^- \to \mu^+\mu^-\nu_\mu\bar{\nu}_\mu$, which constitutes the branching fractions $\mathrm{Br}(W \to \mu)$, $\mathrm{Br}(W \to \tau)$ and $\mathrm{Br}(\tau \to \mu)$, as will be detailed in 6.7. The uncertainties of these branching fractions are propagated and given as a relative error on the cross section.

- **WZ/ZZ/Wγ cross section**: The uncertainty on the cross sections for the various physics processes contributing to the di-boson background, see 6.3.2, are estimated to be 5 % [56].

6.6.2 Experimental Uncertainties

The experimental uncertainties are dominated by the uncertainty related to the applied jet-veto as well as the luminosity and missing transverse energy. A complete list of identified sources of experimental uncertainties is given here:

- **luminosity**: The ATLAS collaboration estimated the uncertainty on the recorded luminosity to be 3.7 % [50].

- **trigger**: The Monte Carlo scale factors for the trigger efficiency is one within the error of 1 % [56]. We take this error as the systematic error on the trigger efficiency.

- **muons**: We identify three sources of uncertainties related to the selected muons. They are:
  - **p_T-smearing**: Modeling the resolution of the muon system is challenging and the transverse momentum of the simulated muons needs to be smeared to match the ones reconstructed in data. The simulated transverse muon momenta are smeared using common ATLAS tools [77]. The uncertainty introduced with this p_T-smearing is estimated by varying the smearing of the individual ID and MS tracks of the muons by one sigma up and down. The changes are propagated to the cross section and the largest found discrepancy is taken as the systematic uncertainty. However, it still remains on a sub-per-mill level and is hence a minor contribution.
  - **ϵ_{rec}**: As we showed in the previous chapter, efficiency scale factors need to be applied to the Monte Carlo muon efficiencies to match the ones on data. While one could take the scale factors measured in Chapter 5, we decide to use the common ATLAS tools, which are based on muons from Z-boson decays. The reason for this is, that our selected muons from W-boson decays have significantly higher transverse momentum than muons from J/ψ decays used in our study in Chapter 5. In the given muon momentum regime, the efficiency scale factors derived from Z-boson studies are hence more reliable and precise. A common ATLAS tool is used to scale the efficiencies and determine the uncertainty on the scaling [77]. The obtained relative error on the cross section from this contribution is 0.18 % and hence very small.
  - **isolation**: The isolation requirement on the muons also introduces an uncertainty. To investigate the effect on our measurement, we use a control region similar to the one already used in 6.5.3 to obtain a scaling factor for the Z+jets background. We follow the defined cut-flow, but instead of vetoing, we select Z-boson events by inverting the invariant mass cut in cut-flow step 4. In addition, we apply the jet-veto requirement to mimic as closely as possible the physics environment after the full selection. We then calculate the data - Monte Carlo agreement as the scaling factor

    $$s := 1 + \frac{N_{\mathrm{data}} - N_{\mathrm{MC}}}{N_{\mathrm{Z+jets}}} \tag{6.6}$$

    as has been detailed already in Section 6.5. We calculate s in the control region once with the muon selection including both, tracker and calorimeter isolation requirements and once with the loosened requirement that only one of the two muons has to pass the isolation cuts. The difference $\Delta s = 0.17\,\%$ of these two scale factors is taken as the systematic uncertainty on the isolation requirement. The small contribution is due to the selected control region that includes the jet-veto requirement.

- **$E_{\mathrm{T}}^{\mathrm{miss}}$**: The missing transverse energy is the sum of contributions from MS measurements as well as calorimeter measurements. The dominant contribution comes from the calorimeters. The uncertainty on the calorimeter terms in our $E_{\mathrm{T}}^{\mathrm{miss}}$ definition has been estimated to be 13.2 % [57]. To estimate the systematic uncertainty on the cross section from the missing transverse energy uncertainty we vary this term by the given 13.2 % and calculate the cross section. The average deviation of 3.32 % is taken as the corresponding systematic uncertainty.

- **jet-veto**: The uncertainty on the cross section that is introduced by the jet-veto requirement in the selection is estimated to be 4.9 % [56]. A Z-boson control region, similar to the one we used to estimate the effect of the isolation requirements but without a jet-veto is used to obtain this uncertainty in a data-driven way.

- **background scaling**: The uncertainty introduced with scaling the three leading background contributions, top, W+jets and Z+jets is another addition to the experimental sources of systematic uncertainties. The error on the individual scaling factors, listed in Table 6.5, is taken as the systematic uncertainty on the corresponding background.

6.7 Extracting the Cross Section

Analyzing the di-muon final state, the total W^+W^- cross section is defined as

$$\sigma_{WW} = \frac{N_{\mathrm{data}} - N_{\mathrm{bkg}}}{\epsilon\, \mathcal{A}\, \mathcal{L}\, \mathrm{Br}(WW \to \mu\mu)} \quad , \tag{6.7}$$

where N_{data} is the number of observed data events after the full selection and N_{bkg} is the number of background events that pass the same selection. N_{bkg} is hence the sum of the individual contributions of the simulated and scaled top, W+jets, Z+jets backgrounds and the simulated di-boson background, that are all normalized to the analyzed luminosity. Table 6.3 gives $N_{\mathrm{data}} = 179 \pm 13.4$ and Table 6.6 gives $N_{\mathrm{bkg}} = 48.3 \pm 10.3$. The errors are statistical. The integrated luminosity of the selected dataset $\mathcal{L}$ is given in Section 6.2 as $\mathcal{L} = 2052.49\ \mathrm{pb}^{-1}$. ϵ and $\mathcal{A}$ stand for efficiency and acceptance of the signal selection while $\mathrm{Br}(WW \to \mu\mu)$ denotes the total branching fraction of a di-muon final state of W^+W^-. Since the process $W \to \tau \to \mu$ [8] is added to the signal, we have to distinguish three processes with different $\epsilon\, \mathcal{A}$, i.e. the case in which both W-bosons decay directly into muons ($\mu\mu$), the one where one W-boson decays directly to a muon and the other decays via a τ to the muon final state ($\mu\tau$) and the case where both W-bosons decay via tau leptons into the di-muon final state ($\tau\tau$). We absorb in the following the acceptance into the efficiency and thus treat the efficiency times acceptance as one factor ϵ. It is

$$\begin{aligned} \epsilon\, \mathrm{Br}(WW \to \mu\mu) \;=\; & \epsilon_{\mu\mu}\, [\mathrm{Br}(W \to \mu)]^2 + \epsilon_{\tau\tau}\, [\mathrm{Br}(W \to \tau)\mathrm{Br}(\tau \to \mu)]^2 \\ & + 2\, \epsilon_{\mu\tau}\, [\mathrm{Br}(W \to \mu)\, \mathrm{Br}(W \to \tau)\, \mathrm{Br}(\tau \to \mu)] \end{aligned} \tag{6.8}$$

[8]To improve the readability we decide to simplify the indication of the physics processes by neglecting undetectable particles, i.e. the neutrinos as well as the indication of electric charges.

with $\text{Br}(W \to \mu) = (10.57 \pm 0.15)\,\%$, $\text{Br}(W \to \tau) = (11.25 \pm 0.20)\,\%$ and $\text{Br}(\tau \to \mu) = (17.39 \pm 0.04)\,\%$ [1]. The channel dependent efficiencies ϵ_{ij} are determined using the W^+W^- signal Monte Carlo samples. They are defined as

$$\epsilon_{ij} = \frac{N_{ij}^{\text{rec}}}{N_{ij}^{\text{gen}}} \quad \text{, with } \; i, j \in \{\mu, \tau\}\,. \tag{6.9}$$

with N_{ij}^{gen} being the number of generated $WW \to ij \to \mu\mu$ events and N_{ij}^{rec} being the number of corresponding events that pass the full selection after reconstruction. We find:

$$\begin{aligned} \epsilon_{\mu\mu} &= (8.795 \pm 0.082)\ \% \\ \epsilon_{\mu\tau} &= (2.730 \pm 0.076)\ \% \\ \epsilon_{\tau\tau} &= (0.563 \pm 0.115)\ \% \end{aligned}$$

The errors are statistical. The transverse momentum spectrum of muons from tau decays is significantly softer than the corresponding prompt muon spectrum as shown in Figure 6.11 and hence many more events do not fulfill the p_{T} requirements in these channels. The efficiencies in the $\tau \to \mu$ decay channels is hence significantly lower and the contributions of $W \to \tau$ events are correspondingly small.

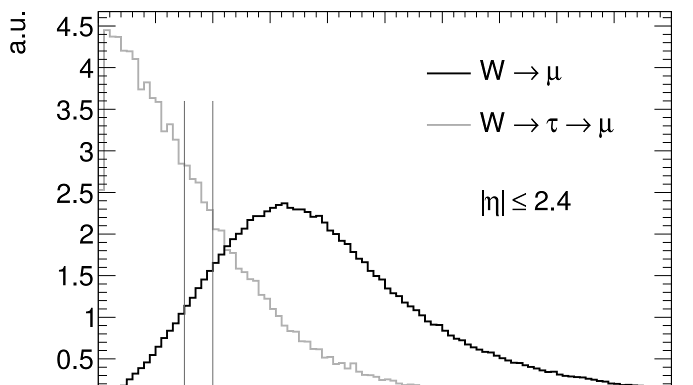

Figure 6.11: The transverse momentum spectra of muons from $W \to \mu$ and $W \to \tau \to \mu$ decays are compared on generator level. The transverse momentum requirements in our selection on the leading and sub-leading muon are indicated.

With the systematic uncertainties of theoretical and experimental sources discussed in the previous section, we are now ready to extract the W^+W^- production cross section at the LHC at a center-of-mass energy of 7 TeV. Equation 6.7 yields

$$\sigma_{pp \to W^+W^-}\,(\sqrt{s}{=}7\ \text{TeV}) = (58.0 \pm 7.5\ (\text{stat.}) \pm 1.9\ (\text{theo.}) \pm 4.3\ (\text{exp.}))\ \text{pb}\,. \tag{6.10}$$

6.8 Comparison to Other Measurements

With this result at hand, we compare our findings with the theoretical predictions given in 1.4.1 as well as the already existing W^+W^- cross section measurements at the LHC [47,48]. Table 6.8 lists prediction and measurements. All measured results agree within one sigma with the predictions. However, the difference between the two results of the measurements in the di-muon channel is peculiar. The signal in the di-muon final state of the ATLAS analysis consists of 64 events. Considering that the used dataset is also included in our dataset and that our muon identification efficiency is about 93 %, we follow a conservative approach and assume that all 64 ATLAS signal events are included in our 179 observed signal events. With this statistical separation we calculate a difference between the ATLAS result in the di-muon channel and our results to be 2.2 sigma. Since the cut-flows are very similar in the two analyses, the observed discrepancy has to be due to the significantly lowered transverse momentum requirement in our analysis. With these cuts, one might be more sensitive to a possibly low mass Higgs boson and its decay into a W-pair, which motivates the following section.

source	σ_{WW} [pb]		uncertainty [pb]		
SM prediction	47.0	±	2.0		
our measurement	58.0	±	7.5 (stat.)	±	4.7 (sys.)
ATLAS ($\mu\mu$)	43.2	±	8.1 (stat.)	±	4.7 (sys.)
ATLAS (leptonic)	54.4	±	4.0 (stat.)	±	4.3 (sys.)
CMS (leptonic)	41.1	±	15.3 (stat.)	±	7.3 (sys.)

Table 6.8: The Standard Model prediction is compared to our measured value of the W^+W^- production cross section. The results of the ATLAS analysis, for the $\mu\mu$ channel as well as the combination of $\mu\mu$, μe and ee channel (leptonic) are given in addition.

6.9 What about the Higgs?

Although our analysis is not optimized for a search of the Higgs boson, it would still be sensitive to the process $H \to W^+W^-$, which we are going to exploit in this section.

As discussed in Chapter 1, the theory favors a low mass Higgs boson. Given the current Higgs boson mass limits, we assume a Standard Model Higgs boson with a mass of 130 GeV. The four leading production processes of a Higgs boson are simulated and listed in Table 6.9. Adding the total cross section of the four production processes and multiplying the branching fraction $BR(H \to WW)$ yields an expected cross section of $\sigma^{\text{predicted}}_{pp\to H\to WW} = 4.9^{+0.9}_{-0.7}$ pb [66].
Figure 6.12 supports the presumption made in the last section. The transverse momentum distribution of the sub-leading muons passing our full selection requirements in the simulated Higgs boson samples is shown. The tighter requirement of the alternative W^+W^- analyses is indicated in the plot to show the events that are added in our selection. The lowered transverse momentum requirement on the sub-leading muon enhances the signal

selection by over 55 % compared to corresponding requirements in the alternative analyses discussed above.
We add the Higgs boson samples to our analysis and Figure 6.13 shows the transverse mass distribution as well as the opening angle between the two muons after the full event selection. We observe some improvement of the data - Monte Carlo agreement after adding the Higgs boson processes, though their overall contribution is small.

There are two ways to look at the SM Higgs boson in this context. We can treat it as the signal or as a background. Both approaches are discussed subsequently.

simulated SM Higgs boson processes and cross sections [pb]

H	$\rightarrow$	W^+W^-	$\rightarrow$	$l^+\, l'^-\, \nu_l\, \bar{\nu}_{l'}$	0.452
$q\,q\,H$	$\rightarrow$	$W^+W^- + X$	$\rightarrow$	$l^+\, l'^-\, \nu_l\, \bar{\nu}_{l'} + X$	0.037
$W^\pm H$	$\rightarrow$	$W^\pm W^+W^-$	$\rightarrow$	$l^+\, l'^-\, \nu_l\, \bar{\nu}_{l'} + X$	0.016
$Z\,H$	$\rightarrow$	$Z\,W^+W^-$	$\rightarrow$	$l^+\, l'^-\, \nu_l\, \bar{\nu}_{l'} + X$	0.009

Table 6.9: The simulated Standard Model Higgs boson production processes are illustrated and presented with the corresponding cross section assuming a Higgs boson mass of $m_H = 130$ GeV. $l, l' \in \{e, \mu, \tau\}$.

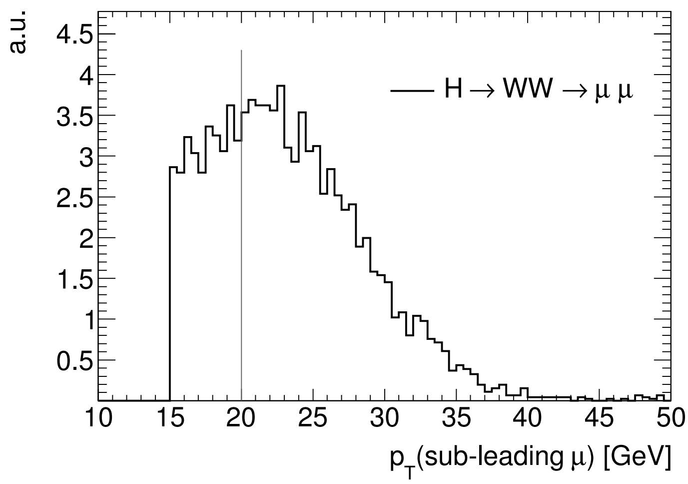

Figure 6.12: The transverse momentum spectrum of the sub-leading muons in the simulated Higgs boson samples are shown for the events that pass the full selection.

6.9.1 The Standard Model Higgs Cross Section

We assume that the observed discrepancy between the predicted SM W^+W^- production cross section and our measurement is caused by the presence of the SM Higgs boson. In

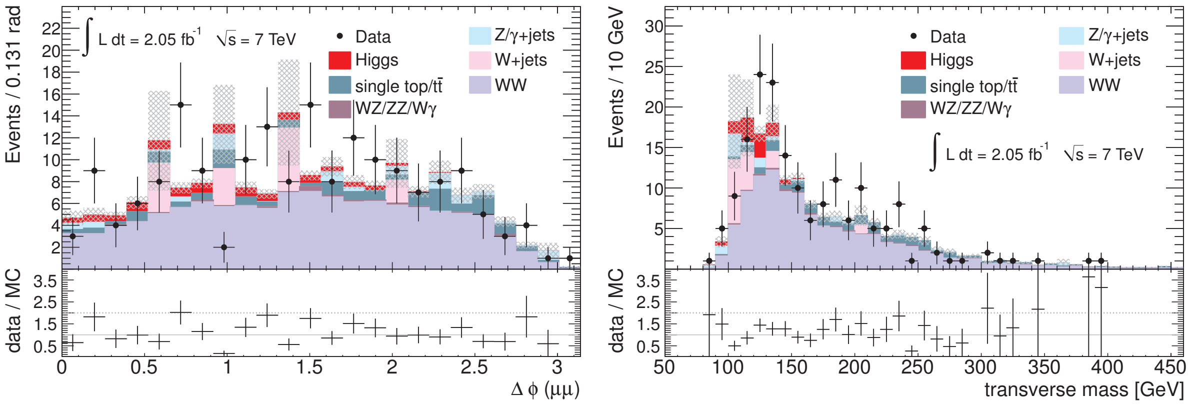

(a) opening angle (b) transverse mass

Figure 6.13: The opening angle between the two muons as well as the transverse mass distribution are shown after the full event selection.

this case, we can calculate its production cross section in the W^+W^- channel to

$$\sigma_{pp\to H\to W^+W^-}\,(\sqrt{s}=7\text{ TeV}) = ((58.0 \pm 8.9) - (47.0 \pm 2.0))\text{ pb} = (11.0 \pm 9.1)\text{ pb}. \quad (6.11)$$

Our measurement is hence in perfect agreement with the SM Higgs boson predictions of $4.9^{+0.9}_{-0.7}$ pb. However, we also observe that our measurement is less than 1.3 standard deviations from zero.

6.9.2 The Higgs Boson as a Background

Another approach is extending our SM W^+W^- cross section measurement. We now treat the Higgs boson samples as an additional, irreducible background contribution to our Standard Model W^+W^- signal. Applying the full selection to the Higgs boson samples, which are normalized to the analyzed luminosity yields $N_{\text{Higgs}} = 10.7 \pm 0.2$. We recalculate $\sigma_{W^+W^-}$ with the Higgs boson processes as an additional background and find

$$\sigma_{pp\to WW}\,(\sqrt{s}=7\text{ TeV}) = (53.2 \pm 7.5\text{ (stat.)} \pm 4.7\text{ (sys.)})\text{ pb} \quad (6.12)$$

where we assume a 10 % uncertainty on the cross section of the Higgs boson production as an additional systematic uncertainty. The central value is now reduced by the Higgs boson cross section, as expected and hence closer to the predictions. The result of our SM W^+W^- cross section measurement including the Higgs boson does agree with the Standard Model prediction within the statistical uncertainties. However, the result presented in Equation 6.10, neglecting the possible existence of a Higgs boson still agrees within about one sigma of total uncertainties with the Standard Model predictions.

6.10 Conclusion

We present the most precise measurement of the Standard Model W^+W^- production cross section in the di-muon decay channel at the center of mass energy of 7 TeV. The result is in agreement with existing measurements as well as the Standard Model predictions. No significant deviations from the Standard Model were found.
However, a discrepancy of about one sigma is observed between our measurements and the SM predictions. Assuming that this difference is due to the presence of a SM Higgs boson and not the result of statistical fluctuations, we calculate the Higgs boson cross section and find it to be in agreement with the corresponding SM predictions. However, within less than 1.3 sigma it is also in agreement with zero.
Furthermore, we treat the SM Higgs boson as an additional background to our SM W^+W^- production. Adding the corresponding Monte Carlo samples to our backgrounds, assuming a Higgs boson mass of $m_H = 130$ GeV, yields a W^+W^- production cross section that is in better agreement with the SM predictions.
Although our measurements and the SM Higgs boson predictions show a good agreement, the available statistics is too limited to allow for a conclusive statement about the existence of the Higgs boson, yet.

CHAPTER 7

Summary & Outlook

The Long Awaited Collision Data

In March 2010, the ATLAS experiment at the Large Hadron Collider LHC at CERN started its long anticipated and very successful data taking stage. After almost 3 decades, from the first conceptual studies over the development and construction, the largest particle collider experiment ever built finally became operational, recording proton-proton collisions at a center of mass energy of 7 TeV. The additional time the LHC construction and commissioning required before starting the 2010 run was well used by the ATLAS collaboration. Based on simulated Monte Carlo samples and recorded cosmic muons, the detector alignment was improved and the software to reconstruct and identify the physics objects in data was studied, refined and updated. Detector as well as reconstruction software were consequently in a good shape the moment the first data arrived in 2010. Nevertheless, thorough studies of the performance of all sub-detector systems as well as all parts of the software on the recorded data are a crucial necessity before any complex physics analysis.

Besides investigating the performance of the B-field sensors that monitor the toroidal magnetic field in ATLAS which is necessary to measure the momenta of traversing muons, we used the early ATLAS data to scrutinize an important muon identification algorithm, the muon segment tagger MuTagIMO.

Muons in First ATLAS Data

At the very beginning of the data taking phase of ATLAS, muon segment taggers used to be neglected for very most physics analyses involving muons with sufficiently high transverse momentum to use combined algorithms for their identification ($p_{\mathrm{T}} \gtrsim 8$ GeV). The mis-tag rate was simply too high so that, despite its high efficiency, the tagged muon collection was not sufficiently pure. Through detailed studies on first data as well as Monte

Carlo simulations, we were able to improve the performance of MuTagIMO considerably by lowering the mis-tag rate by about a factor 2 while maintaining the high efficiency of the algorithm. In our physics analysis detailed in the last chapter we demonstrated that the improved MuTagIMO segment tagger is a valuable addition to the established combined algorithms even for the identification of high momentum muons.

Besides MuTagIMO, there are five additional, independent algorithms to identify muons in ATLAS. In addition, the 'or' of combinations of algorithms is commonly used to increase the identification efficiency. In order to get an overview and detailed understanding on the performances of the individual algorithms and their commonly used combinations, we measured their efficiencies on data. A Tag-and-Probe method on J/ψ particles was used which allowed us to measure not only the flat plateau region of the algorithm efficiencies but also the threshold curve, where they become operational. We hence obtained a complete picture of the individual identification efficiencies. Through the selection of calorimeter tagged muons instead of Inner Detector tracks as probes in the method, the measurement is the most precise of its kind in ATLAS. The results on first data were compared to the corresponding efficiencies on simulated Monte Carlo samples and scale factors depending on the transverse muon momentum and the pseudorapidity were determined. We concluded that the Muid algorithm family shows an overall higher identification efficiency with MuTagIMO being the most efficient muon identification algorithm in ATLAS.

Measuring the W^+W^- Cross Section Using Muons

The excellent performance in 2010 and 2011 of both, the LHC and the ATLAS detector exceeded the most optimistic prediction by far. The amount and quality of data that has been recorded in 2011 by ATLAS allowed us to present an important measurement that does not only provide a crucial test of the Standard Model but is also essential to accomplish one of the major goals of the experiment, the discovery or exclusion of the Standard Model Higgs boson.

The production of W^+W^- events includes triple gauge couplings, which arise from the non-abelian structure of the weak force. A precise measurement of the W^+W^- production cross section is hence sensitive to an elementary feature of the Standard Model. Additionally, SM W^+W^- events represent the largest and irreducible background contribution to Higgs boson searches in the $H \to W^+W^-$ channel, which is the dominant decay channel for Higgs masses larger than 135 GeV [66]. A search for the Higgs in this important channel requires hence a detailed understanding and therefore a precise measurement of the Standard Model W^+W^- production.

We measured the Standard Model W^+W^- production cross section in the di-muon final state, i.e. $W^+W^- \to \mu^+\mu^-\nu_\mu\bar{\nu}_\mu$, taking advantage of our experiences with muons. At this point we profited from our work on the improved muon segment tagger MuTagIMO, which allowed us to increase our selection efficiency. Following our results on the measured muon identification efficiencies, we chose to select one Muid Combined muon and one muon that was either found by MuTagIMO or Muid Combined to select W^+W^- can-

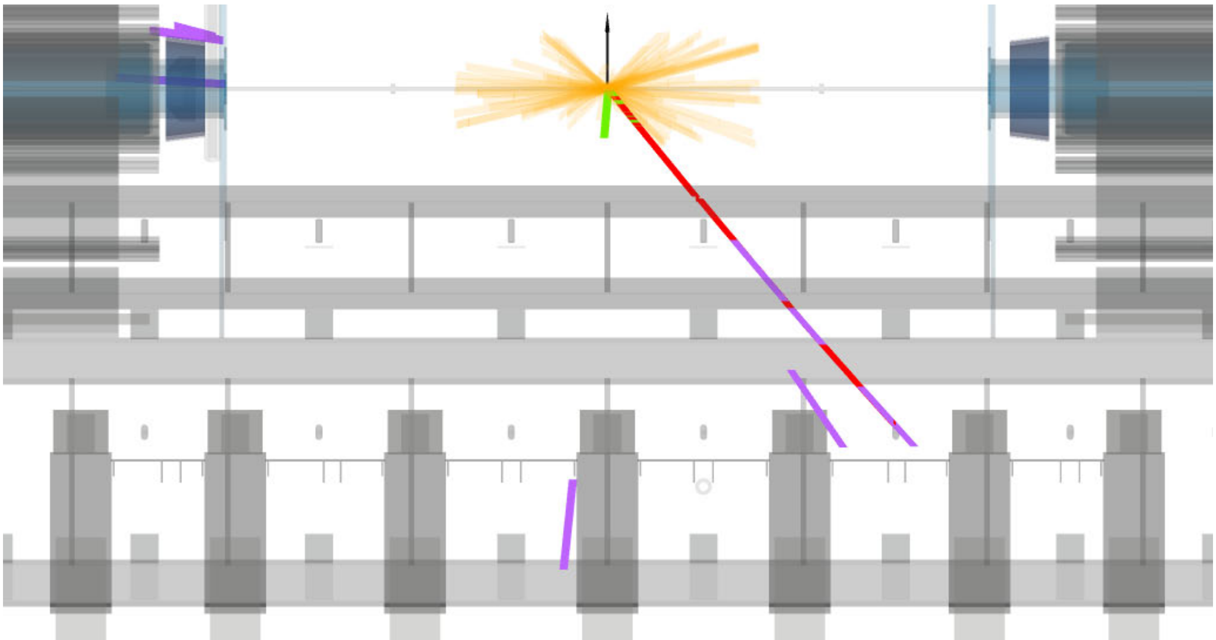

Figure 7.1: Event display of a W^+W^- candidate in ATLAS (side-view). The track of the combined muon is depicted in red, the one of the segment tagged muon is depicted in green. The black arrow illustrates $E_{\mathrm{T}}^{\mathrm{miss}}$. Inner Detector tracks with $p_{\mathrm{T}} > 1$ GeV are shown in orange and segments in the muon system are shown in purple. The visualization is based on ATLAS event 14817677 in run 187811.

didates. Figure 7.1 illustrates the abilities of MuTagIMO, showing an additional event display of a W^+W^- event in which one muon ($p_{\mathrm{T}} = 55.6$ GeV, $\eta = -0.06$) is missed by the combined algorithms since it falls within the feet region of the detector in the $\eta = 0$ acceptance hole of the ATLAS muon system. MuTagIMO successfully recovers this muon with only a single MDT segment present. Together with the three station combined muon in the event ($p_{\mathrm{T}} = 23.5$ GeV, $\eta = 0.5$), all requirements on W^+W^- events are passed. The two muon transverse mass is $m_{\mathrm{T}} = 121.4$ GeV.

We measured the Standard Model W^+W^- production cross section at a center of mass energy of 7 TeV to be

$$\sigma_{pp\to WW}\,(\sqrt{s}{=}7\text{ TeV}) = (58.0 \pm 7.5\text{ (stat.)} \pm 1.9\text{ (theo.)} \pm 4.3\text{ (exp.)})\text{ pb} \tag{7.1}$$

which represents the most precise measurement of this cross section in the di-muon final state to date. Our result is in agreement with the SM prediction of (47.0 ± 2.0) pb, though the observed discrepancy in the central value sparked a discussion about the Higgs boson.

Is There a Higgs?

In our W^+W^- cross section measurement we did not take the existence of a possible Higgs boson into account. It is hence reasonable to check the impact a Standard Model Higgs boson would have on our measurement. In order to do so, we assumed a low mass Higgs boson, as favored by the theory. We set the mass of the Higgs to $m_{\mathrm{H}} = 130$ GeV and added it to our backgrounds. The presence of the Higgs in the backgrounds lowers the central value of the measured W^+W^- cross section to $(53.2 \pm 7.5\ \text{(stat.)} \pm 4.7\ \text{(sys.)})$ pb and hence the measurement agrees within statistical uncertainties with the prediction.

In addition, we estimated the Higgs boson cross section, assuming that the observed discrepancy between our measurement and the prediction is caused by the presence of the Higgs. The result, $\sigma_{pp\to H\to WW} = (11.0 \pm 9.1)$ pb is well in agreement with the Standard Model predictions ($\sigma^{\text{predicted}}_{pp\to H\to WW} = 4.9^{+0.9}_{-0.7}$ pb), but the uncertainties are too large for any conclusive statement.

We would have loved to give a definitive answer to the question that titles this section. However, we could not present any proof for the presence of a Standard Model Higgs boson in the analyzed dataset. While some might already see a hint or even a glance of the Higgs in the presented measurement, more luminosity is needed to end the guesswork. Luckily, the successful run of the LHC and the ATLAS detector continues at full speed.

Supplement: DISCOVERY

On the 4th of July 2012 the two LHC experiments ATLAS and CMS presented the latest results on their Higgs searches to the global community of scientists as well as to the public media. Both experiments observe an excess of events at a mass of around 126 GeV with a significance of $5\,\sigma$ (ATLAS), and $4.9\,\sigma$ (CMS) respectively. A new particle has been discovered that resembles a Standard Model Higgs boson. ATLAS presented the analysis of a di-photon decay channel, as well as the channel with two Z-bosons in their leptonic decays (e, μ). The analysis of the W^+W^- channel was not ready for publication at this date but also seems to confirm the observation in the other channels as has been discussed in internal ATLAS presentations. The extracted production cross section of the discovered particle agrees well with the Standard Model predictions for a Higgs boson with $m_H = 126$ GeV. However, more data is needed to measure additional properties of the discovered particle before definite conclusions on the Standard Model Higgs boson can be drawn.

This discovery also supports our findings in the last chapter. The shown event displays in Figure 6.6 and 7.1 might hence also show a Higgs boson in its W^+W^- decay.

Samenvatting

Langverwachte botsingen

In maart 2010 is het ATLAS experiment in de Large Hadron Collider LHC op CERN begonnen aan de langverwachte, en tot nu toe zeer succesvolle periode van data verzamelen. Bijna drie decennia na de eerste conceptuele studies naar de ontwikkeling en bouw, is het grootste deeltjesversneller-experiment dat ooit gebouwd is in gebruik genomen en begonnen met het vastleggen van proton-proton botsingen met een botsingsenergie van 7 TeV. De extra tijd die nodig was voor de bouw en het in gebruik nemen van de LHC is goed gebruikt door het team van ATLAS. Met behulp van Monte Carlo-simulatie en kosmische muonen werd de uitlijning van de detector verbeterd, en de software voor het reconstrueren en identificeren van deeltjes in de data onderzocht en verfijnd. De detector en reconstructie software waren dus in goede staat op het moment dat de eerste data gemeten werd in 2010. Toch zijn grondige studies van de prestaties van alle onderdelen van de detector en de software op basis van de gemeten gegevens cruciaal voor elke complexe natuurkundige analyse.

In ATLAS wordt een magneetveld gebruikt om de impuls van muonen te meten. We hebben de prestaties van de sensoren die dit magneetveld meten bestudeerd. Daarnaast hebben we de eerste ATLAS data gebruikt om een belangrijk algoritme voor muon-identificatie – de muon-segment-tagger, MuTagIMO – te onderzoeken.

Muonen in de eerste ATLAS-data

Bij de analyse van de allereerste ATLAS-data werden voor de identificatie van muonen met een hoge transversale impuls ($p_T > 8$ GeV) meestal geen muon-segment-taggers, maar gecombineerde algoritmes (combined algorithms) gebruikt. De kans op een foutieve tag (een 'false positive') was te hoog, waardoor de set gevonden muonen niet voldoende betrouwbaar bleek, ondanks de hoge efficiëntie. Met gedetailleerde studies van zowel data als simulatie hebben we de prestaties van MuTagIMO aanzienlijk kunnen verbeteren door het verlagen van de kans op een foutieve tag met ongeveer een factor twee, met behoud van de hoge efficiëntie van het algoritme. In de analyse zoals beschreven in het laatste hoofdstuk van dit proefschrift hebben we laten zien dat de verbeterde MuTagIMO segment-tagger een waardevolle aanvulling is op de bestaande gecombineerde algoritmes, zelfs voor de identificatie van muonen met hoge transversale impuls.

Er zijn naast MuTagIMO vijf andere, onafhankelijke algoritmes om muonen in ATLAS te identificeren. Ook worden combinaties van algoritmes gebruikt om een betere identificatie-efficiëntie te behalen. Voor het verkrijgen van gedetailleerd inzicht in de prestaties van zowel de individuele algoritmes als de veel gebruikte combinaties hiervan, is hun efficiëntie gemeten in de data. Een tag-and-probe-methode gebaseerd op de meting van het J/ψ-deeltje stelde ons in staat om de afhankelijkheid van deze efficiëntie ten opzichte van bepaalde variabelen te meten. Zo hebben we een compleet beeld verkregen van de individuele identificatie-efficiëntie. Door de muonen die in de calorimeter getagged zijn te gebruiken als 'probes', in plaats van sporen in de Inner Detector, is de meting de meest nauwkeurige in zijn soort in ATLAS. De resultaten uit de eerste data zijn vergeleken met de overeenkomstige efficiënties in simulatie en schaalfactoren afhankelijk van de transversale impuls en de pseudorapiditeit zijn bepaald. We concludeerden dat de Muid-algoritmes gemiddeld een hogere identificatie-efficiëntie bereiken en dat MuTagIMO het meest efficiënte algoritme voor muonidentificatie in ATLAS is.

Meting van de werkzame doorsnede van W^+W^- met muonen

De uitstekende prestaties van zowel de LHC als de ATLAS-detector in 2010 en 2011 hebben de meest optimistische voorspellingen ruim overtroffen. De hoeveelheid en kwaliteit van de gemeten data in 2011 maakte het mogelijk om een belangrijke meting te doen die niet alleen een cruciale test van het Standaard Model is, maar ook essentieel voor het bereiken van een van de belangrijkste doelstellingen van het experiment: de ontdekking of uitsluiting van het Standaard Model Higgs-boson.

De productie van W^+W^--events omvat drievoudige ijkkoppelingen, die voortvloeien uit de niet-Abeliaanse structuur van de zwakke kracht. Een nauwkeurige meting van de W^+W^--productiedoorsnede is dus gevoelig voor een elementair onderdeel van het Standaard Model. Los daarvan vertegenwoordigen Standaard Model W^+W^--events de grootste en niet te reduceren achtergrond voor de zoektocht naar het Higgs-boson in het $H \to W^+W^-$-kanaal, het dominante vervalskanaal als de Higgs massa groter blijkt dan 135 GeV [66]. Een zoektocht naar het Higgs-deeltje in dit belangrijke kanaal vereist dus een gedetailleerd begrip en nauwkeurige meting van de W^+W^--productie. We hebben de Standaard Model W^+W^--productiedoorsnede gemeten met de 'di-muon'-eindtoestand, $W^+W^- \to \mu^+\mu^-\nu_\mu\bar{\nu}_\mu$, zodat we konden profiteren van onze ervaringen met muonen. Hier kwamen onze verbeteringen van de muon segment-tagger MuTagIMO van pas, omdat hierdoor onze selectie efficiënter werd. Naar aanleiding van eerdergenoemde resultaten kozen we ervoor om voor onze W^+W^--kandidaten één muon te selecteren dat is gevonden door Muid Combined, en één muon dat is gevonden door MuTagIMO of Muid Combined. Figuur 7.2 illustreert de mogelijkheden van MuTagIMO. Dit is een weergave van een kandidaat voor een W^+W^--event waarin een muon ($p_{\mathrm{T}} = 55.6$ GeV, $\eta = -0.06$) wordt gemist

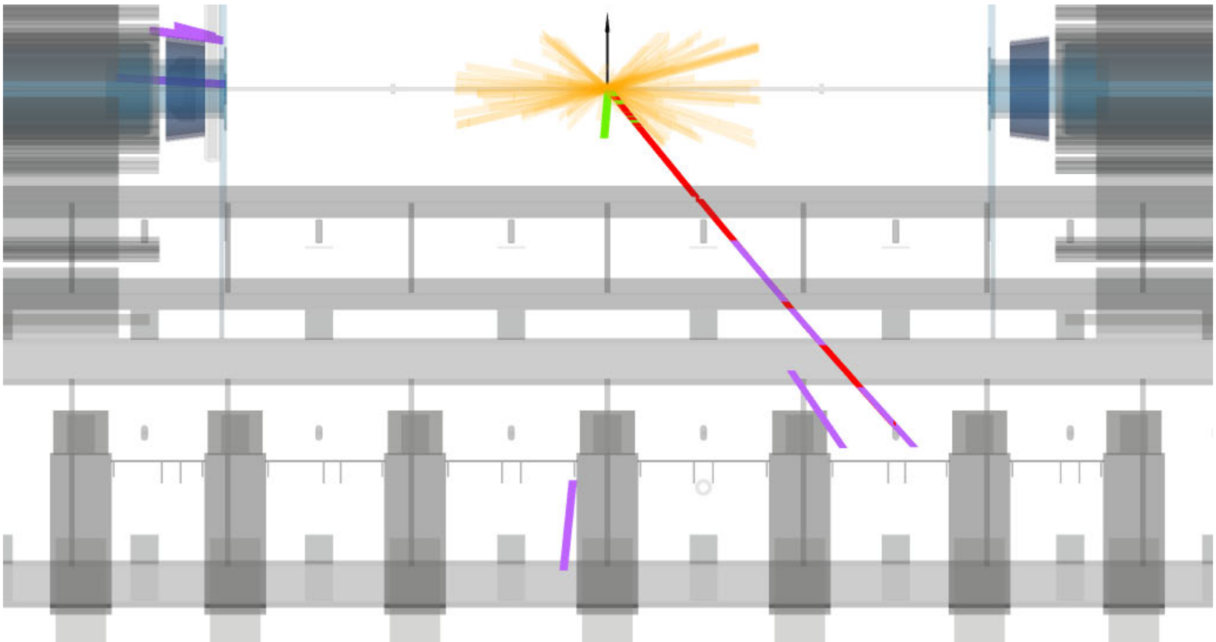

Figure 7.2: Weergave van een kandidaat voor een W^+W^--event in ATLAS (zijaanzicht). Het spoor van het gecombineerde muon is weergegeven in het rood, het muon uit de segment-tagger in het groen. De zwarte pijl geeft de $E_{\mathrm{T}}^{\mathrm{miss}}$ weer. Sporen in de Inner Detector met $p_{\mathrm{T}} > 1$ GeV zijn oranje, en de segmenten in het muonsysteem zijn paars gekleurd. Deze weergave is gebaseerd op ATLAS event 14817677 in run 187811.

door de gecombineerde algoritmes. Dit gebeurt omdat het spoor in het gebied van de voet van de detector valt, in de buurt van $\eta = 0$, een gat in het bereik van het muonsysteem van ATLAS. MuTagIMO vindt dit muon echter met succes terug ondanks dat slechts één MDT is geraakt. Samen met het muon van het gecombineerde algoritme met drie segmenten ($p_{\mathrm{T}} = 23.5$ GeV, $\eta = 0.5$), wordt aan alle eisen voor een W^+W^--event voldaan. De gezamenlijke transversale massa van de twee muonen is $m_T = 121.4$ GeV.

De Standaard Model W^+W^--productiedoorsnede bij een effectieve botsingsenergie van 7 TeV is

$$\sigma_{pp\to WW}\,(\sqrt{s}{=}7\ \mathrm{TeV}) = (58.0 \pm 7.5\ (\mathrm{stat.}) \pm 1.9\ (\mathrm{theo.}) \pm 4.3\ (\mathrm{exp.}))\ \mathrm{pb} \quad , \qquad (7.2)$$

wat neerkomt op de meest nauwkeurige meting van deze doorsnede in de di-muon-eindtoestand tot nu toe. Ons resultaat is in overeenstemming met de voorspelling van het Standaard Model van (47.0 ± 2.0) pb, hoewel de waargenomen discrepantie in de centrale waarde leidde tot een discussie over het Higgs boson.

Bestaat het Higgs-deeltje?

In onze meting van de werkzame doorsnede van W^+W^--productie houden we geen rekening met het bestaan van een mogelijk Higgs-boson. Het ligt daarom voor de hand om te controleren wat de impact van een Higgs-boson op onze meting zou zijn, volgens het Standaard Model. Om dit te bewerkstelligen, zijn we uitgegaan van een Higgs-boson met lage massa, de voorkeur van de theorie. We zetten de massa van het Higgs-deeltje op $m_H = 130$ GeV en hebben dit toegevoegd aan onze achtergronden. De aanwezigheid van het Higgs-deeltje in de achtergrond verlaagt de gemeten centrale waarde van de W^+W^--productiedoorsnede tot $(53.2 \pm 7.5(stat.) \pm 4.7(sys.))$ pb en daarmee is de meting binnen statistische onzekerheden in overeenstemming met de voorspellingen.

Daarnaast hebben we de werkzame doorsnede van het Higgs-boson afgeschat, in de veronderstelling dat het waargenomen verschil tussen onze meting en de voorspelling wordt veroorzaakt door de aanwezigheid van het Higgs-deeltje. Het resultaat, $\sigma_{pp \to H \to WW} = (11.0 \pm 9.1)$ pb is in overeenstemming met de voorspellingen in het Standaard Model ($\sigma^{\text{predicted}}_{pp \to H \to WW} = 4.9^{+0.9}_{-0.7}$ pb), maar de onzekerheden zijn te groot zijn voor een sluitende uitspraak.

We hadden natuurlijk graag een definitief antwoord gegeven op de titelvraag van deze paragraaf. Maar we konden geen enkel bewijs voor de aanwezigheid van een Higgs-boson in de geanalyseerde dataset vinden. Terwijl sommigen misschien een hint van of zelfs een blik op het Higgs-deeltje zien in de gepresenteerde meting, is meer helderheid nodig om speculatie te voorkomen. Gelukkig draaien de LHC en de ATLAS-detector nog steeds op volle toeren.

Toegift: DE ONTDEKKING

Op 4 juli 2012 presenteerden de twee LHC-experimenten ATLAS en CMS wereldwijd de laatste resultaten van de Higgs-zoektocht aan wetenschappers en publieke media. Beide experimenten nemen een overschot aan events waar, bij een massa van ongeveer 126 GeV , met een significantie van $5\,\sigma$ (ATLAS), en $4.9\,\sigma$ (CMS). Dit betekent de ontdekking van een nieuw deeltje dat lijkt op een Higgs-boson uit het Standaard Model. ATLAS presenteerde de analyse van het di-fotonvervalskanaal en het kanaal met twee Z-bosonen en hun leptonverval. De analyse van het W^+W^--kanaal was nog niet klaar voor publicatie op 4 juli, maar ook deze meting lijkt de waarneming te bevestigen. De afgeleide productiedoorsnede van het ontdekte deeltje komt goed overeen met de voorspellingen voor een Higgs-boson met $m_H = 126$ GeV in het Standaard Model. Er is echter meer data nodig om de andere eigenschappen van het ontdekte deeltje te meten voordat definitieve conclusies over het Higgs-boson kunnen worden getrokken.

Deze ontdekking ondersteunt ook onze bevindingen in het laatste hoofdstuk. De weergegeven events in Figuur 6.6 en 7.2 zouden dus ook een Higgs-boson dat naar W^+W^- vervalt kunnen zijn.

APPENDIX **A**

MuTagIMO: Matching Quantities

The following variables are used to match MS segments to ID tracks by MuTagIMO:

- $\mathcal{R}_X$: This quantity is the residual in the local X coordinate:

$$\mathcal{R}_X = locX^{exTrk} - locX^{seg}$$

- $\mathcal{R}_{XZ}$: The residual of the angle in the local XZ plane:

$$\mathcal{R}_{XZ} = \alpha_{xz}^{exTrk} - \alpha_{xz}^{seg}$$

- $\mathcal{R}_Y$: This quantity is the residual in the local Y coordinate:

$$\mathcal{R}_Y = locY^{exTrk} - locY^{seg}$$

- $\mathcal{R}_{YZ}$: The residual of the angle in the local YZ plane:

$$\mathcal{R}_{YZ} = \alpha_{yz}^{exTrk} - \alpha_{yz}^{seg}$$

- $\mathcal{P}_X$: This quantity is the pull in the local X coordinate and defined as:

$$\mathcal{P}_X = \frac{\mathcal{R}_X}{\sqrt{\Delta(locX^{exTrk})^2 + \Delta(locX^{seg})^2 + s_{locX}^2}},$$

  where s_{locX} is a safety factor set to 50 mm.

- $\mathcal{P}_Y$: This quantity is the pull in the local Y coordinate and defined as:

$$\mathcal{P}_Y = \frac{\mathcal{R}_Y}{\sqrt{\Delta(locY^{exTrk})^2 + \Delta(locY^{seg})^2 + s_{locY}^2}},$$

  where s_{locY} is a safety factor set to 10 mm.

- $\mathcal{P}_{YZ}$: The to $\mathcal{R}_{YZ}$ corresponding pull:

$$\mathcal{P}_{YZ} = \frac{\mathcal{R}_{YZ}}{\sqrt{\Delta(\alpha_{yz}^{exTrk})^2 + \Delta(\alpha_{yz}^{seg})^2 + s_{\alpha_{yz}}^2}}$$

  where $s_{\alpha_{yz}}$ is a safety factor set to 0.5 mrad.

- $\mathcal{R}_{max}$: This quantity gives the distance between the extrapolated track and the MDT chambers with the associated segment in the non precision plane.

- $\mathcal{P}_{chamber}$: This distribution corresponds to the pull distribution of $\mathcal{R}_{max}$, hence

$$\mathcal{P}_{chamber} = \frac{\mathcal{R}_{max}}{\sqrt{\Delta(\mathcal{R}_{max})^2}}$$

- $\mathcal{P}_{CY}$: This pull relates position and direction and was introduced as an additional powerful discriminant to reduce the fake rate[1]

$$\mathcal{P}_{CY} = \frac{\mathcal{R}_{Y} - c * \mathcal{R}_{YZ}}{\sqrt{\Delta(locY^{exTrk})^2 - c^2\Delta(\alpha_{yz}^{exTrk})^2 + \Delta(locY^{seg})^2 + c^2\Delta(\alpha_{yz}^{seg})^2}}$$

  where c is a correction factor obtained from the covariance and the individual errors on position and direction of the extrapolated track.

X, Y and Z are coordinates of the local coordinate system which is drawn in Figure 4.1 on page 58.

[1] The denominator becomes $\sqrt{\Delta(locY^{exTrk})^2 + \Delta(locY^{seg})^2 + c^2\Delta(\alpha_{yz}^{seg})^2}$ for the cases where $\Delta(locY^{exTrk})^2 - c^2\Delta(\alpha_{yz}^{exTrk})^2 < 0$.

APPENDIX B

Tag&Probe: Muon Trigger Requirements

The tag muon is required to have fired the muon trigger that had the event recorded. Since the instantaneous luminosity of the LHC increased significantly over time during the used dataset was recorded, the low momentum triggers had to be prescaled. Only a fraction of the events, the prescale factor, where the trigger fired was recorded, since the rate was to high to write out all events that had the trigger fired. The lowest unprescaled muon trigger is chosen for each data period to obtain high statistics while making sure the trigger bias is absent.The lowest unprescaled muon trigger as function of time or ATLAS run number is shown in Table **??**. 'L1' stands for the level one trigger and 'EF' for event filter, the high level trigger of ATLAS. The index 'mu' indicates the single muon trigger, while the attached number is the trigger threshold in GeV.

run number (N_r)	data period	trigger
$N_r < 158443$	B, C, D1	L1_MU0
$158443 \leq N_r < 161118$	D2-D6, E1-E4, E6-E7	EF_mu4
$161118 \leq N_r \leq 161379$	E5, F1, $F2_1$	EF_mu6
$161379 < N_r \leq 161948$		
$162764 \leq N_r \leq 162882$	$F2_2$, G1-G4	EF_mu10
$165591 \leq N_r \leq 166964$	G5-G6, H	EF_mu13

Table B.1: The lowest unprescaled triggers in the different data periods are shown with the corresponding run numbers of 2010 ATLAS data.

APPENDIX C

Muon Inner Detector Track Requirements

To ensure a reliable and precise muon momentum reconstruction various requirements on the Inner Detector track of the muon are applied. The subsequently listed requirements were studied in detail and subsequently recommended by the ATLAS Muon Combined Performance group [77]. For a detailed description of the Inner Detector, the reader is referred to Chapter 2. The requirements are:

- at least one BLayer pixel hit needs to be associated to the track, if the muon ID track traverses pixels in the BLayer that are known to work.
- the sum of Pixel Detector hits and crossed dead Pixel sensors is at least 2.
- the sum of SCT Detector hits and crossed dead SCT sensors is at least 7.
- the number of Pixel and SCT holes is less then 2. A hole is a sensor that is expected to have fired, but did not.
- a successful extension of the ID track to the TRT Detector is required. Since the TRT acceptance only reaches up to $\eta = 2$ the following distinction is made:
  - $|\eta| < 1.9$: number of TRT hits and TRT outliers is required to be larger than 5. In addition, the fraction of outliers must be smaller than 90% of the sum of hits and outliers.
  - $|\eta| \geq 1.9$: if the number of TRT hits and TRT outliers is larger than 5, then the fraction of outliers must be smaller than 90% of the sum of hits and outliers.

APPENDIX D

Muon Efficiencies: Scaling Factors

The plotting ranges in Figures 5.10 and 5.11 are chosen to visualize both, the data - Monte Carlo agreement in the threshold curves as well as in the plateau region. Since the discrepancies are significantly smaller in the plateau region, the sf's in certain low momentum bins are outside the plotting range. A list of these sf's with their errors is given in the subsequent Table D.1. No Staco Combined muons with a transverse momentum below 2.5 GeV were reconstructed in the simulated samples. The corresponding scaling factor is hence not a real number.

		scaling factor in			
algorithm(s)	p_T bin [GeV]	barrel	trans. region	endcap	csc region
Muid Combined	$[2.5, 3]$	$1.43^{+0.24}_{-0.22}$			
MuGirl refitted	$[2.0, 2.5]$	$1.71^{+1.59}_{-1.00}$			
Staco Combined	$[2.0, 2.5]$	$0.24^{+0.36}_{-0.19}$		∞	$0.46^{+0.02}_{-0.15}$
	$[2.5, 3]$		$0.56^{+0.08}_{-0.08}$	$1.80^{+0.39}_{-0.38}$	$1.44^{+0.21}_{-0.21}$
MuGirl	$[2.0, 2.5]$	$1.56^{+1.12}_{-0.78}$			
MuTag +	$[2.0, 2.5]$				$0.47^{+0.02}_{-0.15}$
Staco Combined	$[2.5, 3]$	$0.54^{+0.05}_{-0.06}$			$1.40^{+0.20}_{-0.20}$

Table D.1: All scaling factors falling outside the plotting ranges in Figures 5.10 and 5.11 are given.

APPENDIX **E**

Simulated Monte Carlo Samples

The subsequently listed Monte Carlo samples are only accessible for ATLAS collaboration members and given for completeness.

E.1 MC Samples in Chapter 4

MC samples used in 4.2.4 and 4.3

rel. 15	min. bias	mc09_7TeV.105001.pythia_minbias.recon.ESD.e517_s764_s767_r1302
	$J/\psi \to \mu^+\mu^-$	mc09_7TeV.108496.Pythia_directJpsimu0mu0.recon.ESD.e540_s765_s767_r1302
	$Z \to \mu^+\mu^-$	mc09_7TeV.106047.PythiaZmumu_no_filter.recon.ESD.e468_s765_s767_r1302
	$t\bar{t}$	mc09_7TeV.105200.T1_McAtNlo_Jimmy.recon.ESD.e510_s765_s767_r1302
rel. 16	$J/\psi \to \mu^+\mu^-$	mc10_7TeV.108496.Pythia_directJpsimu0mu0.recon.ESD.e574_s933_s946_r2297
	$Z \to \mu^+\mu^-$	mc10_7TeV.106047.PythiaZmumu_no_filter.recon.ESD.e574_s933_s946_r2302
	$t\bar{t}$	mc10_7TeV.105200.T1_McAtNlo_Jimmy.recon.ESD.e598_s933_s946_r2302

E.2 MC Samples in Chapter 5

MC samples used in 5.6

$J/\psi \to \mu^+\mu^-$	mc10_7TeV.108496.Pythia_directJpsimu0mu0.recon.ESD.e574_s933_s946_r1662
$J/\psi \to \mu^+\mu^-$	mc10_7TeV.108407.Pythia_directJpsimu4mu4.recon.ESD.e574_s933_s946_r1662

E.3 MC Samples in Chapter 6

Each of the generated physics processes is listed individually with its corresponding ATLAS Monte Carlo sample name which includes the used Monte Carlo generator. In addition, the key numbers of the generation process are given, i.e. the cross section, filter efficiency ϵ_{filter}, k-factor as well as the number of generated events N_{MC}. Simulating events is a CPU intense process and it can hence be useful to optimize this process by applying a filter on truth level to reject not relevant events. The calculated cross section needs to be corrected for the possible event selection at truth level by ϵ_{filter}. Another correction factor to the cross section is the so called k-factor which is used to scale the calculated cross section of the generated process to a higher order calculation. In fact, this is only necessary for the samples generated with Alpgen.
For all processes in this section it is $l, l' \in e, \mu, \tau$. X stands as usual for all additional particles in the possible final states, while NpX denotes the generated additional number of X partons in the event. All simulated ATLAS Monte Carlo samples listed below are used in version `p605`.

simulated signal processes as introduced in 6.3.1

process	cross section [pb]	ϵ_{filter}	k	N_{MC}	sample name
$q\bar{q} \to W^+W^- \to e^+\mu^-\nu_e\bar{\nu}_\mu$	0.524	1.0	1.0	199960	`mc10_7TeV.105922.McAtNlo_JIMMY_WpWm_enumunu`
$q\bar{q} \to W^+W^- \to e^+\tau^-\nu_e\bar{\nu}_\tau$	0.524	1.0	1.0	198943	`mc10_7TeV.105923.McAtNlo_JIMMY_WpWm_enutaunu`
$q\bar{q} \to W^+W^- \to \mu^+\mu^-\nu_\mu\bar{\nu}_\mu$	0.524	1.0	1.0	199956	`mc10_7TeV.105924.McAtNlo_JIMMY_WpWm_munumunu`
$q\bar{q} \to W^+W^- \to \mu^+e^-\nu_\mu\bar{\nu}_e$	0.524	1.0	1.0	199961	`mc10_7TeV.105925.McAtNlo_JIMMY_WpWm_munuenu`
$q\bar{q} \to W^+W^- \to \mu^+\tau^-\nu_\mu\bar{\nu}_\tau$	0.524	1.0	1.0	198957	`mc10_7TeV.105926.McAtNlo_JIMMY_WpWm_munutaunu`
$q\bar{q} \to W^+W^- \to \tau^+\tau^-\nu_\tau\bar{\nu}_\tau$	0.524	1.0	1.0	198952	`mc10_7TeV.105927.McAtNlo_JIMMY_WpWm_taunutaunu`
$q\bar{q} \to W^+W^- \to \tau^+e^-\nu_\tau\bar{\nu}_e$	0.524	1.0	1.0	198962	`mc10_7TeV.105928.McAtNlo_JIMMY_WpWm_taunuenu`
$q\bar{q} \to W^+W^- \to \tau^+\mu^-\nu_\tau\bar{\nu}_\mu$	0.524	1.0	1.0	198954	`mc10_7TeV.105929.McAtNlo_JIMMY_WpWm_taunumunu`
$gg \to W^+W^- \to e^+\mu^-\nu_e\bar{\nu}_\mu$	0.0155	0.9899	1.0	9999	`mc10_7TeV.106012.gg2WW0240_JIMMY_WW_enumunu`
$gg \to W^+W^- \to e^+\tau^-\nu_e\bar{\nu}_\tau$	0.0155	0.9232	1.0	9997	`mc10_7TeV.106013.gg2WW0240_JIMMY_WW_enutaunu`
$gg \to W^+W^- \to \mu^+\mu^-\nu_\mu\bar{\nu}_\mu$	0.0155	0.9890	1.0	9998	`mc10_7TeV.106014.gg2WW0240_JIMMY_WW_munumunu`
$gg \to W^+W^- \to \mu^+e^-\nu_\mu\bar{\nu}_e$	0.0155	0.9869	1.0	9998	`mc10_7TeV.106015.gg2WW0240_JIMMY_WW_munuenu`
$gg \to W^+W^- \to \mu^+\tau^-\nu_\mu\bar{\nu}_\tau$	0.0155	0.9288	1.0	9997	`mc10_7TeV.106016.gg2WW0240_JIMMY_WW_munutaunu`
$gg \to W^+W^- \to \tau^+\tau^-\nu_\tau\bar{\nu}_\tau$	0.0155	0.3269	1.0	9998	`mc10_7TeV.106017.gg2WW0240_JIMMY_WW_taunutaunu`
$gg \to W^+W^- \to \tau^+e^-\nu_\tau\bar{\nu}_e$	0.0155	0.9219	1.0	9997	`mc10_7TeV.106018.gg2WW0240_JIMMY_WW_taunuenu`
$gg \to W^+W^- \to \tau^+\mu^-\nu_\tau\bar{\nu}_\mu$	0.0155	0.9289	1.0	9998	`mc10_7TeV.106019.gg2WW0240_JIMMY_WW_taunumunu`

simulated diboson background processes as introduced in 6.3.2

process	cross section [pb]	ϵ_{filter}	k	N_{MC}	sample name
$ZZ \to l^+l^-q\,\bar{q}$	0.533	1.0	1.0	24990	mc10_7TeV.105930.McAtNlo_JIMMY_ZZ_llqq
$ZZ \to l^+l^-l^+l^-$	0.026	1.0	1.0	99982	mc10_7TeV.105931.McAtNlo_JIMMY_ZZ_llll
$ZZ \to l^+l^-\nu\,\bar{\nu}$	0.152	1.0	1.0	99978	mc10_7TeV.105932.McAtNlo_JIMMY_ZZ_llnunu
$ZZ \to l^+l^-\tau^+\tau^-$	0.026	1.0	1.0	24995	mc10_7TeV.106036.McAtNlo_JIMMY_ZZ_2l2tau
$ZZ \to \tau^+\tau^-\tau^+\tau^-$	0.006	1.0	1.0	24991	mc10_7TeV.106037.McAtNlo_JIMMY_ZZ_4tau
$ZZ \to \nu\bar{\nu}\tau^+\tau^-$	0.077	1.0	1.0	24996	mc10_7TeV.113192.McAtNlo_JIMMY_ZZ_tautaununu
$ZZ \to q\bar{q}\tau^+\tau^-$	0.266	1.0	1.0	24990	mc10_7TeV.113193.McAtNlo_JIMMY_ZZ_tautauqq
$W^+Z \to l^+\nu\,q\,\bar{q}$	1.696	1.0	1.0	24989	mc10_7TeV.105940.McAtNlo_JIMMY_WpZ_lnuqq
$W^+Z \to l^+\nu\,l^+l^-$	0.161	1.0	1.0	24995	mc10_7TeV.105941.McAtNlo_JIMMY_WpZ_lnull
$W^+Z \to q'\bar{q}\,l^+l^-$	0.506	1.0	1.0	24992	mc10_7TeV.105942.McAtNlo_JIMMY_WpZ_qqll
$W^-Z \to l^-\bar{\nu}\,q\,\bar{q}$	0.920	1.0	1.0	24993	mc10_7TeV.105970.McAtNlo_JIMMY_WmZ_lnuqq
$W^-Z \to l^-\bar{\nu}\,l^+l^-$	0.088	1.0	1.0	99972	mc10_7TeV.105971.McAtNlo_JIMMY_WmZ_lnull
$W^-Z \to q'\bar{q}\,l^+l^-$	0.274	1.0	1.0	99968	mc10_7TeV.105972.McAtNlo_JIMMY_WmZ_qqll
$W^+Z \to \tau^+\nu_\tau\,l^+\,l^-$	0.081	1.0	1.0	24994	mc10_7TeV.106024.McAtNlo_JIMMY_WpZ_taunull
$W^+Z \to l^+\nu\,\tau^+\tau^-$	0.082	1.0	1.0	24992	mc10_7TeV.106025.McAtNlo_JIMMY_WpZ_lnutautau
$W^+Z \to \tau^+\nu_\tau\tau^+\tau^-$	0.041	1.0	1.0	24990	mc10_7TeV.106026.McAtNlo_JIMMY_WpZ_taunutautau
$W^-Z \to \tau^-\bar{\nu}_\tau\,l^+\,l^-$	0.044	1.0	1.0	24997	mc10_7TeV.106027.McAtNlo_JIMMY_WmZ_taunull
$W^-Z \to l^-\bar{\nu}\,\tau^+\tau^-$	0.044	1.0	1.0	24993	mc10_7TeV.106028.McAtNlo_JIMMY_WmZ_lnutautau
$W^-Z \to \tau^-\bar{\nu}_\tau\tau^+\tau^-$	0.022	1.0	1.0	24941	mc10_7TeV.106029.McAtNlo_JIMMY_WmZ_taunutautau
$W^+Z \to q\,\bar{q}\,\tau^+\tau^-$	0.249	1.0	1.0	24987	mc10_7TeV.113190.McAtNlo_JIMMY_WpZ_qqtautau
$W^-Z \to q\,\bar{q}\,\tau^+\tau^-$	0.137	1.0	1.0	24989	mc10_7TeV.113191.McAtNlo_JIMMY_WpZ_qqtautau
$W^+\gamma \to \mu^+\nu_\mu + \gamma$	28.000	1.0	1.0	49995	mc10_7TeV.106002.Pythia_MadGraph_Wplusmunugamma
$W^+\gamma \to \tau^+\nu_\tau + \gamma$	25.400	0.167	1.0	49996	mc10_7TeV.106003.Pythia_MadGraph_Wplustaunugamma
$W^-\gamma \to \mu^-\bar{\nu}_\mu + \gamma$	18.590	1.0	1.0	49996	mc10_7TeV.108289.Pythia_MadGraph_Wminusmunugamma
$W^-\gamma \to \tau^-\bar{\nu}_\tau + \gamma$	17.340	0.169	1.0	49996	mc10_7TeV.108290.Pythia_MadGraph_Wminustaunugamma

simulated W+jets background processes as introduced in 6.3.2

process	cross section [pb]	ϵ_{filter}	k	N_{MC}	sample name
$W^\pm + \text{Np0} \rightarrow \mu^\pm \overset{(-)}{\nu}_\mu + \text{Np0}$	6919.60	1.0	1.2	3466523	mc10_7TeV.107690.AlpgenJimmyWmunuNp0_pt20
$W^\pm + \text{Np1} \rightarrow \mu^\pm \overset{(-)}{\nu}_\mu + \text{Np1}$	1304.20	1.0	1.2	2499513	mc10_7TeV.107691.AlpgenJimmyWmunuNp1_pt20
$W^\pm + \text{Np2} \rightarrow \mu^\pm \overset{(-)}{\nu}_\mu + \text{Np2}$	377.83	1.0	1.2	3768893	mc10_7TeV.107692.AlpgenJimmyWmunuNp2_pt20
$W^\pm + \text{Np3} \rightarrow \mu^\pm \overset{(-)}{\nu}_\mu + \text{Np3}$	101.88	1.0	1.2	1009589	mc10_7TeV.107693.AlpgenJimmyWmunuNp3_pt20
$W^\pm + \text{Np4} \rightarrow \mu^\pm \overset{(-)}{\nu}_\mu + \text{Np4}$	25.75	1.0	1.2	254879	mc10_7TeV.107694.AlpgenJimmyWmunuNp4_pt20
$W^\pm + \text{Np5} \rightarrow \mu^\pm \overset{(-)}{\nu}_\mu + \text{Np5}$	6.92	1.0	1.2	69958	mc10_7TeV.107695.AlpgenJimmyWmunuNp5_pt20
$W^\pm + \text{Np0} \rightarrow \tau^\pm \overset{(-)}{\nu}_\tau + \text{Np0}$	6918.60	1.0	1.2	3259564	mc10_7TeV.107700.AlpgenJimmyWtaunuNp0_pt20
$W^\pm + \text{Np1} \rightarrow \tau^\pm \overset{(-)}{\nu}_\tau + \text{Np1}$	1303.20	1.0	1.2	2496467	mc10_7TeV.107701.AlpgenJimmyWtaunuNp1_pt20
$W^\pm + \text{Np2} \rightarrow \tau^\pm \overset{(-)}{\nu}_\tau + \text{Np2}$	378.18	1.0	1.2	3764804	mc10_7TeV.107702.AlpgenJimmyWtaunuNp2_pt20
$W^\pm + \text{Np3} \rightarrow \tau^\pm \overset{(-)}{\nu}_\tau + \text{Np3}$	101.51	1.0	1.2	1008514	mc10_7TeV.107703.AlpgenJimmyWtaunuNp3_pt20
$W^\pm + \text{Np4} \rightarrow \tau^\pm \overset{(-)}{\nu}_\tau + \text{Np4}$	25.64	1.0	1.2	248864	mc10_7TeV.107704.AlpgenJimmyWtaunuNp4_pt20
$W^\pm + \text{Np5} \rightarrow \tau^\pm \overset{(-)}{\nu}_\tau + \text{Np5}$	7.04	1.0	1.2	64950	mc10_7TeV.107705.AlpgenJimmyWtaunuNp5_pt20

simulated single top and $t\bar{t}$ background processes as introduced in 6.3.2

process	cross section [pb]	ϵ_{filter}	k	N_{MC}	sample name
$t\bar{t} \rightarrow l^\pm \overset{(-)}{\nu}_l + X$	164.57	0.55551	1.0	14845714	mc10_7TeV.105200.T1_McAtNlo_Jimmy
$W^\pm \overset{(-)}{t} \rightarrow X$	15.60	1.0	1.0	299805	mc10_7TeV.105500.AcerMC_Wt
$t \rightarrow \mu^\pm \overset{(-)}{\nu}_\mu + X$ s-channel	0.50	1.0	1.0	299877	mc10_7TeV.108344.st_schan_munu_McAtNlo_Jimmy
$t \rightarrow \tau^\pm \overset{(-)}{\nu}_\tau + X$ s-channel	0.50	1.0	1.0	299864	mc10_7TeV.108345.st_schan_taunu_McAtNlo_Jimmy
$t \rightarrow \mu^\pm \overset{(-)}{\nu}_\mu + X$ t-channel	6.93	1.0	1.0	199910	mc10_7TeV.117361.st_tchan_munu_AcerMC
$t \rightarrow \tau^\pm \overset{(-)}{\nu}_\tau + X$ t-channel	6.93	1.0	1.0	199907	mc10_7TeV.117362.st_tchan_taunu_AcerMC

simulated Z+jets background processes as introduced in 6.3.2

process	cross section [pb]	$\epsilon_{\mathrm{filter}}$	k	N_{MC}	sample name
$Z + \mathrm{Np0} \to \mu^+\mu^- + \mathrm{Np0}$	668.68	1.0	1.25	6619010	mc10_7TeV.107660.AlpgenJimmyZmumuNp0_pt20
$Z + \mathrm{Np1} \to \mu^+\mu^- + \mathrm{Np1}$	134.14	1.0	1.25	1334723	mc10_7TeV.107661.AlpgenJimmyZmumuNp1_pt20
$Z + \mathrm{Np2} \to \mu^+\mu^- + \mathrm{Np2}$	40.33	1.0	1.25	403886	mc10_7TeV.107662.AlpgenJimmyZmumuNp2_pt20
$Z + \mathrm{Np3} \to \mu^+\mu^- + \mathrm{Np3}$	11.19	1.0	1.25	109954	mc10_7TeV.107663.AlpgenJimmyZmumuNp3_pt20
$Z + \mathrm{Np4} \to \mu^+\mu^- + \mathrm{Np4}$	2.75	1.0	1.25	29978	mc10_7TeV.107664.AlpgenJimmyZmumuNp4_pt20
$Z + \mathrm{Np5} \to \mu^+\mu^- + \mathrm{Np5}$	0.77	1.0	1.25	9993	mc10_7TeV.107665.AlpgenJimmyZmumuNp5_pt20
$Z + \mathrm{Np0} \to \mu^+\mu^- + \mathrm{Np0}$ (l.m.)	3051.62	0.0376	1.22	494918	mc10_7TeV.116948.AlpgenJimmyZmumuNp0_Ml110to40Pt15Pt5
$Z + \mathrm{Np1} \to \mu^+\mu^- + \mathrm{Np1}$ (l.m.)	87.87	0.488	1.22	299939	mc10_7TeV.116949.AlpgenJimmyZmumuNp1_Ml110to40Pt15Pt5
$Z + \mathrm{Np2} \to \mu^+\mu^- + \mathrm{Np2}$ (l.m.)	41.45	1.0	1.22	499864	mc10_7TeV.116262.AlpgenJimmyZmumuNp2_Ml110to40_pt20
$Z + \mathrm{Np3} \to \mu^+\mu^- + \mathrm{Np3}$ (l.m.)	8.38	1.0	1.22	149939	mc10_7TeV.116263.AlpgenJimmyZmumuNp3_Ml110to40_pt20
$Z + \mathrm{Np4} \to \mu^+\mu^- + \mathrm{Np4}$ (l.m.)	1.85	1.0	1.22	39988	mc10_7TeV.116264.AlpgenJimmyZmumuNp4_Ml110to40_pt20
$Z + \mathrm{Np5} \to \mu^+\mu^- + \mathrm{Np5}$ (l.m.)	0.46	1.0	1.22	9996	mc10_7TeV.116265.AlpgenJimmyZmumuNp5_Ml110to40_pt20
$Z + \mathrm{Np0} \to \tau^+\tau^- + \mathrm{Np0}$	668.40	1.0	1.25	6608784	mc10_7TeV.107670.AlpgenJimmyZtautauNp0_pt20
$Z + \mathrm{Np1} \to \tau^+\tau^- + \mathrm{Np1}$	134.81	1.0	1.25	1322674	mc10_7TeV.107671.AlpgenJimmyZtautauNp1_pt20
$Z + \mathrm{Np2} \to \tau^+\tau^- + \mathrm{Np2}$	40.36	1.0	1.25	403864	mc10_7TeV.107672.AlpgenJimmyZtautauNp2_pt20
$Z + \mathrm{Np3} \to \tau^+\tau^- + \mathrm{Np3}$	11.25	1.0	1.25	109947	mc10_7TeV.107673.AlpgenJimmyZtautauNp3_pt20
$Z + \mathrm{Np4} \to \tau^+\tau^- + \mathrm{Np4}$	2.79	1.0	1.25	29977	mc10_7TeV.107674.AlpgenJimmyZtautauNp4_pt20
$Z + \mathrm{Np5} \to \tau^+\tau^- + \mathrm{Np5}$	0.77	1.0	1.25	9990	mc10_7TeV.107675.AlpgenJimmyZtautauNp5_pt20
$Z + \mathrm{Np0} \to \tau^+\tau^- + \mathrm{Np0}$ (l.m.)	378.50	0.000484	1.22	42997	mc10_7TeV.116940.AlpgenJimmyZtautaullNp0_Ml110to40Pt15Pt5
$Z + \mathrm{Np1} \to \tau^+\tau^- + \mathrm{Np1}$ (l.m.)	10.72	0.0277	1.22	79985	mc10_7TeV.116941.AlpgenJimmyZtautaullNp1_Ml110to40Pt15Pt5
$Z + \mathrm{Np2} \to \tau^+\tau^- + \mathrm{Np2}$ (l.m.)	5.146	0.0264	1.22	34488	mc10_7TeV.116942.AlpgenJimmyZtautaullNp2_Ml110to40Pt15Pt5
$Z + \mathrm{Np3} \to \tau^+\tau^- + \mathrm{Np3}$ (l.m.)	1.037	0.0487	1.22	14996	mc10_7TeV.116943.AlpgenJimmyZtautaullNp3_Ml110to40Pt15Pt5
$Z + \mathrm{Np4} \to \tau^+\tau^- + \mathrm{Np4}$ (l.m.)	0.228	0.0691	1.22	4996	mc10_7TeV.116944.AlpgenJimmyZtautaullNp4_Ml110to40Pt15Pt5
$Z + \mathrm{Np5} \to \tau^+\tau^- + \mathrm{Np5}$ (l.m.)	0.05799	0.0957	1.22	1996	mc10_7TeV.116945.AlpgenJimmyZtautaullNp5_Ml110to40Pt15Pt5

simulated Higgs events as introduced in 6.9

process	cross section [pb]	ϵ_{filter}	k	N_{MC}	sample name
$H \to W^+W^- \to l^+ l'^- \nu_l \bar{\nu}_{l'}$	452.09	0.001	1.0	499891	mc10_7TeV.116613.PowHegPythia_ggH130_WW2lep
$qqH \to W^+W^- + X \to l^+ l'^- \nu_l \bar{\nu}_{l'} + X$	36.948	0.001	1.0	49983	mc10_7TeV.116623.PowHegPythia_VBFH130_WW2lep
$W^\pm H \to W^\pm W^+W^- \to l^+ l'^- \nu_l \bar{\nu}_{l'} + X$	16.034	0.001	1.0	19993	mc10_7TeV.125235.PythiaWH130_WW2lep
$ZH \to ZW^+W^- \to l^+ l'^- \nu_l \bar{\nu}_{l'} + X$	8.895	0.001	1.0	19992	mc10_7TeV.125395.PythiaZH130_WW2lep

APPENDIX **F**

List of Acronyms

The subsequent list shows all acronyms and their meaning used throughout this thesis in alphabetical order. The page of their first mentioning/explanation is given for reference.

ADC	Analog to Digital Converter	p. 57
ALICE	A Large Ion Collider Experiment	p. 17
aTGC	anomalous Triple Gauge Boson Coupling	p. 8
ATLAS	A Toroidal LHC Apparatus	p. 19
BNL	Brookhaven National Lab	p. 5
BR	Branching ratio	p. 6
CERN	European Organization for Nuclear Research	p. 15
CDF	The Collider Detector at Fermilab	p. 10
CMS	Compact Muon Solenoid	p. 17
CPU	Central Processing Unit (integral part of computers)	
CSC	Cathode Strip Chamber	p. 32
EF	Event Filter Trigger (Level 3 Trigger)	p. 38
EM	Electromagnetic (used in various contexts)	
FSR	Final State Radiation	p. 40
FCal	Forward Calorimeter	p. 28
HEC	Hadronic Endcap Calorimeter	p. 28
HLT	High Level Trigger (L2 and EF)	p. 38
HS	Hard Scattering	p. 40
ID	Inner Detector	p. 22
IP	Interaction Point	p. 22
ISR	Initial State Radiation	p. 40
L1	Level 1 Trigger	p. 38
L2	Level 2 Trigger	p. 38
LAr	Liquid Argon	p. 27
LEP	Large Electron Positron Collider	p. 16

LHC	Large Hadron Collider	p. 16
LHCb	Large Hadron Collider beauty	p. 17
MC	Monte Carlo	p. 40
MDT	Monitor Drift Tube	p. 29
MET	Missing Transverse Energy	p. 42
MIP	Minimum Ionizing Particle	p. 28
MIT	Massachusetts Institute of Technology	p. 5
MOORE	Muon Object Oriented Reconstruction	p. 45
MS	Muon Spectrometer	p. 28
MUID	Muon Identification	p. 44
NLO	Next-to-Leading Order	p. 9
PDF	Parton Distribution Function	p. 40
PS	Proton Synchroton	p. 16
RPC	Resistive Plate Chamber	p. 32
RoI	Region of Interest	p. 38
SCT	Semiconductor Tracker	p. 24
sf	scaling factor	p. 85
SLAC	Stanford Linear Accelerator Center	p. 5
SM	Standard Model of Particle Physics	p. 2
SPS	Super Proton Synchroton	p. 16
STACO	Statistical Combination	p. 44
TGC	Thin Gap Chamber	p. 33
TRT	Transition Radiation Tracker	p. 25
UE	Underlying Event	p. 40
VBF	Vector Boson Fusion	p. 4

References

[1] K. Nakamura et al. (Particle Data Group), JP G 37, 075021 (2010) and 2011 partial update for the 2012 edition (URL: `http://pdg.lbl.gov`)

[2] K. Simonyi, *Die Kultur-Geschichte der Physik*, Harri Deutsch Verlag, ISBN: 3-8171-1651-9

[3] E. Noether, *Invariante Variationsprobleme*, Nachr. D. König. Gesellsch. D. Wiss. Zu Göttingen, Math-phys. Klasse (235-257), 1918

[4] F. Halzen and A.D. Martin, *Quarks & Leptons*, John Wiley & Sons Inc., ISBN: 0-471-88741-2, 1984

[5] B. Povh, K. Rith, C. Scholz and F. Zetsche, *Particles and Nuclei*, Springer Verlag, ISBN: 3-540-20168-8, 2004

[6] J. P. Ottersbach, *Micro Black Holes at the LHC*, Lambert Academic Publishing, ISBN: 978-3-8383-7273-0, 2010

[7] J.-P. Lansberg, *J/ψ, ϕ' and Υ Production at Hadron Colliders: A Review*, arXiv:hep-ph/0602091v2, 2006

[8] ATLAS Collaboration, *Measurement of the differential cross-section of inclusive, prompt and non-prompt J/ψ production in proton-proton collisions at $\sqrt{s} = 7$ TeV*, Nuclear Physics B 850 (387-444), arXiv:1104.3038v2 [hep-ex], 2011

[9] P. W. Higgs, *Broken Symmetry and the Mass of Gauge Vector Mesons*, Phys. Rev. Lett. 13 (321-323), 1964

[10] LEP Working Group for Higgs boson searches, *Search for the Standard Model Higgs Boson at LEP*, arXiv:hep-ex/0306033, 2003

[11] The ATLAS and CMS Collaborations, *Combined Standard Model Higgs boson searches with up to 2.3 fb^{-1} of pp collision data at $\sqrt{s} = 7$ TeV at the LHC*, ATLAS-CONF-2011-157, 2011

[12] P. Spangolo, *Boson Gauge Couplings at LEP*, arXiv:hep-ex/0506048, 2005

[13] P. Azzurri, *WW Production, Polarisation and Spin Correlations at LEP*, arXiv:hep-ex/0610060v1, 2006

[14] E. Lipeles, *WW and WZ production at the Tevatron*, arXiv:hep-ex/0701038, 2007

[15] R. W. Brown and K. O. Mikaelian, *W^+W^- and Z^0Z^0 pair production in e^+e^-, pp, and $p\bar{p}$ colliding beams*, Phys. Rev. D19 922, 1979

[16] S. Frixione, *A next-to-leading order calculation of the cross section for the production of W^+W^- pairs in hadronic collisions*, Nucl. Phys. B410 280-324, 1993

[17] J. Ohnemus, *Hadronic ZZ, W^+W^-, and $W^\pm Z$ Production with QCD Corrections and Leptonic Decays*, Phys. Rev. D50 1931-1945, 1994

[18] J. M. Campbell, R. K. Ellis and C. Williams, *Vector boson pair production at the LHC*, arXiv:1105.0020, 2011

[19] ATLAS Collaboration, *Measurement of the inclusive $W^\pm$ and Z/γ^* cross sections in the e and μ decay channels in pp collisions at $\sqrt{s} = 7$ TeV with the ATLAS detector*, arXiv:1109.5141v3 [hep-ex], 2011

[20] ATLAS Collaboration, *Measurement of the cross section for top-quark pair production in pp collisions at $\sqrt{s} = 7$ TeV with the ATLAS detector using final states with two high-pt leptons*, arXiv:1202.4892v1 [hep-ex], 2012

[21] L. Evans and P. Bryant, *LHC Machine*, JINST 3 S08001, 2008

[22] ATLAS Collaboration, *The ATLAS Experiment at the CERN Large Hadron Collider*, JINST 3 S08003, 2008

[23] ALICE Collaboration, *The ALICE experiment at the CERN LHC*, JINST 3 S08002, 2008

[24] CMS Collaboration, *The CMS Experiment at the CERN LHC*, JINST 3 S08004, 2008

[25] LHCb Collaboration, *The LHCb Detector at the LHC*, JINST 3 S08005, 2008

[26] TeVI Group, *Design Report Tevatron 1 project*, FERMILAB-DESIGN-1984-01, 1984

[27] ATLAS, *ATLAS muon spectrometer: Technical Design Report*, 1997

[28] ATLAS Computing Group, *ATLAS Computing : Technical Design Report*, ATLAS-TDR-017;CERN-LHCC-2005-022, 2005

[29] M. Cacciari, G. P. Salam and G. Soyez, *The anti-kt jet clustering algorithm*, arXiv:0802.1189v2, 2008

[30] G. Corcella, I. G. Knowles, G. Marchesini, S. Moretti, K. Odagiri, P. Richardson, M. H. Seymour and B. R. Webber, *HERWIG 6.5: an event generator for Hadron Emission Reactions With Interfering Gluons (including supersymmetric processes)**, arXiv:0011363v3;CERN-TH-2000-284, 2002

[31] M. Bähr, S. Gieseke, M. A. Gigg, D. Grellscheid, K. Hamilton, O. Latunde-Dada, S. Plätzer, P. Richardson, M. H. Seymour, A. Sherstnev, J. Tully and B. R. Webber, *Herwig++ Physics and Manual*, arXiv:0803.0883v3;CERN-PH-TH-2008-038, 2008

[32] T. Sjöstrand, S. Mrenna and P. Skands, *A Brief Introduction to PYTHIA 8.1*, arXiv:0710.3820;CERN-LCGAPP-2007-04, 2007

[33] T. Gleisberg, S. Höche, F. Krauss, M. Schönherr, S. Schumann, F. Siegert and J. Winter, *Event generation with SHERPA 1.1*, arXiv:0811.4622;FERMILAB-PUB-08-477-T1, 2008

[34] A. dell' Acqua, A. di Simone, M. V. Gallas, A. Rimoldi, V. Tsulaia, I. Ueda, S. Vahsen and Z. Marshall, *ATLAS Simulation readiness for first data at LHC*, ATLAS-SOFT-CONF-2007-001, 2007

[35] Geant4 Collaboration, *Introduction to Geant4*, `http://geant4.web.cern.ch/geant4/support/userdocuments.shtml`, 2010

[36] D. Adams et al, *Track Reconstruction in the ATLAS Muon Spectrometer with MOORE*, ATLAS-SOFT-2003-007, 2003

[37] M. Virchaux, *Muonbox: a full 3D tracking programme for Muon reconstruction in the ATLAS Spectrometer*, ATL-MUON-97-198, 1997

[38] R. Nicolaidou, L. Chevalier, S. Hassani, J. F. Laporte, E. le Menedeu and A. Ouraou, *Muon identification procedure for the ATLAS detector at the LHC using Muonboy reconstruction package and tests of its performance using cosmic rays and single beam data*, J. Phys.: Conf. Ser. 219 032052, 2010

[39] S. Hassani at al., *A muon identification and combined reconstruction procedure for the ATLAS detector at the LHC using the (MUONBOY, STACO, MuTag) reconstruction packages*, Nucl. Instrum. Meth. A572 (77-79), 2007

[40] E. Lund, L. Bugge, T. G. Cornelissen, M. Elsing, I. Gavrilenko, W. Liebig, D. López Mateos, A. Salzburger, A. Strandlie and S. Todorova, *Refitting of combined inner detector and muon spectrometer tracks from Monte Carlo samples by using the Kalman fitter and the STEP algorithm in the ATLAS experiment*, ATL-SOFT-PUB-2008-005, 2008

[41] ATLAS Collaboration, *MDT calibration plots*, ATLAS-PLOT-MUON-2011-002, 2011

[42] T. Cornelissen, M. Elsing, I. Gavrilenko, S. Fleischmann, W. Liebig, E. Moyse and A. Salzburger, *Concepts, Design and Implementation of the ATLAS New Tracking (NEWT)*, ATL-SOFT-PUB-2007-007, 2007

[43] ATLAS Collaboration, *Charged-particle multiplicities in pp interactions measured with the ATLAS detector at the LHC*, CERN-PH-EP-2010-079, 2011

[44] ATLAS Collaboration, *A measurement of the ATLAS muon reconstruction and trigger efficiency using J/ψ decays*, ATLAS-CONF-2011-021, 2011

[45] ATLAS Collaboration, *Di-muon composition in ATLAS at* 7 TeV, ATLAS-CONF-2011-003, 2011

[46] ATLAS Collaboration, *Determination of the muon reconstruction efficiency in ATLAS at the Z resonance in proton-proton collisions at* $\sqrt{s} = 7$ TeV, ATLAS-CONF-2011-008, 2011

[47] ATLAS Collaboration, *Measurement of the WW production cross section in* $\sqrt{s} =$ 7 TeV *pp collisions and limits on anomalous gauge couplings*, arXiv:1203.6232v1 [hep-ex], 2012

[48] CMS Collaboration, *Measurement of W^+W^- production and search for the Higgs boson in pp collisions at* $\sqrt{s} = 7$ TeV, Physics Letters B 699 (2011) 25-47, 2011

[49] ATLAS Collaboration, *The Virtual Point 1 Event Display for the ATLAS Experiment*, in Proceedings of Computing in High Energy and Nuclear Physics 2009 Conference (CHEP2009), Prague, Czech Republic, 2009

[50] ATLAS Collaboration, *Updated Luminosity Determination in pp Collisions at* $\sqrt{s} =$ 7 TeV *using the ATLAS Detector*, ATLAS-CONF-2011-011, 2011

[51] P. M. Nadolsky, H.-L. Lai, Q.-H. Cao, J. Huston, J. Pumplin, D. Stump, W.-K. Tung, C.-P. Yuan, *Implications of CTEQ global analysis for collider observables*, Phys.Rev.D78:013004, arXiv:0802.0007v3 [hep-ph], 2008

[52] A.D. Martin, W.J. Stirling, R.S. Thorne, G. Watt, *Parton distributions for the LHC*, arXiv:0901.0002v3 [hep-ph], 2009

[53] *Rocky Balboa*, Dir. Sylvester Stallone, Perf. Sylvester Stallone, Antonio Tarver and Milo Ventimiglia, Metro-Goldwyn-Mayer / Columbia Pictures / Revolution Studios, 2006

ATLAS Collaboration Internal Publications

[54] L. Asquith et al., *Performance of Jet Algorithms in the ATLAS Detector*, ATL-COM-PHYS-2009-630, 2009

[55] D. Fassouliotis, T. Lagouri, A. Poppleton, S. Robins, G. Stavropoulos and I. Vichou, *Muon Identification using the MUID package*, ATL-COM-MUON-2003-003, 2003

[56] J. Alison et al., *Measurement of the WW Production Cross Section in Proton-Proton Collisions at* $\sqrt{s} = 7$ TeV *with the ATLAS Detector and Limits on the Anomalous Triple-Gauge-Boson Couplings*, ATL-COM-PHYS-2011-1522, 2012

[57] M. Antonelli et all, *Performance of Missing Transverse Energy Reconstruction in Proton-Proton Collisions at* 7 TeV *with ATLAS*, ATL-COM-PHYS-2011-567, 2011

PhD theses

[58] M. Limper, *Track and vertex reconstruction in the ATLAS inner detector*, ISBN: 978-90-9024572-0, 2009

[59] N. van Eldik, *The ATLAS muon spectrometer: calibration and pattern recognition*, ISBN: 978-90-6464-071-1, 2007

[60] J. Snuverink, *The ATLAS muon spectrometer: commissioning and tracking*, ISBN: 978-90-365-2912-9, 2009

[61] G. Ordóñez Sanz, *Muon Identification in the ATLAS Calorimeters*, 2009

[62] Z. van Kesteren, *Identification of muons in ATLAS*, ISBN: 978-90-9025098-4, 2010

[63] M. Kayl, *Measurement of the charged particle density with the ATLAS detector*, ISBN: 978-94-91211-14-0, 2011

[64] A. Koutsman, *On the Road to Supersymmetry with ATLAS*, ISBN: 978-90-6464-476-4, 2011

web links

[65] *Convention for the Establishment of a European Organization for Nuclear Research*, `http://council.web.cern.ch/council/en/Governance/Convention.html`, 1953

[66] publications from the LHC Higgs Cross Section Working Group, `https://twiki.cern.ch/twiki/bin/view/LHCPhysics/CrossSections`

[67] documentation on Top quark Monte Carlo samples, `https://twiki.cern.ch/twiki/bin/viewauth/AtlasProtected/TopMC10For2011Data`

[68] ATLAS B-physics publications, `https://twiki.cern.ch/twiki/bin/view/AtlasPublic/BPhysPublicResults`

[69] publications on the ATLAS Detector status, `https://twiki.cern.ch/twiki/bin/view/AtlasPublic/ApprovedPlotsATLASDetector`

[70] publications on the ATLAS Pixel detector, `https://twiki.cern.ch/twiki/bin/view/AtlasPublic/PixelPublicResults`

[71] publications on the ATLAS SCT detector, https://twiki.cern.ch/twiki/bin/view/AtlasPublic/SCTPublicResults

[72] publications on the ATLAS LAr calorimeter, https://twiki.cern.ch/twiki/bin/view/AtlasPublic/LArCaloPublicResults2010

[73] publications on the ATLAS Tile calorimeter, https://twiki.cern.ch/twiki/bin/view/AtlasPublic/TileCaloPublicResults

[74] publications on the ATLAS trigger system, https://twiki.cern.ch/twiki/bin/view/AtlasPublic/TriggerPublicResults

[75] ATLAS event displays, https://twiki.cern.ch/twiki/bin/view/AtlasPublic/EventDisplayPublicResults

[76] publications from the Muon Combined Performance Working Group, https://twiki.cern.ch/twiki/bin/view/AtlasPublic/MuonPerformancePublicPlots

[77] analysis guidelines of the ATLAS MCP group, https://twiki.cern.ch/twiki/bin/view/AtlasProtected/MCPAnalysisGuidelinesRel16

[78] documentation on MuTag, https://twiki.cern.ch/twiki/bin/view/AtlasProtected/MuTagDocumentation

[79] documentation on MuGirl, https://twiki.cern.ch/twiki/bin/viewauth/Atlas/MuGirl

[80] documentation on the calorimeter muon taggers, https://twiki.cern.ch/twiki/bin/viewauth/Atlas/CaloMuonContainer

[81] documentation on jet cleaning, https://twiki.cern.ch/twiki/bin/viewauth/AtlasProtected/HowToCleanJets2011

[82] analysis guidelines of the ATLAS JetEtmiss group, https://twiki.cern.ch/twiki/bin/viewauth/AtlasProtected/JetEtmissDataAnalysisRecommendationSummer2010

private communications

[83] private communication with Dr. Gerjan Bobbink

[84] private communication with Dr. Olya Igonkina

[85] private communication with Prof. Dr. Stan Bentvelsen

"Der grösste Sinnesgenuß [...] ist, im gesunden Zustande, Ruhe nach der Arbeit."

Immanuel Kant

Acknowledgements

The past four and a half years were thrilling and challenging at the same time. I consider myself fortunate to have been able to work in a fantastic group at Nikhef for the ATLAS experiment at CERN in such exciting times, with the first data coming in right in the middle of my PhD.
I would like to thank my promoter Prof. Dr. Stan Bentvelsen as well as my supervisor Dr. Peter Kluit for all their support and guidance, particularly in the final year of my PhD. I would also like to thank Dr. Max Baak who supervised me during my first half year at Nikhef, getting me involved in an interesting Higgs analysis right from the start.
I thank my family and all my friends for their support particularly during the difficult periods in my PhD. Hereby I include all my fantastic colleagues from Nikhef and CERN that I long consider my friends. We had four and a half amazing years in Amsterdam as well as in the region of Geneva with lots of fun also beyond the office hours. A special thanks goes to my paranimfs Ido Mussche and Marten Bosma, as well as my "paranimf of honor" Lucie de Nooij.